Lifetime Estimation for Ductile Failure in Semicrystalline Polymer Pipes

Mehrzad Taherzadehboroujeni

Dissertation submitted to the faculty of the Virginia Polytechnic Institute and State University in partial fulfillment for of the requirements for the degree of

Doctor of Philosophy

In

Engineering Mechanics

Scott W. Case

Mark S. Cramer

Saied Taheri

Michael J. Bortner

June 24, 2019

Blacksburg, VA

Keywords: High density Polyethylene, Creep rupture, Lifetime, Simulation, Failure

Lifetime Estimation for Ductile Failure in Semicrystalline Polymer Pipes

Mehrzad Taherzadehboroujeni

Abstract

The aim of this study is to develop a combined experimental and analytical framework for accelerated lifetime estimates of semi-crystalline plastic pipes which is sensitive to changes in structure, orientation, and morphology introduced by processing conditions. To accomplish this task, high-density polyethylene (HDPE) is chosen as the exemplary base material. As a new accelerated test protocol, several characterization tests were planned and conducted on as-manufactured HDPE pipe segments. Custom fixtures are designed and developed to admit uniaxial characterization tests. The yield behavior of the material was modeled using two hydrostatic pressure modified Eyring equations in parallel to describe the characterization test data collected in axial tension and compression. Subsequently, creep rupture failure of the pipes under hydrostatic pressure is predicted using the model. The model predictions are validated using the experimental creep rupture failure data collected from internal pressurization of pipes using a custom-designed, fully automatic test system. The results indicate that the method allows the prediction of pipe service lifetimes in excess of 50 years using experiments conducted over approximately 10 days instead of the traditional 13 months. The analytical model is joined with a commercial finite element package to allow simulations including different thermal-mechanical loading conditions as well as complicated geometries. The numerical model is validated using the characterization test data at different temperatures and deformation rates. The results suggest that the long-term performance of the pipe is dominated by the plastic behavior of the material and its viscoelastic response is found to play an insignificant role in this manner. Because of the potential role of residual stresses on the long-term behavior, the residual stress across the wall thickness is measured for three geometrically different HDPE pipes. As expected, the magnitude of tensile and compressive residual stresses are found to be greater in pipes with thicker walls. The effect of the residual stress on the long-term performance of the pipes is investigated by including the residual

stress measurements into the numerical simulations. The residual stress slightly accelerates the failure process; however, for the pipe geometries examined, this acceleration is insignificant.

Lifetime Estimation for Ductile Failure in Semicrystalline Polymer Pipes

Mehrzad Taherzadehboroujeni

General Audience Abstract

The use of plastic pipes to carry liquids and gases has greatly increased in recent decades, primarily because of their moderate costs, long service lifetimes, and corrosion resistance compared with materials such as corrugated steel and ductile iron. Before these pipes can be effectively used, however, designers need the capability to quickly predict the service lifetime so that they can choose the best plastic material and pipe design for a specific application. This capability also allows manufacturers to modify materials to improve performance.

The aim of this study is to develop a combination of experiments and models to quickly predict the service lifetime of plastic pipes. High-density polyethylene (HDPE) was chosen as the plastic material on which the model was developed. Several characterization tests are planned and conducted on as-manufactured HDPE pipe segments. The yielding behavior of the material is modeled and the lifetime predictions are evaluated. The predictions are validated by experimental data captured during pipe burst tests conducted in the lab. The results indicate that the method allows the accurate prediction of pipe service lifetimes in excess of 50 years using experiments conducted over approximately 10 days instead of the traditional 13 months, resulting in significant savings in time (and consequently costs) and making it possible to introduce new materials into production more rapidly.

Dedication

For my parents, Shahin and Mohammadreza, for your endless love and support during my entire life.

Acknowledgments

The following list is for all of the people who helped me over the past few years by their advice, conversation, or technical support.

Dr. Scott W. Case, your advice, support, and guidance helped me grow as a person and as a professional engineer during the past four years. I sincerely appreciate you for taking your precious time discussing my research and advising me on several challenges I have been through.

Dr. Mark S. Cramer, I want to thank you for your deep knowledge of Engineering Mechanics and your support over the years inspired me during my research.

Dr. Michael J. Bortner, your knowledge of polymer morphology and structure-property relationships inspired and sparked my interest in learning more about the microstructure of the semicrystalline polymers.

Dr. Saied Taheri, thank you for your advice and support over the past few years.

Dr. Robert Moore, your communications and collaboration helped ensure my publication in Polymer Engineering and Science.

Dr. Marwan Al-Haik, I am very grateful to you for recommending me to join the Engineering Mechanics program in Fall 2015 and providing me the opportunity to work on my Ph.D. research.

Mac McCord, I greatly value your knowledge and training on the Instron machine and data acquisition system. I have learned a lot from you about how to come up with creative solutions for the experimental challenges. Without your help, my pipe bursting experiments would have been unsuccessful.

Dr. Roozbeh Kalhor, thank you for your knowledge and training on Digital Image Correlation system. You help and collaborate during the experiments was greatly appreciated.

Contents

List of Figures

List of tables

Chapter 1: Background and Literature Review

1.1. Introduction

The use of plastic pipes to carry liquids and gases has greatly expanded in recent decades because of their moderate cost, ease of handling and installation, long service life, reduced long-term maintenance, and replacement costs, and resistance to degradation compared with materials such as corrugated steel, concrete, and ductile iron. As a result of these advantages, the worldwide plastic pipe industry is predicted to grow at double-digit rates over the next five years and reach $500 billion by 2024. In the US alone, sales are expected to reach $57.3 billion, totaling 3.6 million kilometers of plastic pipe [1].

Polyethylene (PE) is among the polymers which are commonly used as the base material for plastic pipes. High Density Polyethylene (HDPE) alone accounted for the second-largest share of

plastic pipe demand in 2013 and was expected to see the strongest gains in demand through 2018 [1]. One of the most important properties of HDPE pipes is their time-dependent hydrostatic strength (stress leading to rupture) or service life under internal pressure. The three modes of plastic pipe failure in service are (1) ductile failure, as a result of plastic strain accumulation, (2) brittle failure, as a result of crack propagation, and (3) brittle failure, as a result of thermo-oxidation degradation (aging). An example of each failure modes is shown in Figures 1, 2 and 3. Due to new improvements in crack growth resistance of new generation HDPE, the brittle failure is no longer observed during the certification tests within 18 months [2]. In addition, thanks for the advances in stabilization techniques, the third stage of failure is shifted toward longer failure times and it is no longer counted as a limiting factor in the long-term performance of plastic pipes [1]. The first mode—ductile failure—is more likely to be the main cause of premature failure in relatively high stress and, thus, it is the main focus of this study.

Figure 1: Ductile failure of an HDPE pipe.

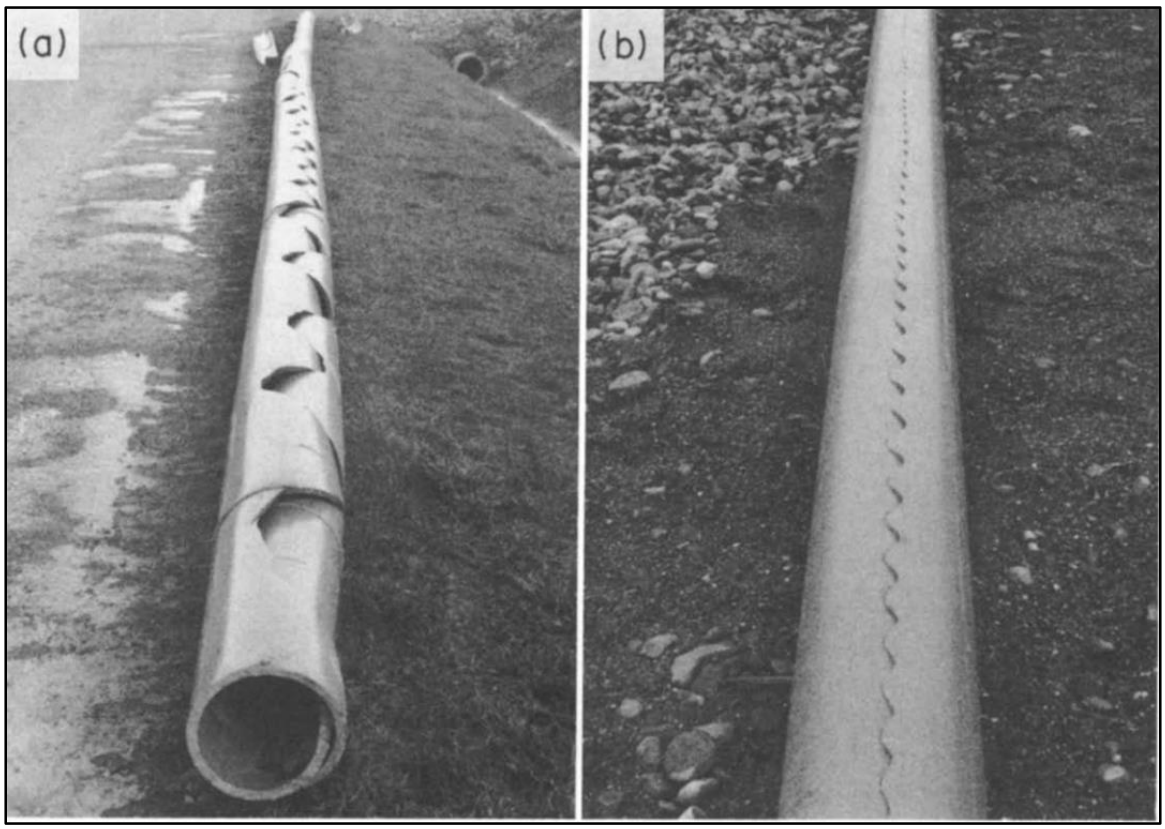

Figure 2: Brittle failure of plastic pipes due to (a) low and (b) high-speed crack propagation [3]. [Reproduced with permission]

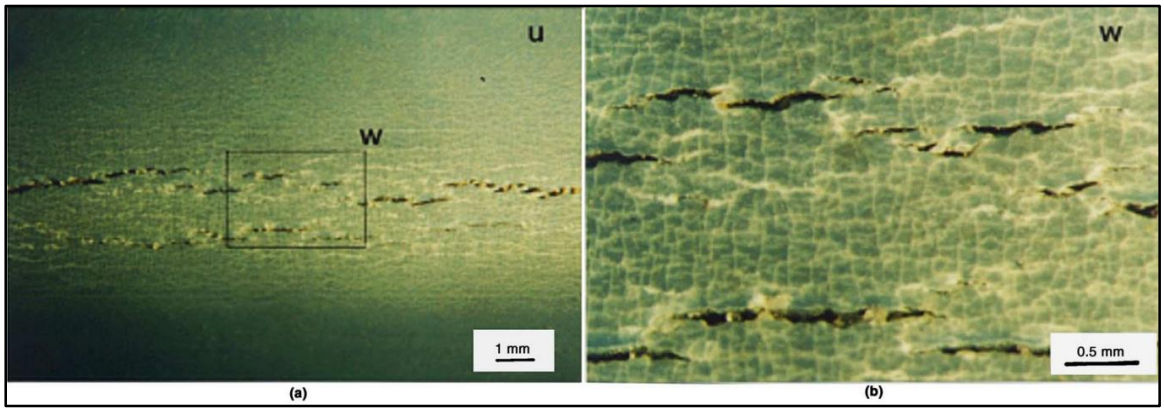

Figure 3: Brittle failure of plastic pipes due to chemical degradation. (a) Axial macrocracks. (b) Higher magnification of domain W [3]. [Reproduced with permission]

1.2. Deformation before yielding

The complicated mechanical behavior of polymers is related to the microstructural mobility and deformation of the material under applied strain. These structural deformations and changes can

be very different for different semicrystalline polymers than for amorphous polymers, complicating finding the origin of overall mechanical properties of the materials. For the case of large strains, the deformation is related to drastic morphology changes caused by slipping and entangling chains in both of the amorphous and crystalline phases as well as rearranging the crystalline lamellae. The structural changes are more complicated for higher levels of strains. In addition, the relative contributions of each motion changes as a function of temperature. For higher temperatures (above glass transition temperature) the majority of the structural changes are chain slip, local melting and recrystallization, cavitation, and shear deformation. Although several studies [3-5] have been conducted to correlate the impact of different structural motions to overall mechanical properties, due to the complexity of the morphology and interactions of different motions on each other, no comprehensive quantitative modeling is reported.

For the case of deformation before yielding, the structural changes are not as dramatic as in the large strain cases. However, these changes facilitate deeper insight into the viscoelastic behavior and local plasticity in semicrystalline polymers. During small deformation under uniaxial tension, the stretch causes the growth of nanoscale defects such as damage in crystalline phase [6] and cavitation in the interlamellar layers of the amorphous phase [7] which can reduce the material stiffness and affect its plastic behavior.

1.3. Micromechanisms of The Deformation

Figure 4 shows the microstructure changes in a semicrystalline polymer where the crystalline lamellae (bright area) grow radially and twist along their longitudinal axis [8] in spherulite domains surrounded by amorphous phase polymer (the dark area). Since the spherulites hold the orientations and the shape of the crystalline lamellae, they can be assumed as representative volume elements in the mechanics of heterogeneous materials. The mechanical behavior of the material is related to both the interlamellar and intralamellar deformation modes. However, at small strain, the deformation occurs mostly in the amorphous phase.

When the material is under tensile loading, three different domains of motions in spherulites can be identified: longitudinal, equatorial, and rotational. Figure 5 shows these three motions. The longitudinal motion can be observed in the lamellae aligned with the direction of applied strain (Figure 5 (a)). Due to significant differences in mechanical properties of lamellae and the

amorphous phase, the lamellae ribbons slip next to each other which causes inhomogeneous deformation through the region [9]. The amorphous phase, however, experiences the partial squeezing and compression between two ribbons of lamellae.

The equatorial motion, however, can be observed on the lamellae aligned perpendicular to the direction of the applied strain, see Figure 5 (b). The motion results in stretching in the amorphous region between two lamellae ribbons. An increase in the temperature facilitates the mobility of the polymer chains in the amorphous phase between the two lamellae ribbons. In the case of small deformations, the motion is reversible, however, for larger deformations, motion can result in local plastic deformation in the amorphous region and generation of nanoscale voids [10].

Due to complexity in the microstructure and differences in mechanical properties of the lamellae and the amorphous phase, the lamellae ribbons tilt along with their longitudinal direction and create rotational motion domains, as shown in Figure 5 (c). The motion is almost reversible for the small deformations. However, some degrees of irreversibility has been observed [11] which can be related to breaking of tie molecules within the crystals.

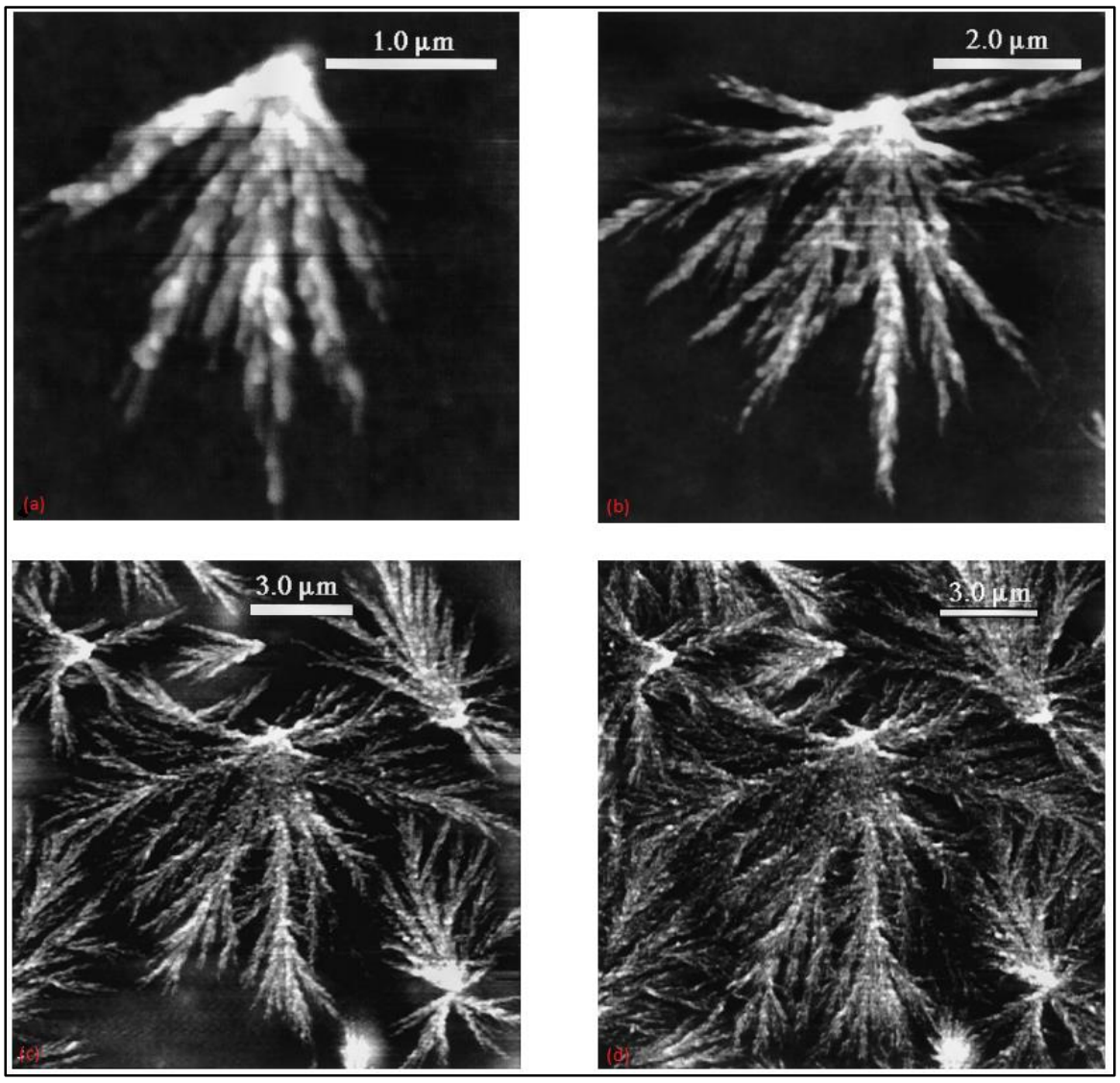

Figure 4: AFM images of the evaluation of the PEEK spherulite during the crystallization at 190°C. (a) 70 min, (b):140 min, (c) 210 min, (d) 280 min [12]. [Reproduced with permission]

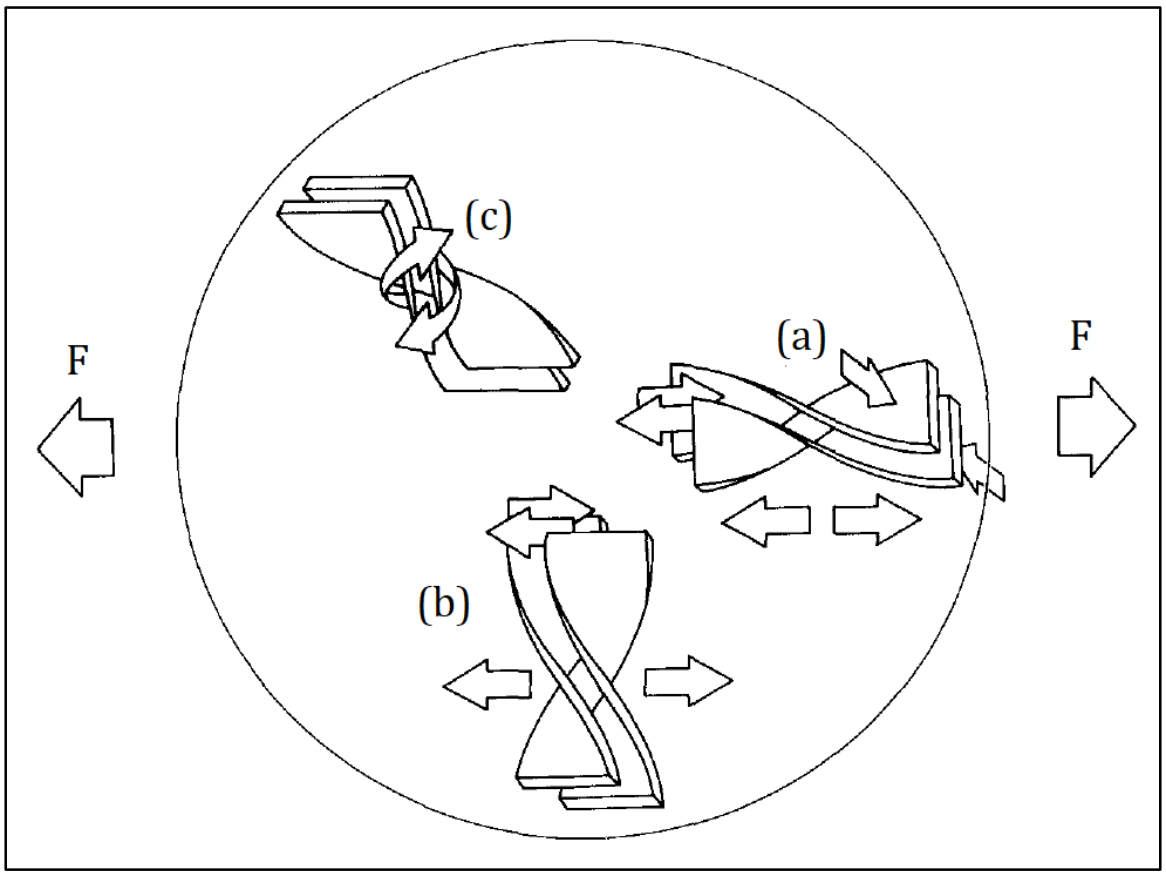

Figure 5: Local deformation motions in a spherulitic structure under tension loading. (a) Longitudinal (b) equatorial and (c) rotational motion [8]. [Reproduced with permission]

1.3.1. Microstructural Defects Before Yielding

Various microscale motions occur in the microstructure of semicrystalline materials during macroscale deformations. The structural and morphological complexity along with different mechanical properties of the crystalline and amorphous phase is responsible for these different microscale motions. In case of small strain under uniaxial tension, several microstructural defects can be introduced in the material.

Cavitation phenomenon is one of the major microstructural defects. Depending on the microstructure of the material, cavitation may or may not appear during the deformation. In the case where the lamellae are thick enough, the cavitation can be observed during deformation. The nanoscale voids decrease the local stresses of the lamellae in the equatorial and rotational motions. Voids can appear as a uniform and non-uniform distribution in different regions of the material

depends on the form of localization of deformation in amorphous regions. On the other hand, if the thickness of the lamellae was small enough, the breakage and fragmentation in them prevent the occurrence of cavitation [6]. Another study shows that cavitation occurs for some materials such as HDPE and poly (methylene oxide) while it does not occur for other materials such as low density polyethylene (LDPE) and ethylene− octene copolymer [12]. The observation supports the idea that the thickness of lamellae plays a significant role. The lamellae thickness HDPE and poly (methylene oxide) are much thicker than LDPE and ethylene− octene copolymer.

Not only does cavitation occur during large deformations, but also some studies [13, 14] indicated that even in the early stage of deformation the cavitation can be observed. Figure 6 shows small angle X-ray scattering patterns for HDPE under different levels of deformation. The results indicate that the cavitation initiates even at very low stages of deformation [14]. The occurrence of cavitation in the amorphous region and breakage in the crystalline lamellae can provide a deeper understanding of the origin of plastic deformation.

Careful AFM observations of three different semicrystalline materials under small strain tension shows that small cracks were initiated a line with the direction of the applied load which result in local breakage of lamellae [7]. The breakage in the crystal lamellae causes overall softening and nonlinear behavior in mechanical responses of the material.

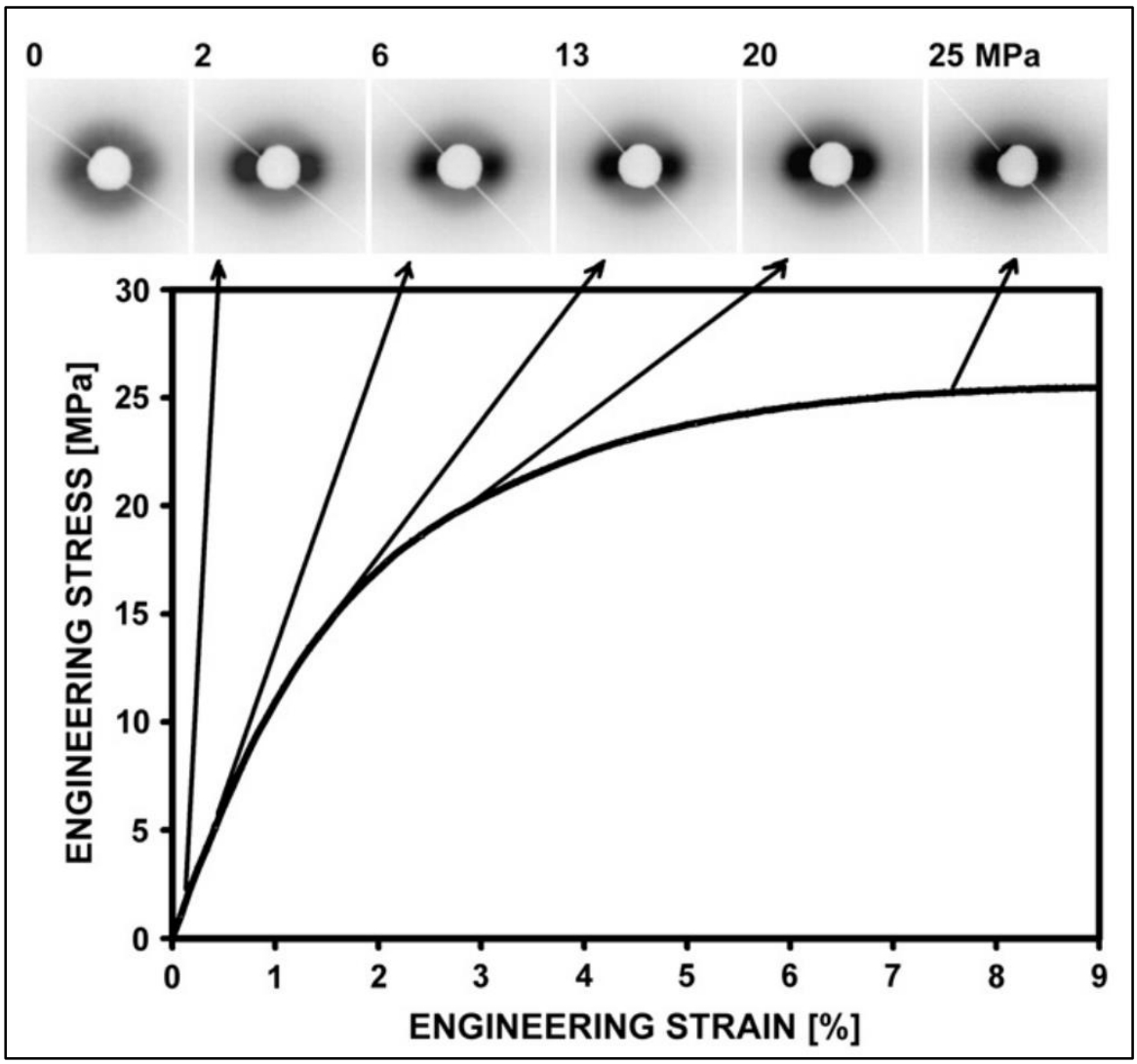

Figure 6: Small angle X-ray scattering patterns following the evolution of the cavitation during deformation [14]. [Reproduced with permission]

1.4. Mechanism of Plastic Deformation

The plastic deformation in semicrystalline materials is due to crystal slip processes which result from initiation and propagation of microscale screw dislocations into the crystalline region. During the plastic deformation, several microscale phenomena, such as kinks and texturing, were observed in different studies [15-17]. The screw dislocations were found to be initiated from a lateral surface of the crystalline region and to propagate through the crystal. Figure 7 shows the steps of dislocation propagation through the crystal. The dislocation is initiated in the lateral surface and

in the direction of the chain stem, step (1), then propagates through the crystal lamellae, step (2), and finally passes the crystal and creates a new step at the surface of the crystal region, step (3). However, due to the viscoelastic relaxation of the material, the chain stems show gradual movement [18].

In the case of polyethylene, the chain stems show a 180° twist as well as a longitudinal displacement (screw dislocation) which is reported to be the most probable defect for displacement propagation through the crystal lamellae [19]. The mechanism of moving the screw dislocation is shown in Figure 8. The 180° twist in the chain stems is initiated at one end and moves along the longitudinal direction of the chain. The chain stem undergoes a longitudinal displacement, the shear region, when the twist passes the whole length of the chain. The twist motion is transferred to neighbor chain stems and the dislocation propagates throughout the crystal lamellae [20].

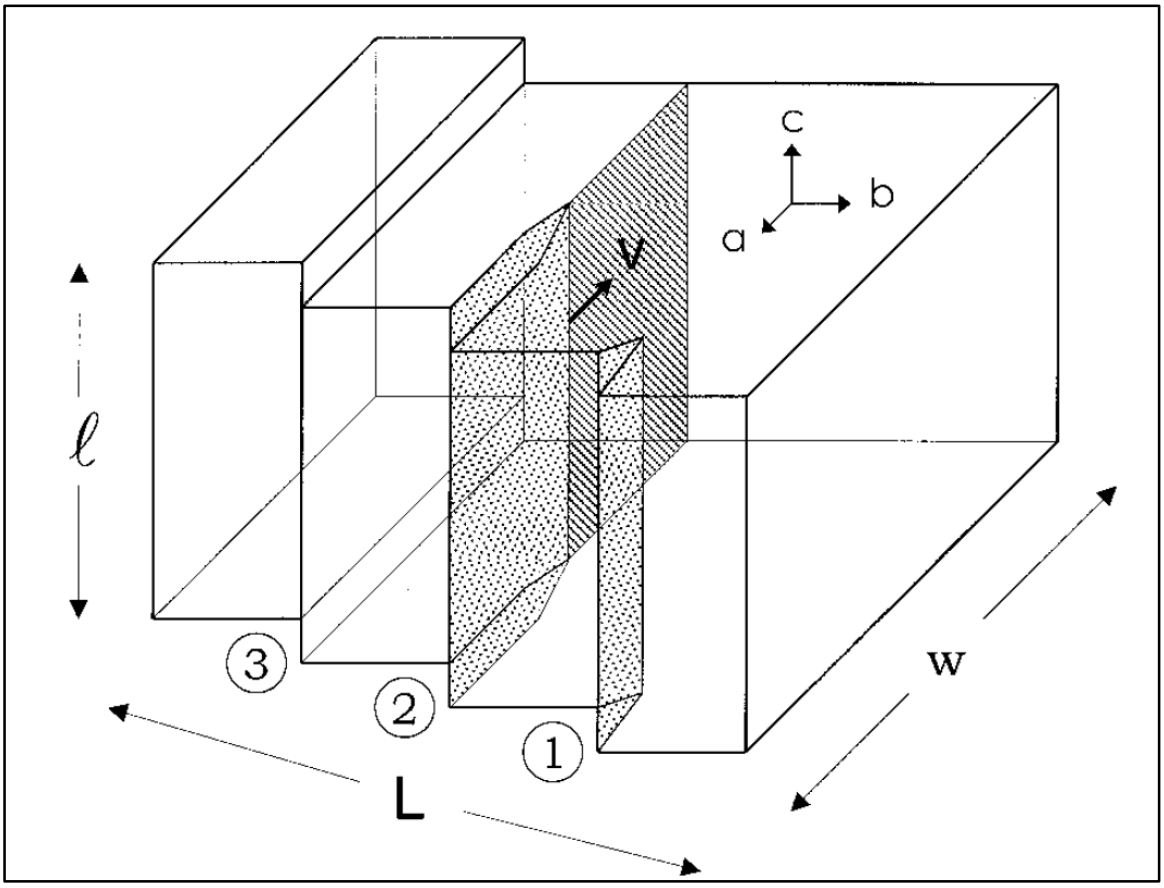

Figure 7: Small angle X-ray scattering patterns following the evolution of the cavitation during deformation [14]. [Reproduced with permission]

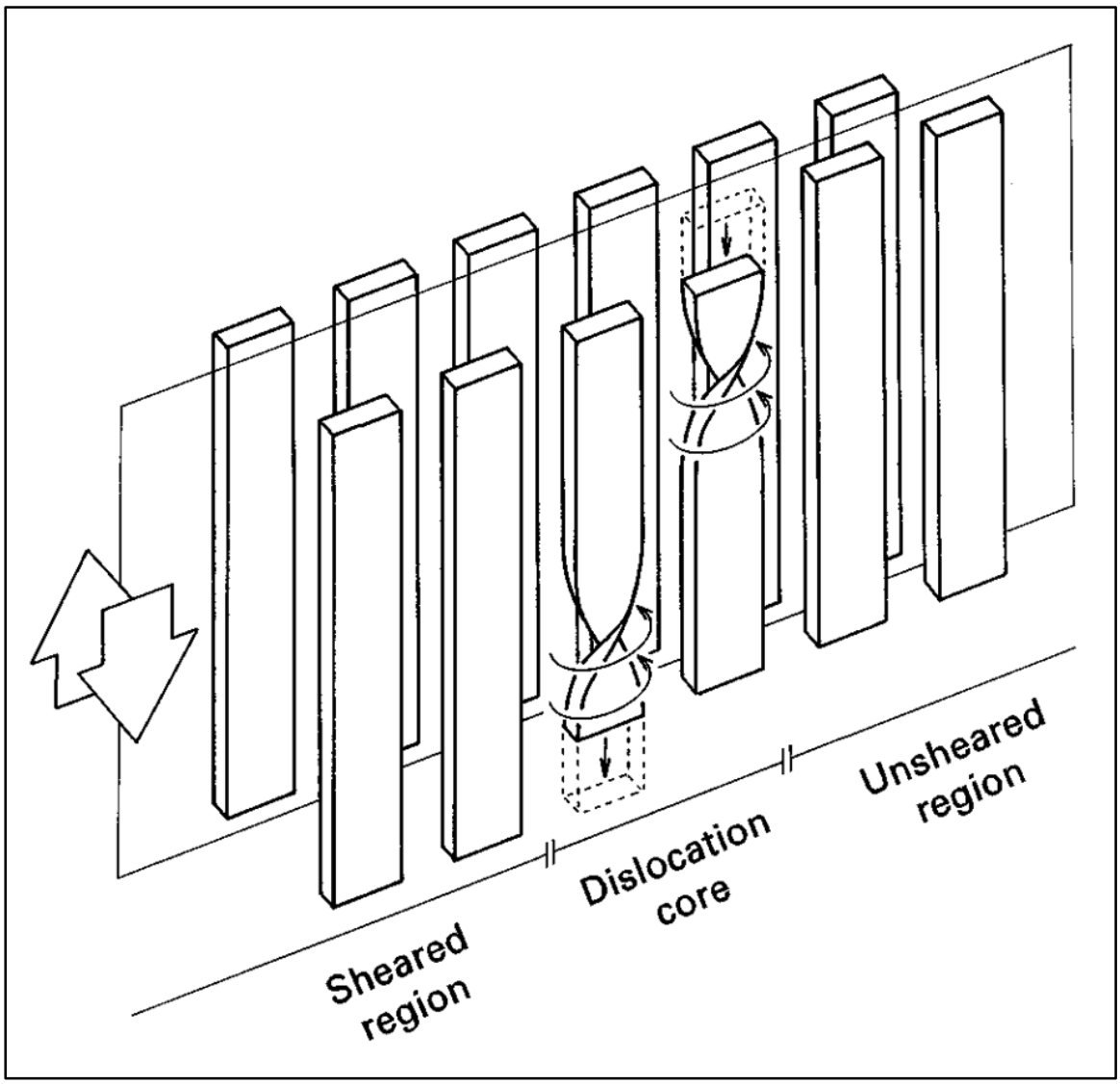

Figure 8: Screw dislocation propagation mechanism [20]. [Reproduced with permission]

At temperatures higher than glass transition of the amorphous phase, a semicrystalline polymer contains a combination of crystalline regions and a rubbery amorphous phase.

The plastic rate of strain, $\dot{\varepsilon}$, can be related to the propagation of dislocations through the material. The plastic rate of deformation depends on several features of dislocations, such as the density of dislocations, ρ, and the velocity of dislocations, V. The density of dislocations is defined as the ratio of the total length of dislocations to the total volume of the crystalline region. However, the total length of dislocations can be estimated by the number of screw dislocation, n, times the length of each screw dislocation, l. Also, the velocity of dislocations can be evaluated as the

lamellae width, w, where the dislocation can propagate within a unit of time. The velocity of dislocations is related to the rate of screw dislocation initiation ahead of the dislocation line by;

$$V = av_t \tag{1.1}$$

where v_t is the activation rate of screw dislocation initiation and a is a crystallographic parameter. Further observations [21] suggested that v_t can be estimated as the rate of crystalline relaxation, v_c, which is given as;

$$v_c = A \exp(-\Delta E/RT) \tag{1.2}$$

where ΔE is activation energy of the relaxation process, A is a pre-exponential constant, R is universal gas constant and T is the absolute temperature. For polyethylene, the activation energy of the relaxation process is independent from the crystal content as long as the crystalline lamellae are thicker than five to six monomers [21]. In addition, the rate of crystalline relaxation is found to be strongly dependent on the thickness of the crystal lamellae [22] although no explicit relationship has been found.

1.5. Failure in Plastic Pipes

The Plastic Pipe Institute (PPI) specifies a service life of at least 50-years for plastic pipes. To accelerate the rupture process in the laboratory, techniques have been developed which use the Arrhenius equation to predict the time-to-failure of the pipes [23, 24]. It is then possible to extrapolate the creep strength of plastic pipes at a lower temperature (i.e. room temperature) at longer times using the measurement at higher temperatures but at shorter times. One of the most common standards to determine the long-term hydrostatic strength of polymeric pipes is ASTM D2837. The D2837 standard requires a minimum of 18 pipe specimens to be tested in which one sample has to be placed under hydrostatic pressure for more than 10,000 hours (13 months) to produce the expected strength for 100,000 hours (50-year lifetime). In addition, Moon et al. [25] suggested two algorithmic methods, direct and interpolation, to construct the reference long-term strength lines for different temperatures. While the techniques represent a substantial acceleration in comparison to 50 years, they are still extremely time-consuming. In addition, the Arrhenius or Williams-Landel-Ferry (WLF) equations are only valid for thermo-rheologically simple polymers. However, the response of a semi-crystalline polymer such as HDPE is more complex.

In an effort to address this complex behavior, an accelerated testing method was suggested by Popelar et al. [26] where horizontal and vertical shift functions were used to superpose the long-term hydrostatic pressure data in different temperatures and create a master curve that is able to predict the lifetime service of PE pipes. Figure 9 shows an example of superposition shifting of long-term hydrostatic pressure data for HDPE pipes. The tests were conducted at 4 different temperatures and under constant internal pressure. By taking the $20℃$ as the reference temperature, the master curve, Figure 9 (b), was constructed using horizontal and vertical shifting functions, as;

$$H_T = \exp\big(-0.109(T - T_r)\big) \tag{1.3}$$

$$V_T = \exp\big(-0.0116(T - T_r)\big) \tag{1.4}$$

where, H_T and V_T are horizontal and vertical shift factors, respectively, and T_r is the reference temperature. In the case where the long-term hydrostatic data exist at an elevated temperature for a PE pipe, the failure time at the operating temperature can be evaluated by using the horizontal shift factors in the following equation.

$$t_f(T_r) = t_f(T)/H_T \tag{1.5}$$

The required hoop stress associated with the evaluated failure time, also, can be evaluated using the vertical shift factor as

$$\sigma(T_r) = V_T\sigma(T) \tag{1.6}$$

By using this accelerated technique, the design hoop stress corresponding to a 50 year lifetime for the pipe at operating temperature, $20℃$, is evaluated to be twice the hoop stress that causes failure in the pipe at $80°C$ during 650 hours of hydrostatic testing [26]. Although this technique shows a significant reduction on the required testing time from 10,000 hours, the method is developed based on the existence of long-term hydrostatic data at different elevated temperatures. The hydrostatic testing under a controlled pressure and at different elevated temperatures requires very special uncommon experimental setup and also at least a couple of months of testing time. Thus, the method is costly and time-consuming to practically use in robust pipe design projects.

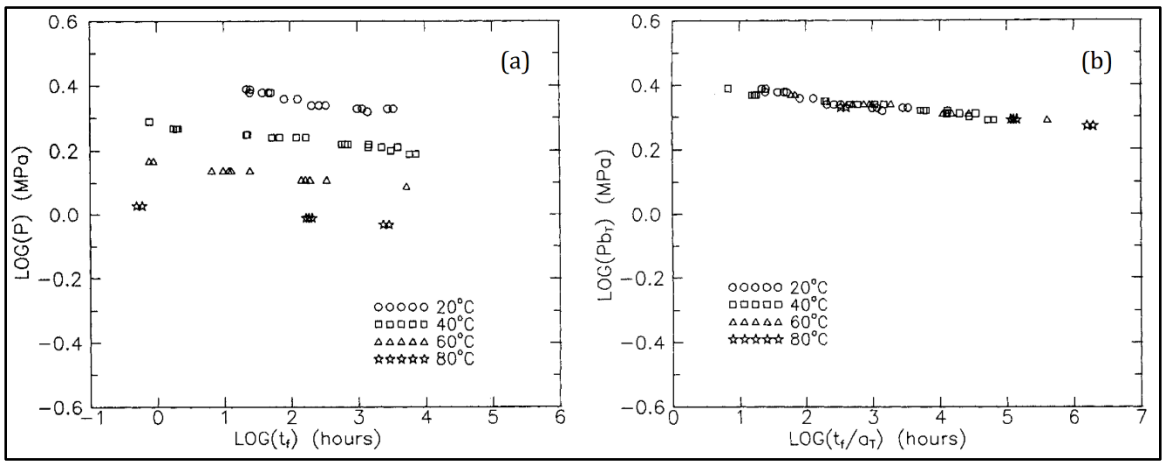

Figure 9: (a) Long-term hydrostatic pressure test data for HDPE pipes, (b) master curve constructed by horizontal and vertical shiftings of the data [26]. [Reproduced with permission]

Another accelerated testing method was recently developed [27] to predict the plasticity-controlled failure (ductile failure) of HDPE pipes based on two thermally-activated Eyring processes. Several uniaxial tensile and compression tests were performed on compression-molded samples from an HDPE resin to develop a hydrostatic pressure modified Eyring model and characterize the yield kinetics of the material. In addition, several uniaxial creep tests were performed using compression-molded samples in order to evaluate the critical strain which is required to estimate the time of failure. Experimental data from hydrostatic pressure tests were adopted to validate the model. The model prediction shows reasonable agreement to the experimental data. However, while conducting the characterization tests on flat plaques is convenient in that it allows the use of standard mechanical testing equipment, matching of the processing conditions is required to achieve the same material state as in the as-manufactured pipes. In addition, a combination of parameters such as degree and direction of molecular orientation, the cooling rate of the melt, injection pressure in the extrusion process, and the type of polymer (amorphous or semi-crystalline) may introduce a complex structure into an as-manufactured pipe that is difficult or impossible to imitate in compression-molded samples. Alternatively, one can perform the characterization directly on as-manufactured pipes. A complication is that additional fixturing is required; however, it eliminates the need to attempt to match the state of the as-manufactured material. In addition, conducting characterization on as-manufactured pipes enhances the ability to study the impact of different processing condition on the products. Thus, a new testing procedure is introduced in Chapter 2 where as-manufactured pipe

segments were studied directly. The presented model requires only 10 days of testing to develop an accurate prediction of long-term performance of the HDPE pipes.

One can employ numerical simulation to overcome some of the limitations of experimental approaches. Despite many experimental studies on long-term creep behavior of plastic pipes, very few numerical simulation and modeling studies have been conducted. Kuhl et al. [28] suggested a numerical model describing the nonlinear viscoelastoplastic creep behavior of HDPE pipes at small strains. Cheng et al. [29] used the finite element method to analyze the primary and secondary creep behavior of HDPE pipes and also to estimate the overall lifetime of the pipes. The suggested constitutive model was developed by employing a fitting process of a general formula to the actual data from very time consuming long-term creep tests. However, for accelerated characterization purposes, it is desirable to develop a combination of a comprehensive numerical simulation with short-term mechanical testing to model the long-term creep rupture behavior of plastic pipes at different variable working temperatures and loadings. Thus, a numerical model is presented in Chapter 3 where short term experiments were employed to develop the material characterization model.

1.6. Residual Stress

Residual stresses in the extruded thermoplastic pipes are introduced during the cooling process where a cold water spray is used to cool down hot recently extruded pipes. The residual stresses are the result of the non-uniform temperature gradient. During the cooling process, the outside layers of the material solidify at much higher rates than the inside and middle layers. Variation in cooling rate causes variation in the thermal expansion of the material across the thickness of the pipes which results in tensile and compression residual stresses. During the cooling process, the outside layers of the material freeze at a higher rate in comparison to the inside and middle layers. Therefore, the outside of the pipe solidifies while the inside of the pipe is still warm and soft. The fast cooling rate of the outside layers locks in the microstructural arrangement and limits the crystallization process. However, the slower cooling rate in the inside layers of the pipe allows the material to crystallize. The cold, solid outside layers limit the thermal shrinkage of inside layers. Consequently, the continuity between layers causes the generation of compressive and tension residual hoop stress on the outside and inside layers of the pipe, see Figure 10 (b).

Several different experimental procedures were suggested to evaluate the distribution of residual hoop stresses. However, most of the procedures involve axial slitting of the pipe rings and their deflection measurements. An experimental method was introduced by Williams et al. [30, 31] where a different amount of material was removed from inside and outside of several rings of a high density polyethylene pipe. Then, the rings were cut axial in two to allow the material to deform as a result of relaxing the residual hoop stress. Since the material shows a significant time-dependent response, the deflection of the cut rings was measured over a period of 1000 hours.

The corresponding curved beam deflection formulation was employed to relate the measured deflection of the cut rings to the amount of released bending moment, and then, to the residual hoop stress distribution across the thickness of the pipe. Figure 10 shows a schematic illustration of a section of the pipe and the bending moment caused by a non-uniform distribution of residual hoop stress through the thickness of the pipe. For the case where the material was removed from outside of the pipe, the residual hoop stress was evaluated by

$$\sigma_h(t) = \frac{E}{12\pi r_i^2}\left(4t\delta + t^2\frac{d\delta}{dt} + 2\int \delta dt\right) + \sigma_0 \tag{1.7}$$

For the case where the material was removed from inside of the pipe

$$\sigma_h(t) = -\frac{E}{12\pi r_o^2}\left(4t\delta + t^2\frac{d\delta}{dt} + 2\int \delta dt\right) + \sigma_0 \tag{1.8}$$

where, r_i and r_o are the original inner and outer radius of the pipe, respectively. Here, $\delta(t)$ denotes as the deflection of the cut rings in term of the thickness, t, and σ_0 is a constant which was evaluated by using the condition of balance of hoop stress though the thickness of the pipe [30, 31], as

$$\int_0^{r_o - r_i} \sigma_h dt = 0. \tag{1.9}$$

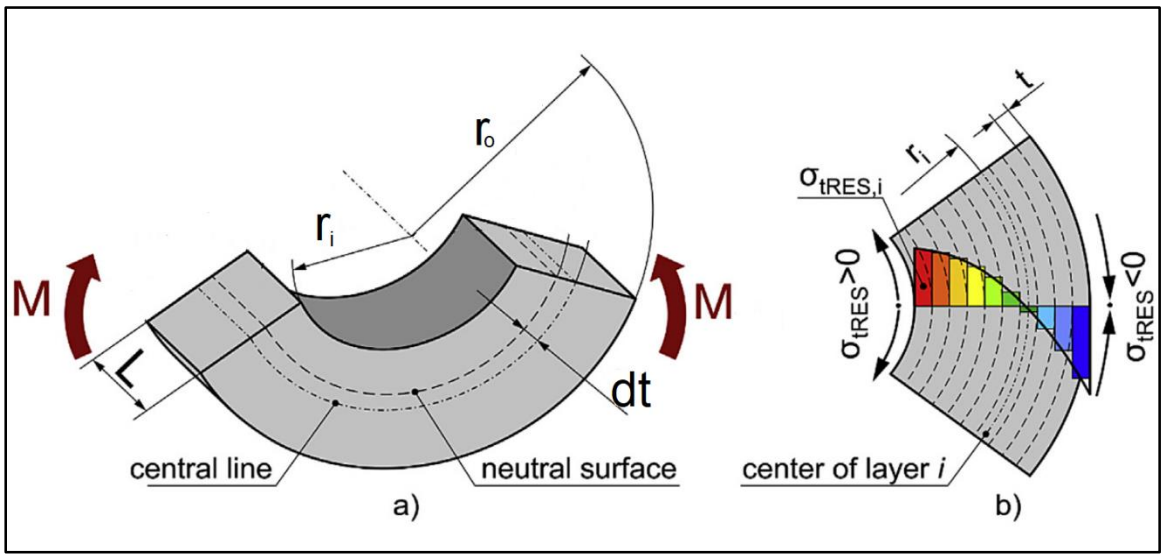

Figure 10: a) A section of the pipe which can be considered as a curved beam under pure bending moment caused by residual hoop stress. b) The form of residual stress through the thickness of the pipe [32]. [Reproduced with permission]

Later, another study [32] was conducted to evaluate the residual stresses in the extruded plastic pipes using the deflection measurement of cut rings technique. Polypropylene pipes with different dimensions were chosen and 13 different rings were cut out of each pipe. Among them, six rings were machined from the outside and six other rings were machined from the inside and one ring was kept in its original pipe dimension, as shown in Figure 11. Then, the rings were cut axially and the corresponding deflections were measured over time. The curved beam and thick-walled cylinder theories were utilized to estimate the residual stress. The distribution of residual hoop stress evaluated for different pipes was compared to each other. The observations from [32] suggest that the magnitude of residual hoop stress is independent of the dimension of the pipes. This observation seems to be contradictory to the origin of residual stress. For pipes with higher SDR (the ratio of outer diameter to the thickness) the gradient of temperature during the cooling process is lower than lower SDR pipes. In other words, in thicker pipes, a higher temperature variation exists across the thickness of the pipe with compare to thinner pipes during the cooling process. The residual stress results from the gradient of temperature. Therefore, we would expect that the magnitude of residual stress would depend on the geometry of the pipes. Because of higher temperature variation in thicker pipes, a higher magnitude of residual stresses is expected.

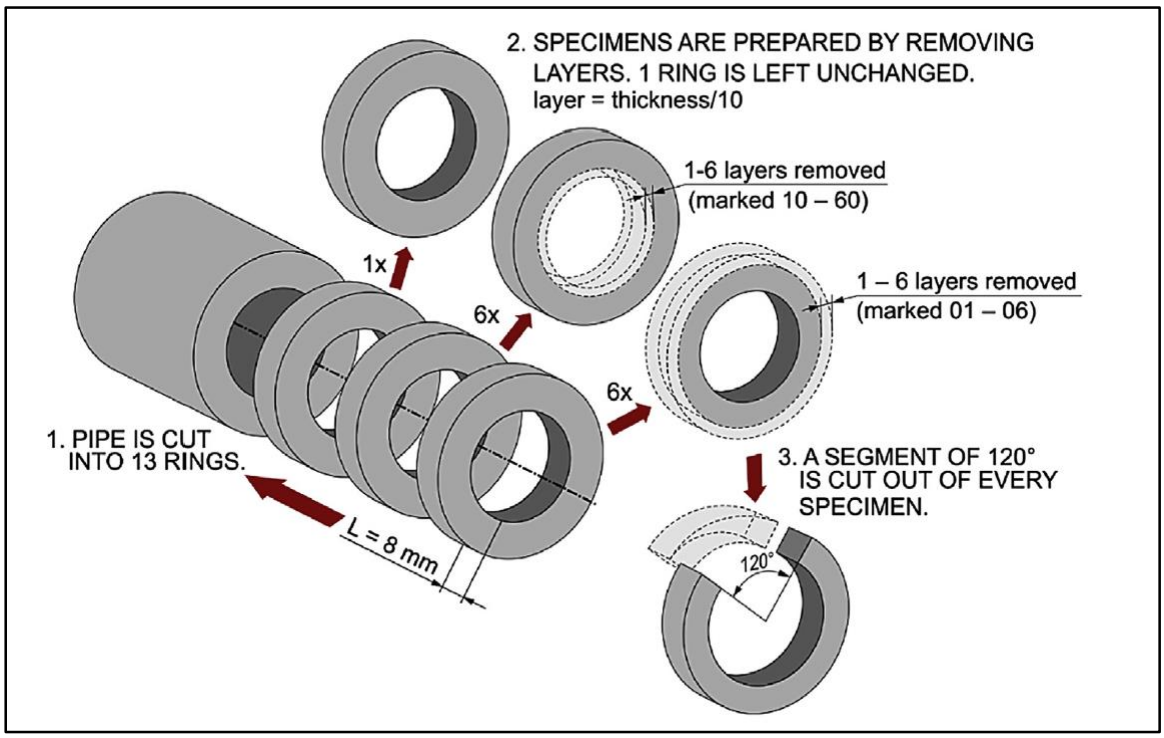

Figure 11: Cut rings preparation steps [32]. [Reproduced with permission]

Krishnaswamy [33] conducted several hydrostatic pressure tests on two sets of dimensionally different polyethylene pipes to study the effect of residual stress on the creep rupture of the pipes. The pipes were made from the same resin and under the same production conditions. The tests were conducted at two temperatures: $23°C$ and $80°C$. The results of hydrostatic pressure tests are shown in Figure 12 for the both pipes and at $23°C$ and $80°C$. Based on the results, it was concluded that the tensile portion in the residual hoop stress accelerated the creep rupture and the ductile fracture of the pipe. Therefore, the lower level of residual stress, as in SDR 17, was concluded to be favorable for creep rupture.

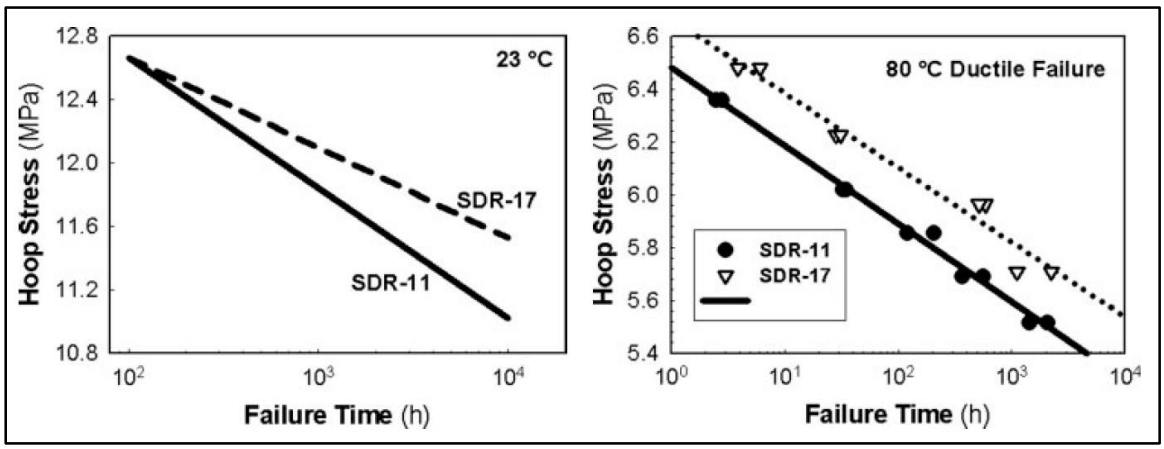

Figure 12: Results of Hydrostatic pressure tests for two different PE pipes at 23°C and 80°C [33]. [Reproduced with permission]

1.7. Overview

This work focuses on the long-term performance of HDPE pipes. The pipes are widely used for water and gas transportation across the world, thus, quick evaluation of the long-term performance of the pipes is very important in the plastic pipe industry. In the second chapter, an accelerated testing method is presented to evaluate the long-term performance of pipes made of semi-crystalline polymers. As-manufactured high density polyethylene pipes were subjected to several tensile and compression tests. The plastic flow Eyring model was employed to characterize the yield kinetics of the material. The long-term performance of the pipes was estimated using the developed model and the predictions were validated by actual long-term experimental data. The presented accelerated technique required only 10 days of testing to predict the 50-year service life of the pipes. Using as-manufactured pipes enhances the ability to study the different processing conditions effects on the performance of the pipe and eliminates the need for matching the state of testing material to the pipe material.

In the third chapter, a finite element numerical modeling is presented. The model is based on the developed plastic flow model reported in Chapter 2. The numerical model is used to simulate the tensile tests at different temperatures and strain rates as well as the hydrostatic pressure (burst) tests under different internal pressure. The results of the simulations are validated with the experimental data. In addition, the numerical model is used to study the effects of variation in

working temperature on the performance of the pipes by simulating the hydrostatic pressure (burst) tests at a daily variable working temperature.

The fourth chapter focuses on the state of the residual hoop stress in the pipes. The distribution of residual hoop stress across the pipe thickness is evaluated for pipes with three different geometries (SDR 9, 11, 13) to investigate the effects of pipe geometry on the residual stresses. Then, the evaluated residual hoop stresses are used along with the numerical model developed in Chapter 3 to study the effect of residual hoop stress on the long-term performance of the pipes.

This dissertation wraps up with an overall summary and conclusion as well as recommended future work.

Chapter 2: Accelerated Testing Method to Estimate the Long-Term Hydrostatic Strength of Semi-Crystalline Plastic Pipes

2.1. Introduction

The ability to quickly develop predictions of the service lifetime of plastic pipes at different load levels allows designers to choose the best plastic material and pipe design for a specific application. Additionally, it helps material producers to rapidly design, manufacture, test, screen, and modify the base polymeric material. The aim of this study is to introduce a combined experimental and analytical framework to develop accelerated lifetime estimates for semi-crystalline plastic pipes which is sensitive to the structure, orientation, and morphology changes introduced by changing processing conditions. To accomplish this task, High Density Polyethylene (HDPE) is chosen as the exemplary base material and custom fixtures are developed to admit tensile and hoop burst tests on the as-manufactured HDPE pipes. A pressure-modified Eyring flow equation is employed to predict the rupture lifetime of HDPE pipes using the measured mechanical properties under axial tensile and hydrostatic pressure loading in different temperatures and strain rates. The method allows the prediction of pipe service lifetimes in excess of 50 years using experiments conducted over approximately 10 days instead of the traditional 13 months.

2.2. Material

All pipes were provided by LyondellBasell Industries (Cincinnati Technology Center, OH) with SDR 11 configuration made of an HDPE resin (PE100 pipe grade). The average outside diameter and the thickness of the pipe are $33\,mm$ and $3\,mm$, respectively. The variability in the pipe thickness was small (less than $\pm 1.5\%$) and was not explicitly included in this study.

2.3. Method

It has been suggested [34] that for a constant temperature, the product of time-to-failure, t_f, and strain rate at the failure is constant and independent of loading. This constant value indicates the amount of accumulated plastic strain at the failure, called critical strain, ε_{cr}. Later studies [35-37] indicated that the same relation exists between t_f, the plastic flow rate (the strain rate in the secondary creep region), $\dot{\varepsilon}_p$, and ε_{cr}.

$$t_f(\sigma, T) = \frac{\varepsilon_{cr}}{\dot{\varepsilon}_p(\sigma, T)} \tag{1}$$

The critical strain is associated with the accumulated plastic strain at the failure, and it was reported to be constant and independent of stress level [2, 35]. The critical strain can be evaluated using creep experiments; however, determination of the plastic flow rate for small creep loads is extremely time-consuming. Therefore, an alternative quick way is required to estimate the plastic flow rate.

In a different study [38], the secondary creep region was demonstrated to be identical to the yielding region in a constant strain rate test for polycarbonate. In other words, the state of yielding in uniaxial loading under constant strain rates is equivalent to the state corresponding to the secondary creep region in the creep experiments. Based on this important point, the plastic flow rate can be evaluated using uniaxial tensile and compression tests by employing the Eyring plastic flow processes [39, 40]. To predict the stress and temperature dependence of the plastic flow rate, $\dot{\varepsilon}$, a Eyring activated flow relation, originally proposed by Eyring [39] and then developed in [40, 41], was adopted:

$$\dot{\varepsilon} = \dot{\varepsilon}_0 \exp(-\Delta E/kT) \sinh\left(\frac{S_y V}{kT}\right) \tag{2}$$

where

S_y: Yield stress

$\dot{\varepsilon}_0$: A constant pre-exponential factor

T: Absolute temperature

ΔE: Activation energy

V: Activation volume

k: Boltzmann's constant

Other studies [38, 41-47] of yield stress over a wide range of temperature and strain rates on a number of polymers indicate that one Eyring process does not sufficiently describe the yield behavior. An explanation for this discrepancy is that there are multiple Eyring processes working in parallel. Consequently, the total yield stress for two such processes can be calculated by adding the yield stress evaluated based on each Eyring process, or:

$$\begin{aligned} \frac{S_y}{T} &= \frac{S_{y_1}}{T} + \frac{S_{y_2}}{T} \\ &= \frac{k}{V_1} \sinh^{-1}\left(\frac{\dot{\varepsilon}}{\dot{\varepsilon}_{0_1}} \exp\left(\frac{\Delta E_1}{kT}\right)\right) \\ &+ \frac{k}{V_2} \sinh^{-1}\left(\frac{\dot{\varepsilon}}{\dot{\varepsilon}_{0_2}} \exp\left(\frac{\Delta E_2}{kT}\right)\right) \end{aligned} \tag{3}$$

where subscripts 1 and 2 are associated with two Eyring processes and the parameters have the same meaning as in equation (2) but are related to the first and second processes.

The effect of hydrostatic pressure on yield stress was specifically investigated in several studies [40-42, 48, 49] where it determined that a hydrostatic pressure increases the activation energy of each Eyring processes. As a result, equation (2) can be modified [41] as

$$\dot{\varepsilon} = \dot{\varepsilon}_0 \exp(-\tfrac{\Delta E}{kT} - \tfrac{p\Psi}{kT}) \sinh\left(\tfrac{S_y V}{kT}\right) \tag{4}$$

where Ψ is the pressure activation volume. In equation (4), p is the hydrostatic pressure within the pipe material which can be determined using;

$$p = -\tfrac{1}{3}(\sigma_1 + \sigma_2 + \sigma_3) \tag{5}$$

where σ_1, σ_2 and σ_3 are the principal stress components. For uniaxial tensile and compression loading, p is given as $-\frac{\sigma}{3}$ and $\frac{\sigma}{3}$, respectively, where σ is the absolute value of axial stress. For a

thin-walled pipe in the case of biaxial creep (burst) tests, the principal stresses are the hoop stress, σ_h, and axial stress, $\sigma_a = \frac{\sigma_h}{2}$. Thus, the hydrostatic pressure can be determined as $p = -\frac{\sigma_h}{2}$. It is noteworthy that the hydrostatic pressure term used in equation (4) is not the same as the internal pressure in the biaxial creep (burst) tests. Using equation (4), equation (3) can be reformulated as

$$\frac{S_y}{T} = \frac{k}{V_1}\sinh^{-1}\left(\frac{\dot{\varepsilon}}{\dot{\varepsilon}_{0_1}}\exp\left(\frac{\Delta E_1}{kT} + \frac{p\Psi_1}{kT}\right)\right) + \frac{k}{V_2}\sinh^{-1}\left(\frac{\dot{\varepsilon}}{\dot{\varepsilon}_{0_2}}\exp\left(\frac{\Delta E_2}{kT} + \frac{p\Psi_2}{kT}\right)\right) \quad (6)$$

where, Ψ_1 and Ψ_2 are pressure activation volume for processes 1 and 2, respectively. While Kanters et al. [2] suggest a single pressure modification term, other studies [41-43, 48] suggest that the effect of hydrostatic pressure is significantly different for each process and cannot be considered to be the same. For instance, in Truss et al study [41], the pressure activation volume for process 1 was found to be 114-145% higher than that for process 2. Thus the pressure effect on each of the processes should be considered separately.

In equation (6), two activation energies, two activation volumes, two constant pre-exponential factors, and two pressure activation volumes are material parameters that need to be evaluated experimentally. To do so, several mechanical tests including uniaxial tensile tests under different strain rate and at different temperatures and uniaxial compression tests at different temperatures and under different strain rates are employed.

2.4. Material Characterization

To measure the molecular weight values and distribution of the HDPE resin, a PolymerChar GPC-IR instrument, equipped with infrared detector and online viscometer was used with three Agilent Olexis columns and 1,2,4-trichlorobenzene (TCB, stabilized with 300 ppm 2,6-di-tert-butyl-4-methyl-phenol) as solvent at 145° C and at a constant flow rate of 1 mL/min. An amount of about 300 µL of sample solution was injected per analysis. The column was calibrated using a relative calibration with 12 narrow MWD polystyrene (PS) standards in the range of 0.474 kg/mole to 3,510 kg/mole. All samples were prepared by dissolving 16 mg of sample in 8 mL (at 160° C.) of stabilized TCB (same as mobile phase) and maintaining for 1 hour with continuous shaking prior sampling in the GPC instrument.

DSC measurements were performed in a nitrogen atmosphere using a TA Instruments Q1000 DSC. The samples were (1) ramped up by 10°C/min rate to 160°C (2) kept isothermal for 5 mins

(3) ramped down by 10°C/min rate to 0°C and finally (4) ramped up again at 10°C/min to 160°C. DMA measurements were also performed using TA Instruments Q800 DMA in a single cantilever mode with an oscillation amplitude of 20 m at a frequency of 1 Hz. The samples were (1) equilibrated at -150°C for 5 minutes and then (2) ramped up by 3°C/min to 130°C.

Small angle X-ray scattering (SAXS) and wide angle X-ray diffraction (WAXD) were conducted to study the morphology of the material and to ensure that the material is isotropic and, thus, the von Mises expressions is appropriate to define the equivalent stress in the Eyring model. SAXS experiments were executed using a Rigaku S-Max 3000 3 pinhole SAXS system, equipped with a rotating anode emitting X-ray with a wavelength of 0.154 nm (Cu Kα). The sample-to-detector distance was 1605 mm, and the q-range was calibrated using a silver behenate standard. Two-dimensional SAXS patterns were obtained using a fully integrated 2D multiwire, proportional counting, and a gas-filled detector with an exposure time of 2 h. All SAXS data were analyzed using the SAXSGUI software package to obtain radially integrated SAXS intensity versus scattering vector q, where $q = \left(\frac{4\pi}{\lambda}\right) sin(\theta)$, θ is one half of the scattering angle, and λ is the wavelength of X-ray. SAXS profiles have been corrected for sample thickness and transmission. In the WAXD test, two-dimensional diffraction patterns were obtained using an image plate, with an exposure time of 2 hours, using the Rigaku S-Max 3000 3 pinhole SAXS system. All WAXD data were analyzed using the SAXSGUI software package to obtain azimuthal averaged WAXD intensity versus 2θ profiles, where θ is one half of the scattering angle. WAXD profiles were vertically shifted to facilitate a comparison of the diffraction profiles.

2.5. Mechanical Testing

In this work, we employed a new tensile and compression testing procedure in which as-manufactured pipe segments have been used as the test samples. The strain was measured using the Digital Image Correlation (DIC) technique. The DIC measurements were conducted using two Prosilica GE cameras (Allied Vision Technologies) and with two 60mm Nikon lenses in conjunction with Vic-Snap 8 and Vic-3D 7 software. The DIC system was calibrated before each test. The average intersection deviation error of all 3D points was less than the maximum recommended value of 0.3 [50]. Subsequently, the strain in x and y directions were determined

using the captured images in which each image taken by cameras was divided by square facets with a size of 23-pixels and a facet distance of 15-pixels. These measurements were used to verify that the specified strain rate is consistent with the observed strain rate and that the strains are uniform within the gage length.

A threaded fixture was designed for SDR 11 pipes. One fixture was screwed into each end of 254-mm-long pipe segments. To reduce the potential effect of stress concentration resulting from the sharp edges of the thread, the fixture was cut with a very slight angle from the top. As a result, no sharp edge was present on the thread at the start of the gage length on both sides. Subsequently, the samples were speckled with white paint to provide a high contrast pattern for the DIC measurements of the deformations during tests. Four STBC131 T hose clamps from Thaman Rubber Co. (Cincinnati, OH) were also used on each side to firmly fix the segments on the fixture (Figure 13(a)-(c)). A torque wrench was also used to apply 10.17 N·m torque to the clamps.

The tensile response of the pipes was measured using a screw-driven INSTRON® load frame with a 50 kN load cell (MTS ReNew^{TM} Upgrade Package). An INSTRON® chamber was mounted on the load frame to provided controlled elevated temperatures by using an INSTRON® temperature controller model 3116. The samples were tested at different strain rates and under 4 different temperatures: room temperature (20℃), 42℃, 60℃, and 80℃. The constant applied strain rate, the constant applied temperature, the strains, and the axial stresses were reported for each experiment.

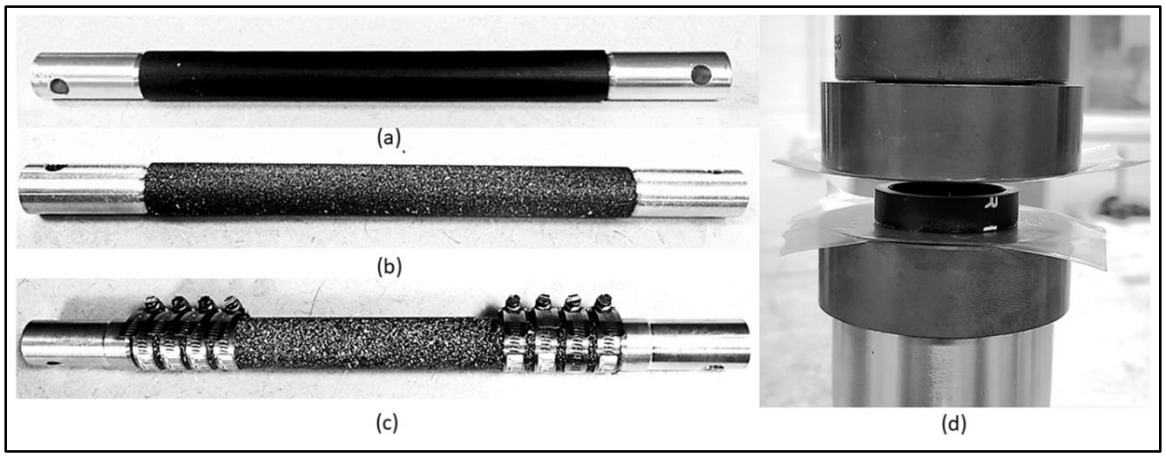

Figure 13: Tensile sample preparation, fixtures were screwed into the sample(a), the sample was speckled with white color paint spray (b), the clamps were mounted on each side (c). Compression specimen placed between the two platens covered with the Teflon® tape

In addition to the tensile tests, compression tests provide the second state of stress which can be used to evaluate the parameters of equation (6). The compression tests were conducted on pipe rings with 7 mm length carefully cut using a SHARP® lathe. Then, the specimens were placed between two smooth flat stainless steel platens which were mounted on a screw-driven INSTRON® load frame with a 50 kN load cell (MTS ReNewTM Upgrade Package). Significant experimental concerns with compression tests are the possibilities of global buckling, wrinkling, or barreling which are practically difficult to control. To address these concerns and find meaningful yield stress from compression tests, ultra-slippery-Teflon® PTFE tape, and high-performance-white-lithium-grease sprays as lubricants were employed on both ends of each compression sample. A constant axial displacement rate was applied to the specimens by the INSTRON® machine and the corresponding applied loads were measured. Figure 13 (d) shows a specimen placed between the two platens covered with the Teflon® tape and the lubricant spray on the INSTRON® machine. To observe the two Eyring processes the tests were conducted at two temperatures (21°C and 60°C), and under different strain rates. At the end of each test, the constant applied strain rate and the axial stresses were reported.

To evaluate the critical strain and also to validate the model, biaxial creep tests (in the form of burst or hydrostatic pressure tests) were conducted using a custom-developed system. The samples were cut into 254 mm long sections, speckled with white paint, and placed between end caps (Figure 15 (a)). Subsequently, water was pumped, using a MAXIMATOR® air driven liquid pump type PP8, through the system to purge the trapped air, and the sample and the reservoir were filled with water. Finally, all the valves were closed and compressed nitrogen (N_2) gas was charged into the reservoir by using a TESCOM® gas regulator. To maintain a constant pressure, a feedback pressure control system was developed. The system measures the internal pressure using an OMEGA pressure transducer, model NO: PX309-1KG5V, and then sends the data to the data acquisition software (National Instruments LabVIEW 2011). The data acquisition software analyzes the data and sends an on/off signals to an electronically activated solenoid valve (Normally closed 24V Peter Paul Electronics Safety Valve 20/EH22). The valve is mounted on the nitrogen tank and feeds the system if needed. Figure 14 shows a schematic of the setup and the actual system. To measure the strains in axial and hoop directions, DIC measurements were employed and the imaging rate was adjusted based on the time of experiments. Each test was

repeated at least two times to make sure consistent results. Finally, the constant applied pressure, the time to failure, and the strains were reported for each experiment.

2.6. Material Characterization Results

The HDPE resin utilized in this study melts at 129℃, has a bimodal distribution of molecular weight, possesses a glass transition temperature of -115.9 ℃. The values are measured by DSC, DMA, and GPC, respectively. The polydispersity index (PDI) of the material is 26.4. The M_n, M_w, and M_z values are $9.5 \times 10^3 \frac{g}{mol}$, $2.51 \times 10^5 \frac{g}{mol}$, and $1.3 \times 10^6 \frac{g}{mol}$, respectively.

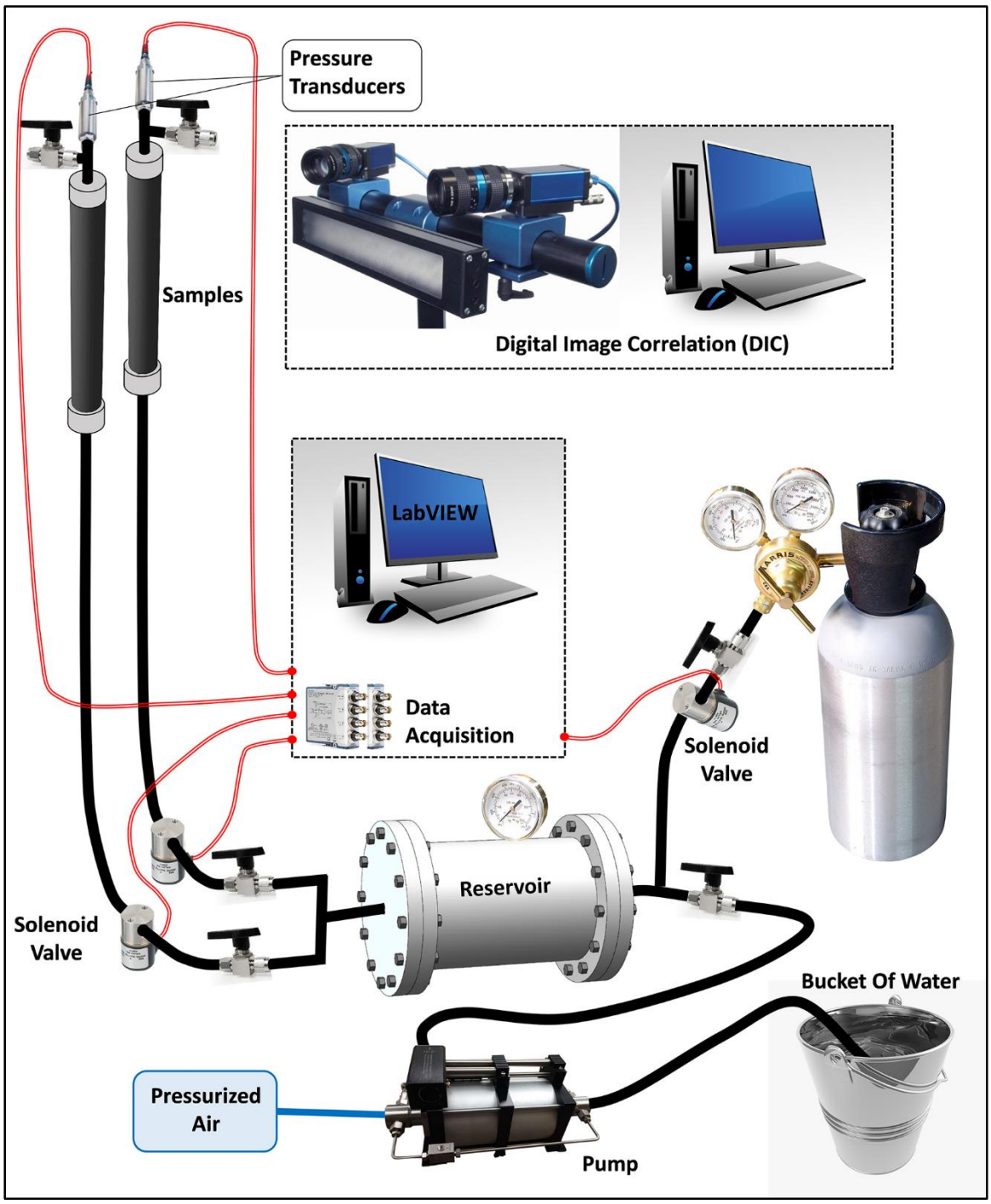

Figure 14: Schematic of the hydrostatic pressure (burst) test setup.

Figure 15: (a) the actual test set-up with two specimens during the test, and (b) The image of pipe ductile failure as the result of constant internal pressure at room temperature.

SAXS was used to study the three-dimensional morphological arrangement of crystallites formed during processing of the SDR 11 pipes. The resulting spectrum, Figure 16, shows a primary scattering maximum at 0.27 nm^{-1} and a secondary maximum at 0.70 nm^{-1}. The presence of multiple scattering maxima indicates that the crystallites in these materials possess a high degree of ordering. Additionally, it is important to note that the peak positions and peak shapes do not significantly change, which indicates that crystalline morphology in respect to shape and distribution does not change through the thickness of the pipe. The pipes analyzed were uniform when considering the hoop and axial directions of the pipe. No measurable anisotropy exists in either SAXS or WAXD (Figure 17). This is indicated by the fact that the 2D intensity distribution is constant with respect to the angle when measuring SAXS through the thickness.

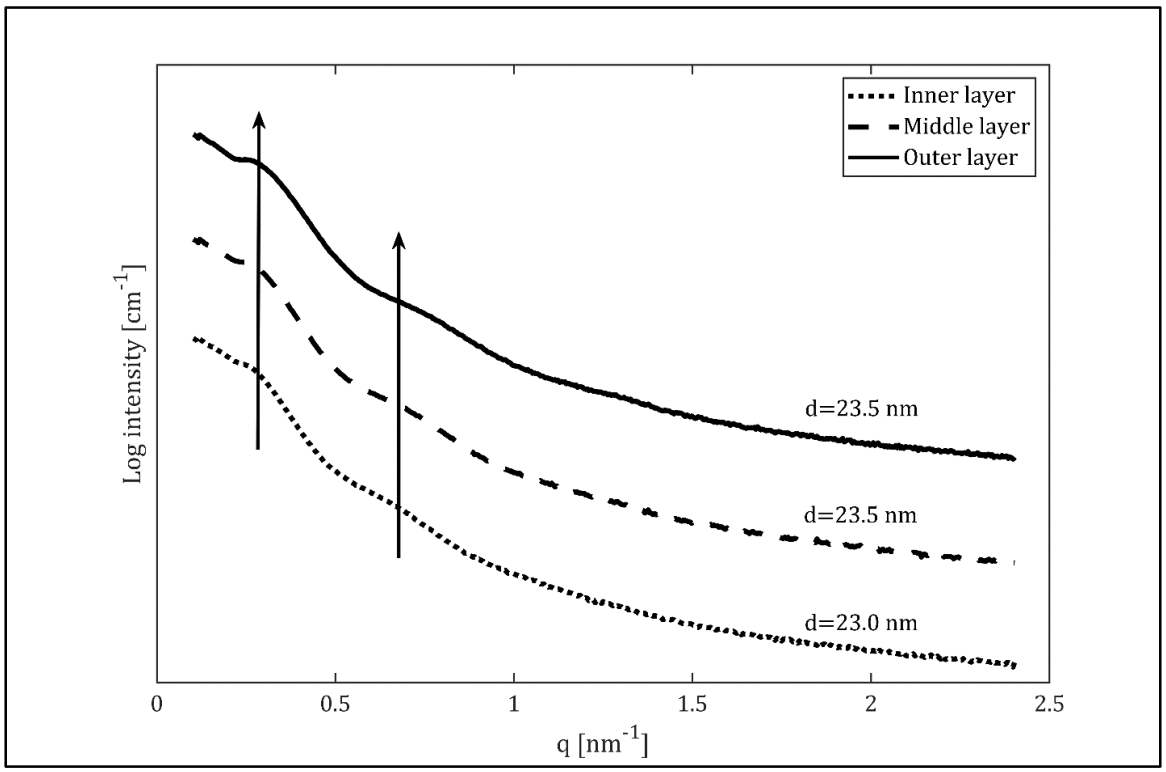

Figure 16: One dimensional small angle X-ray scattering profiles for different layers of the pipe, inner, middle and outer layers.

In order to compare the distribution of crystallites in the material through the thickness, three different layers have been cut from the pipes. The samples representing each layer was in a square shape with the side size 10 mm and thickness of 1 mm. When comparing inner, middle, and outer layers, Figure 17(b) demonstrates that the layers are nearly identical. The Bragg spacing (d) has been calculated as $d = \frac{2\pi}{q}$, and shows a slightly increasing long period from inside to outside. However, the increase in the Bragg spacing, *d*, is less than 3% of the total spacing. WAXD data was also taken on the same samples in order to compare the total crystallinity and investigate possible differences in the crystal structure. The total crystallinity can be computed as a ratio of the area of crystalline peaks and the total area under the curve. Similar to the SAXS data, Figure 17 shows that there are small differences in the layers; however, these differences in the total crystallinity are small compared to total crystallinity and the pipe can be considered homogeneous for the purposes of this accelerated testing method.

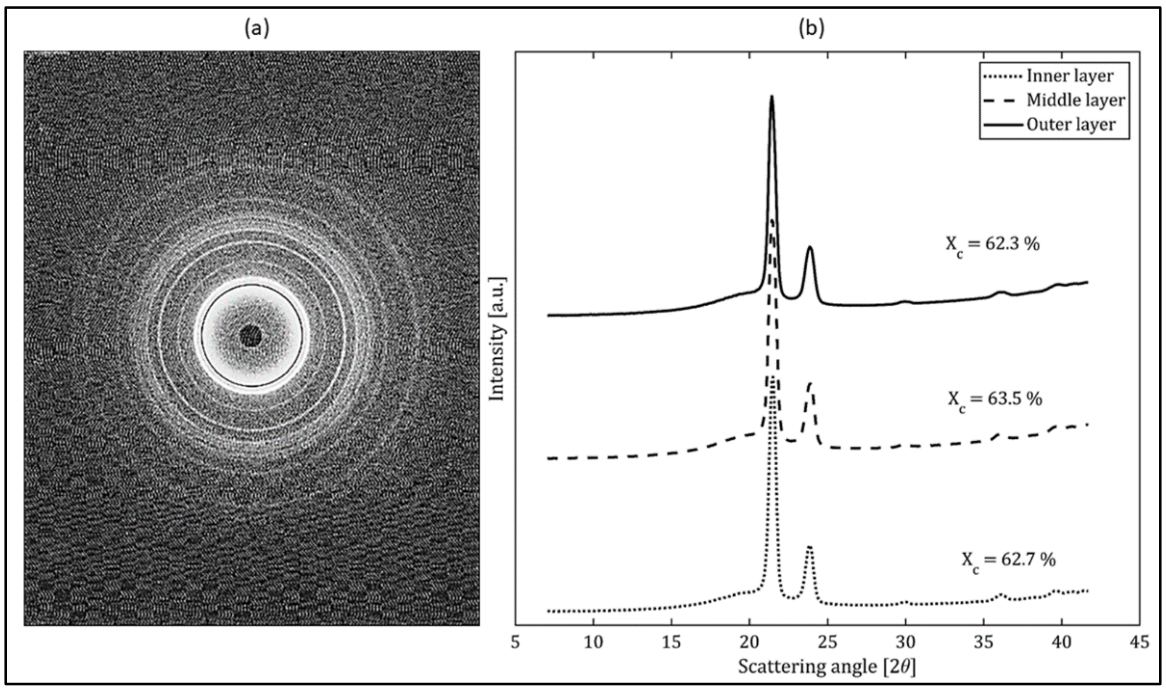

Figure 17: Wide angle X-ray scattering results. (a) two-dimensional results of the inner layer. (b) The WAXD profiles of different layers of the pipe.

2.7. Mechanical Testing Results and Discussion

In this study, HDPE pipe segments were employed to incorporate the processing conditions implicitly in the model. A comparison was made to highlight the difference between results obtained with the current approach and those obtained via traditional tensile tests. The traditional tensile tests were conducted in accordance with ASTM D638-14 [51]. The samples were prepared by compression molding of the HDPE into TYPE I dog-bone shape [51]. Figure 18 shows the tensile stress-strain results for SDR 11 HDPE pipes which were tested at 23 ℃. The results were compared with the traditional tensile test results conducted under the same testing configuration. The results highlight the importance of capturing the influence of processing conditions on the response of the as-processed pipes in contrast to the flat plaque samples. Such measurements are only feasible on pipe sections.

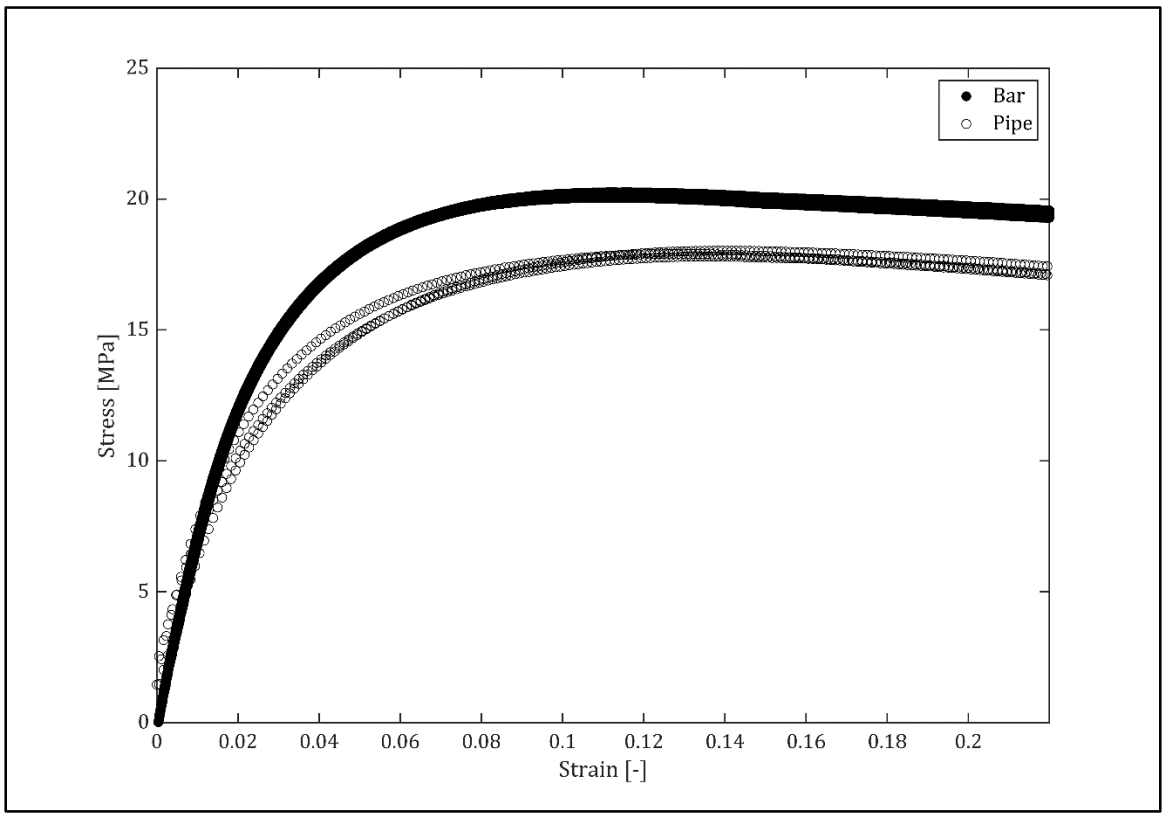

Figure 18: Tensile test results for HDPE dog-bone bars and the pipes at room temperature.

To determine the gage length for each custom designed test and to have a full strain field (as a result of necking), Digital Image Correlation (DIC) technique was used. Several uniaxial tensile tests were conducted to evaluate the yield stress in different strain rates and temperatures. The stress-strain results under different strain rates and at different temperatures are provided in Figure 19. As the results show, the tensile yield strength of the HDPE decreases either by increasing the temperature or decreasing the strain rate.

The yield stresses are evaluated where the first peak load was recorded. (These are shown with circles in Figure 19.) However, in some cases at temperatures of 60°C and 80°C and low strain rates, a second yield point can be identified which occurs at engineering strains of approximately 65 percent (shown with boxes in Figure 19). The same observation was reported previously by Seguela et al [20, 52] where the plastic deformation of different polyethylene and ethylene copolymers were studied and the temperature- and rate-dependence of the homogeneous and heterogeneous slips were taken into to account.

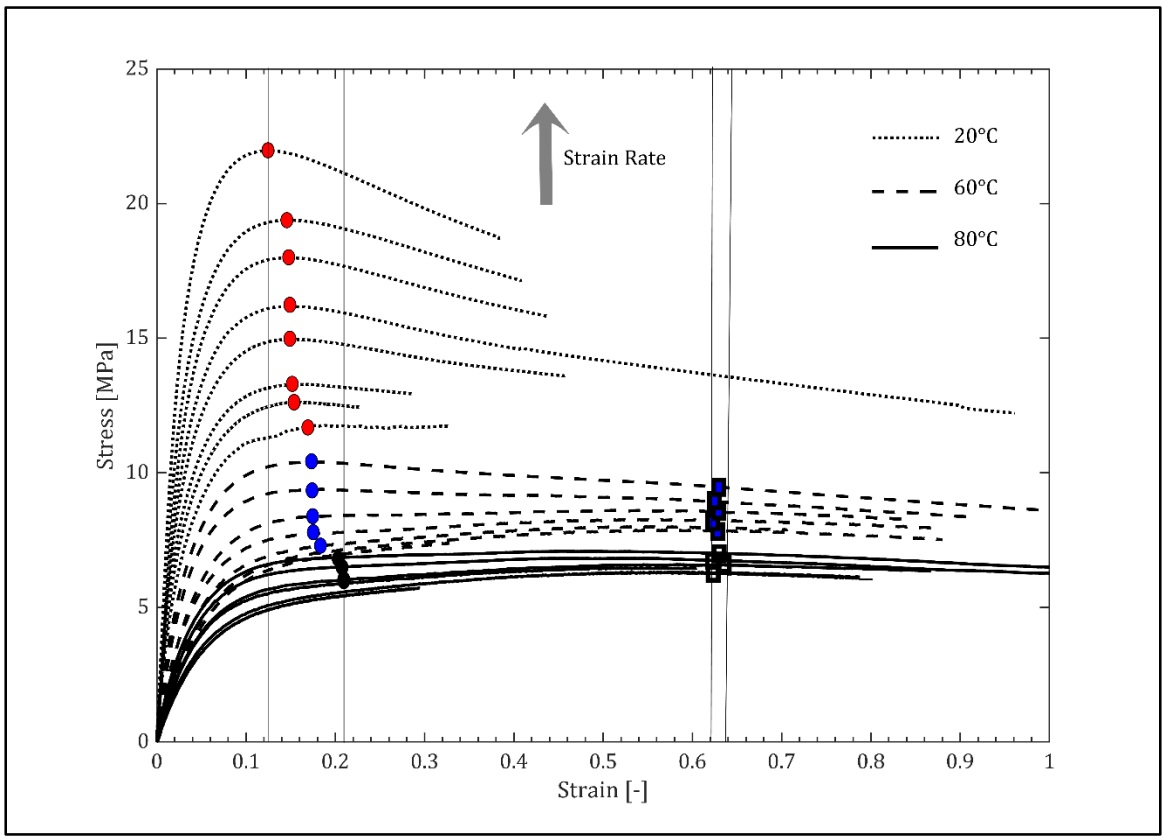

Figure 19: Tensile test results of the pipes at different strain rates and temperatures. The circles denote as the first yield and the boxes denote the second yield points.

In addition to the tensile tests, several compression tests were conducted at two temperatures and different strain rates. The stress-strain results under different strain rates and at the elevated temperature of 60°C are provided in Figure 20. To identify the yield point and to evaluate the yield stress, the bilinear representation method was employed [40, 53, 54] where the yield point is defined as the point of intersection of two tangent lines (shown in Figure 20).

After the testing, tensile yield strengths for each configuration and compressive yield strengths for different strain rates and temperatures were collected. Subsequently, the equivalent von Mises stress was calculated for both tensile and compression tests in which the unidirectional stress is the only non-zero component. The equivalent von Mises stress can be calculated by

$$\bar{\sigma} = \sqrt{\frac{1}{2}[(\sigma_a - \sigma_h)^2 + (\sigma_a - \sigma_t)^2 + (\sigma_t - \sigma_h)^2]} = \sigma_a \tag{7}$$

where σ_a, σ_h, and σ_t are axial, hoop and through thickness components of the stress tensor, respectively. The use of the von Mises equivalent stresses and strains is justified in this case

because the SAXS and WAXD results indicate no significant anisotropy in our as-processed pipes. For pipes with more significant anisotropy, a different analysis approach accounting for the anisotropy (e.g. [55]) should be employed. The equivalent von Mises strain is calculated as

$$\bar{\varepsilon} = \sqrt{\frac{2}{9}[(\varepsilon_a - \varepsilon_h)^2 + (\varepsilon_a - \varepsilon_t)^2 + (\varepsilon_t - \varepsilon_h)^2]} \tag{8}$$

where ε_a, ε_h, and ε_t are axial, hoop and through thickness components of the strain tensor, respectively. The deformations in the tests are relatively large and plastic. Thus, the material can be assumed to be incompressible and

$$\varepsilon_h = \varepsilon_t = -\frac{\varepsilon_a}{2} \tag{9}$$

By substituting (9) into equation (8), the equivalent von Mises strain for uniaxial tensile and compression tests can be calculated by

$$\bar{\varepsilon} = \sqrt{\frac{2}{9}[\left(\varepsilon_a + \frac{\varepsilon_a}{2}\right)^2 + \left(\varepsilon_a + \frac{\varepsilon_a}{2}\right)^2 + \left(\frac{\varepsilon_a}{2} - \frac{\varepsilon_a}{2}\right)^2]} = |\varepsilon_a| \tag{10}$$

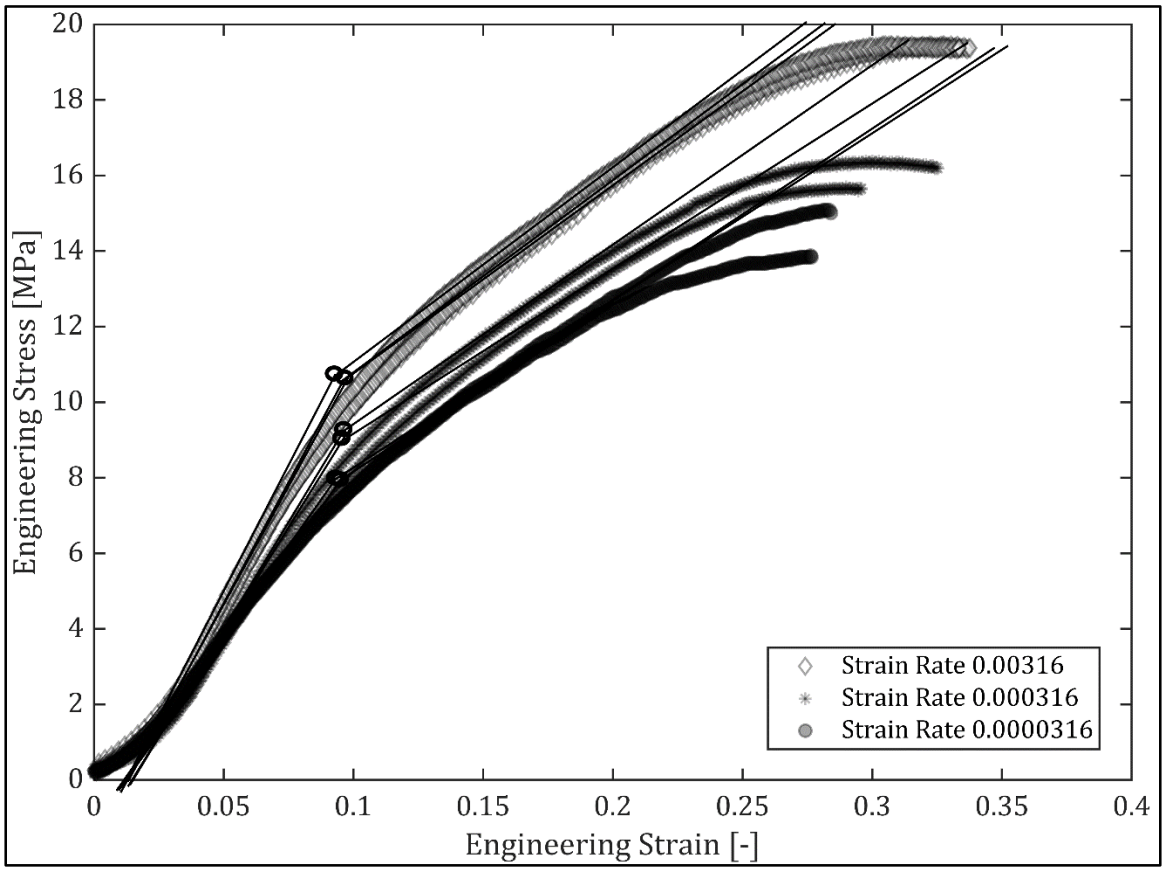

Figure 20: Compression test results at different strain rates and room temperature.

In addition to the equivalent von Mises stress and strain, hydrostatic pressure in each uniaxial test is calculated as

$$p = -\frac{1}{3}(\sigma_a + \sigma_h + \sigma_t) = -\frac{\sigma_a}{3} \tag{11}$$

The equivalent von Mises yield stresses, the equivalent von Mises strain rates, and the different applied temperatures were employed to fit the eight material constants in the pressure modified Eyring model, equation (6). To fit the model and evaluate the four unknown parameters for each Eyring process, the least squares regression technique was employed to minimize the square errors between the model prediction and these measured yield stresses. The regression was conducted in the Microsoft Excel solver using the generalized reduced gradient (GRG) nonlinear solving method with the convergence of 0.0001, forward derivatives and population size of 100. The fitting was conducted in two steps. In the first step, only the first Eying process (the first part of equation 6) was fitted to the yield data at high temperatures and low strain rates (the data points at the left side of the knee in figure 21). After the four unknown parameters of process 1 were evaluated, the remaining yield data were used to fit the whole model (equation 6) to evaluate the four unknown parameters associated with the second process. The R^2 value of 0.9961 was achieved at the end of the second step; the fitted parameters for the both Eyring process are presented in Table 1. The fitting processes were conducted multiple times using different initial guesses for the parameters and the same set of fitted parameters were found, providing confidence that a global minimum has been achieved. The values obtained for Ψ1 and Ψ2 indicate that the effect of hydrostatic pressure is different for each process. Figure 21 summarizes the measured tensile and compression yield stresses along with the fitted model.

The Eyring parameters listed in Table 1 and the comparison between the model and experimental data in Figure 21 suggests that two Eyring processes can adequately describe the yield behavior of the material. Process 1 has an activation energy of 902.5 kJ/mol (1.498×10^{-18} Joules) and is observed in low strain rates and high temperatures. On the other hand, Process 2 has a lower activation energy of 108 kJ/mol (1.793×10^{-19} Joules) and appears at higher strain rates and lower temperatures.

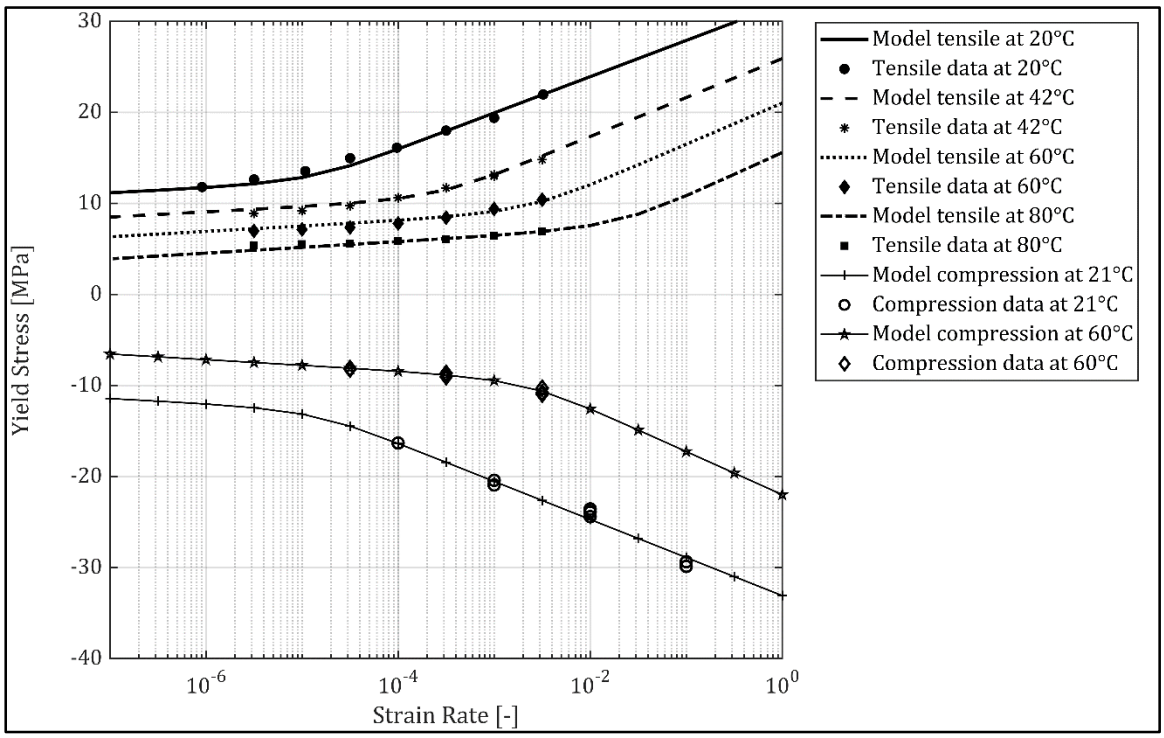

Figure 21: Yield stress data from tensile and compression tests, and the perdition lines constructed based on developed Eyring model.

Table 1: Evaluated model parameters based on yield data in figure 21.

i	$V_i\ (nm^3)$	$\Delta E_i\ (\frac{kJ}{mol})$	$\dot{\varepsilon}_i\ (\frac{1}{s})$	$\Psi_i\ (nm^3)$
1	34.58	902.5	5.61E+111	3.644
2	2.66	108	1.716E+14	0.0048

After the tensile and compression tests, biaxial creep tests in the form of hydrostatic internal pressure testing of the pipes at room temperature and under different stress levels were conducted to evaluate the critical strain for equation (1) and to verify the time-to-failure which is estimated by the model. The hoop and axial strains were measured using DIC. The through-thickness-strain was evaluated using the incompressibility assumption. Then, the equivalent von Mises strains were calculated using equation (10).

The critical strain was evaluated using only short-term biaxial creep test data (those tests in which failure occurred in less than a day). The slope of the von Mises strain in the secondary creep

region was calculated for each test. The critical strain was evaluated as the product of the experimental time-to-failure and the secondary strain rate. Figure 22 summarizes the secondary strain rates versus time-to-failure for biaxial creep tests. The exponent on the time-to-failure is constrained to a value of -1; the value of 0.971 for R^2 indicates that the critical strain of 0.1331 is independent of strain rate (and hence independent of the stress).

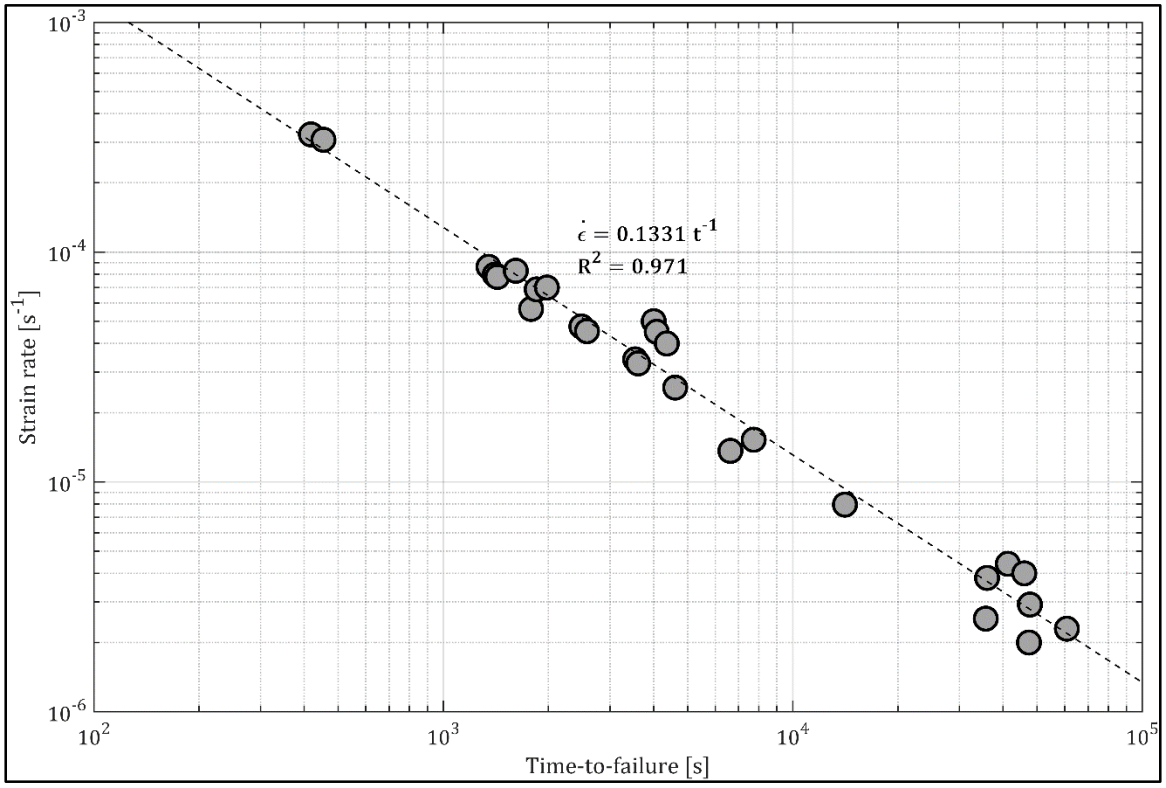

Figure 22: Evaluation of critical strain.

The time-to-failure can be predicted by substituting the plastic strain rates, evaluated from the model, and critical strain into equation (1). One potential concern in this approach is its reliance on critical strains obtained from the internal pressurization test. A potential alternative is to evaluate the critical strain as the strain at the first yield point observed in the uniaxial tests (the circles in Figure 19). To evaluate the sensitivity of the predictions to the critical strain, lifetime predictions using critical strain values of 0.123, 0.1331, and 0.210 are calculated employing the developed Eyring-type model (The first and last values are the minimum and maximum yield strains observed in the uniaxial tensile tests; the middle value is that obtained from the internal

pressurization tests.). The model predictions and the experimental results from the biaxial creep tests at room temperature are summarized in Figure 23 (a). This figure provides the hoop stress versus the time-to-failure for all biaxial creep data showing that there is a good agreement between the actual and the predicted time-to-failure data. We note that using different values of the critical strain naturally results in different predictions. However, in the low-pressure regions, the differences in hoop stress at a given lifetime are very small (less than 1.7%).

To investigate the origin of this apparent insensitivity of the time-to-failure to the value of the critical strain, we re-examine the time-to-failure expression in equation (1). We note that the value of ε_{cr} is in the order of 10^{-1} while the plastic strain rate, $\dot{\varepsilon}_p$, ranges from values on the order of 10^{-6} to 10^{-10} for long-term biaxial creep tests. A natural consequence is that the predicted time-to-failure is much more sensitive to the plastic strain rate than to the value of the critical strain, especially at very small creep rates. Consequently, based on this result and the observations in Figure 23 (a), one can conclude that the predicted long-term performance of the pipes is independent of the critical strain. Therefore, the lifetime predictions can be done without conducting any creep tests, only tensile and compression tests at different strain rates and temperatures are sufficient to develop the model (including the estimate of ε_{cr} based on the quasi-static tests) and predict the long-term performance of the pipes. Each of the necessary model calibration tests are conducted on a single INSTRON® load frame in under 10 days, resulting in a significant improvement in the required testing time to develop the prediction. Naturally, we anticipate that the biaxial tests to failure would still be conducted in limited cases to validate the model. However, initial material screening/down selection studies may be conducted rapidly using the approach outlined here.

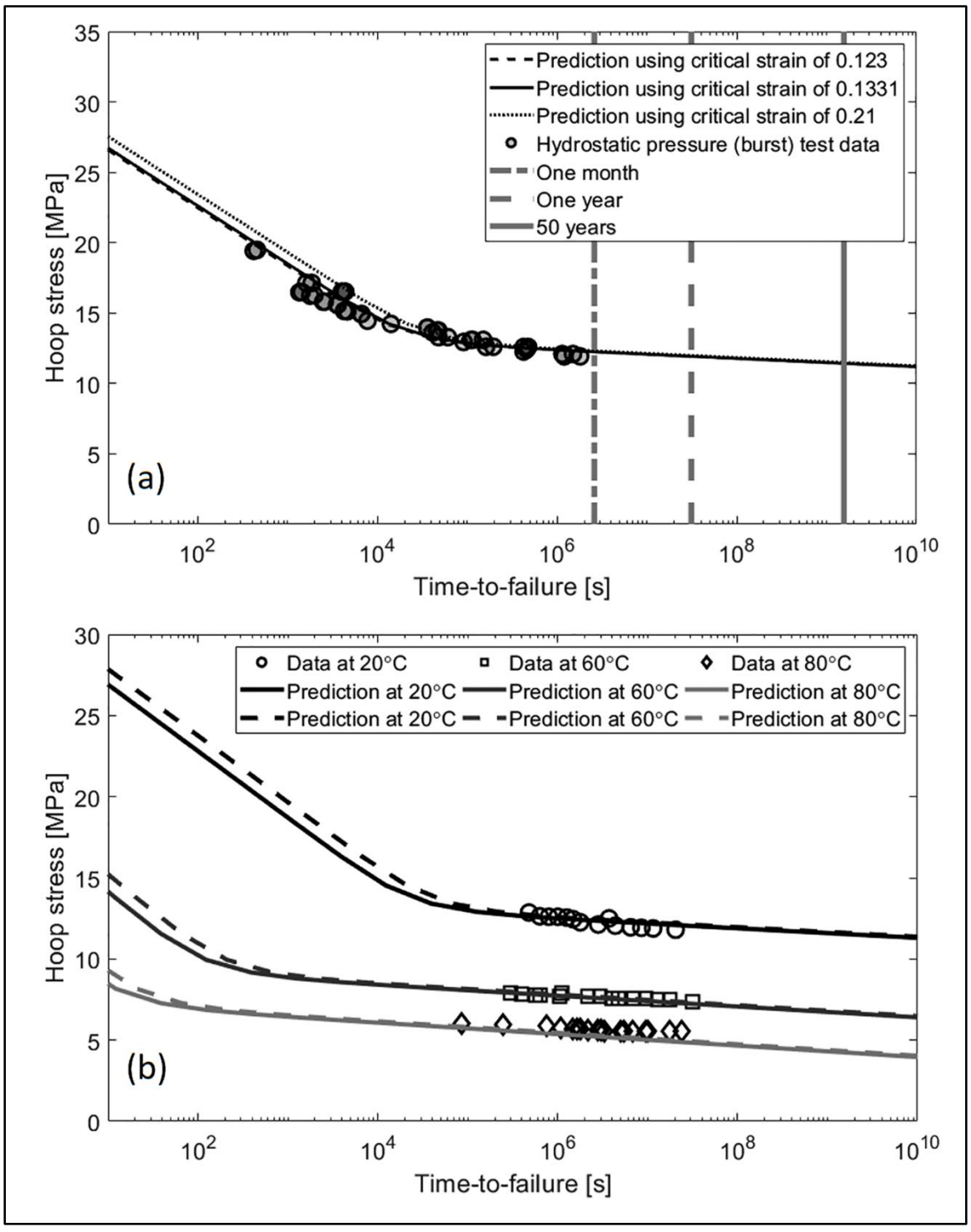

Figure 23: Model validation. (a) Hydrostatic pressure (burst) test data at room temperature, measured using the experimental setup shown in figure 14. (a) long-term hydrostatic pressure test data for a PE100 pipe grade [2].

In addition, the model predictions at three temperatures of 20°C, 60°C and 80°C are shown in figure 23 (b) where three sets of long-term hydrostatic pressure (burst) test data are provided. The experimental data were reported [2] for slightly different HDPE pipes. The pipes, however, are listed as PE100 pipe grade and are expected to have the same long-term performance as the pipes used in the current study at the working temperature of 20°C. As shown in figure 23 (b), the model predictions are in a good agreement with the experimental data at 20°C and 60°C. However, at 80°C, the model prediction underestimates the performance of the pipe. This observation might be related to the differences in the melting points of the pipe materials. The pipes used in the current study has a lower melting point, thus, the performance of the pipe might not be the same at higher temperatures.

Of particular interest for pipe designs is the value of yield stress at low strain rates. In the case of low strain rates, the behavior associated with Process 1 is dominant. Thus, from equation (6) we have

$$\frac{S_y}{T} = \frac{k}{V_1}\sinh^{-1}\left(\frac{\dot{\varepsilon}}{\dot{\varepsilon}_{0_1}}\exp\left(\frac{\Delta E_1}{kT}+\frac{p\Psi_1}{kT}\right)\right) \tag{12}$$

The inverse hyperbolic sine function is given exactly [56] by

$$\sinh^{-1}(z) = \ln(z+\sqrt{z^2+1}) \tag{13}$$

For the form given in equation (12),

$$z = \frac{\dot{\varepsilon}}{\dot{\varepsilon}_{0_1}}\exp\left(\frac{\Delta E_1}{kT}+\frac{p\Psi_1}{kT}\right) \tag{14}$$

At low strain rates and at room temperature, the value of z is very large, thus equation (13) can be simplified as

$$\sinh^{-1}(z) \approx \ln(2z) \tag{15}$$

Now, by using equations (14) and (15), equation (12) can be rearranged as

$$\frac{S_y}{T} \approx \frac{k}{V_1}\left[\ln\left(2\frac{\dot{\varepsilon}}{\dot{\varepsilon}_{0_1}}\right)\right]+\frac{\Delta E_1}{TV_1}+\frac{p\Psi_1}{TV_1} \tag{16}$$

For an internally pressurized thin-walled pipe, the von Mises yield stress can be related to the hydrostatic pressure as

$$p = -\frac{3}{\sqrt{3}}S_y \tag{17}$$

Thus, the von Mises yield stress can be evaluated as

$$S_y \approx \frac{Tk\left[\ln\left(2\frac{\dot{\varepsilon}}{\dot{\varepsilon}_{0_1}}\right)\right]+\Delta E_1}{V_1+\frac{\sqrt{3}}{3}\Psi_1} \tag{18}$$

For a 50 year (~1.58×10^9 second) lifetime of the pipe and assuming a critical strain of ~0.1, a plastic strain rate of ~10^{-10}/s leads to ductile creep rupture. Using the material parameters from Table 1, a plastic strain rate of ~10^{-10}/s and room temperature (20°C), the von Mises stress, S_y, of 10.0 MPa can be calculated based on equation (18). This corresponds to a hoop stress of 11. 6 MPa for a thin-walled pipe under an internal pressure.

Although the approach presented here was developed and validated using HDPE pipe segments, it can be applied to other plastic pipes. Previous studies showed that the Eyring model can successfully describe the yield kinetics of different polymers. For example, Roetling [45-47] successfully applied the Eyring equation to the yield behavior of polymethylmethacrylate and isotactic polypropylene. Bauwens et al. [38, 42, 44, 49] modeled the yielding behavior of poly (vinyl chloride) and polycarbonate using the Eyring equation. Thus one can perform the testing protocol and data reduction approach suggested herein to other polymeric pipes.

1.8. Conclusions

A new accelerated testing protocol was presented where the mechanical characterizations were conducted on as manufactured pipe segments. Several tensile and compression tests were conducted at different rates of deformation and temperatures on the pipe segments. Using as-manufactured pipe segments eliminates any additional adjustments in the material state and enhances the ability to study the effect of different processing conditions on the behavior of the material. The yield kinetics were described using two pressure-modified Eyring processes working in parallel. Effect of hydrostatic pressure on the material plastic flow rates was evaluated separately for each of the Eyring processes. The results indicated that the hydrostatic pressure affected the plastic flow of the material differently for each process and, thus, independent pressure modification factors were required to characterize the effect of hydrostatic pressure on each Eyring process. To conduct the validation tests, a custom-designed test setting was designed and assembled using a data acquisition system, pressure transducers, and actuators. The experimental setting was used to conduct hydrostatic pressure (burst) tests on the SDR 11 pipe segments under several carefully controlled constant pressures and at the room temperature. During each test, the

field of deformation of each sample was measured using a high-resolution digital image correlation (DIC) system.

The constructed Eyring model was utilized to predict the long-term performance of the pipes. During evaluating the predictions, several critical strain values were adopted to investigate the sensitivity of the model to the magnitude of the critical strain. The results indicated that the magnitude of critical strain did not play a significant role in the long-term predictions, which means the predictions were mainly dominated by the estimated value for the plastic rate of deformation. Thus, the yield strain measured during the tensile tests was used instead of critical strain. This important observation yielded to eliminate the need for conducting characterization creep tests. Consequently, the new experimental protocol significantly reduced the required testing time to 10 days using the experimental data from only tensile and compression tests conducted using a single load frame. The developed model was able to provide an accurate lifetime prediction, as demonstrated with the comparison of the results of experimental measurements.

Chapter 3: Mechanical Characterization and Numerical Modeling of High-Density Polyethylene Pipes

3.1. Introduction

The worldwide plastic pipe industry is predicted to experience dramatic growth over the next decade. Because of its low-cost production, and excellent long-term performance of high-density polyethylene (HDPE), this polymer is among the most popular materials used in the production of plastic pipes. However, due to its complicated semicrystalline microstructure and nonlinear time-temperature dependent mechanical behavior, the mechanical characterization of HDPE pipes is very challenging and time-consuming. In addition, during the manufacturing of HDPE pipes, the processing conditions (such as molecular orientation, cooling rate, and extrusion injection pressure) can introduce different complex microstructures into the material which lead to different material properties. In this chapter, a new numerical model is developed based on the mechanical characterization technique presented in the previous chapter. The model provides a powerful tool to investigate the behavior of the products over a wide range of service times and different working conditions. The mechanical characterization to support the model was performed on as-manufactured pipe segments to practically enhance the ability of direct study of the different processing condition. The results from the numerical modeling were compared with the experimental data for tensile and internal pressurization (burst) test cases and a good agreement was observed.

3.2. Methods

The general response of HDPE to a large deformation can be divided into two main components: the initial elastic component and the time and temperature dependent non-elastic component. HDPE is a semi-crystalline polymer with a complex viscoelastic and plastic behavior. One can combine the time and temperature dependent elastic and plastic responses of the material to develop a comprehensive constitutive model which is able to describe the mechanical behavior of the material under different temperature, loadings, and deformation rates.

Several research studies focused on the viscoelastic behavior of polyethylene [57-60]. Colak and Dusunceli [58] studied the viscoelastic and viscoplastic behavior of HDPE by developing a viscoelasticity-theory-based model. The model was then used to simulate the material under uniaxial compression loading at different rates of deformation. Although the model predictions were in great agreement with the experimental data, the model development process was based on fitting an arbitrary function on the experimental data using the trial-and-error procedure.

In another study, Guedes [57] developed a mathematical model for the viscoelastic behavior of a medical grade polyethylene based on the fractional Maxwell model where the applicability of the time and temperature superposition was investigated. Both horizontal and vertical shifts were found to be required to superpose the curves. Later, Bilgin et al. [60] studied the viscoelastic behavior of polyethylene pipes by conducting several stress-relaxation tests to evaluate the time-dependent behavior of the material under different mechanical and thermal loading levels. The results showed the thermal stresses within the pipe are significantly lower than the design stresses. In addition, they found that by employing the linear viscoelastic characterization, one can predict the pipes' short-term responses to the designed range of stress. However, the time-dependent plastic behavior and long-term responses of PE pipes still need to be investigated. In the current study, we assume that the time and temperature dependent plastic behavior of the material has the most dominant effect on the long-term performance of the pipes and initial responses can be modeled simply by defining the elastic behavior. However, to validate this assumption, the sensitivity of the long-term performance to the initial viscoelastic responses is measured and discussed.

The hydrostatic pressure modified Eyring model was employed to characterize the complicated plastic response of the material. The plastic deformation of the material is highly sensitive to the

working temperature and the loading level. Eyring [39] suggested a generalized expression to relate the viscosity to the rate of shear deformation and the temperature. Then, several other scientists in different research studies [42, 44, 49] adopted and modified the expression to evaluate the stress and temperature dependence of the plastic flow rate, $\dot{\varepsilon}$, as:

$$\dot{\varepsilon} = \dot{\varepsilon}_0 \exp(-\Delta E/kT) \sinh\left(\frac{S_y V}{kT}\right) \tag{3.1}$$

where S_y is yield stress, $\dot{\varepsilon}_0$ is a constant, T is absolute temperature, and k is the Boltzmann's constant. In equation (3.1), ΔE is the required energy to activate the plastic flow, activation energy. The polymer is permitted to flow when several number of polymer chain segments have the sufficient energy move [61]. The volume of the polymer segments required to initiate the movement is called activation volume [62] and denoted by V. Different research studies [42, 45-47] on yield behavior of polymer materials over a wide range of deformation rates and temperatures indicated that more than one plastic flow process exists, and thus, multiple Eyring processes can be employed in parallel to describe the yielding behavior of the material in a wide range of deformation rate and temperate. The overall yield stress, however, can be calculated by adding the yield stress evaluated based on each Eyring process or:

$$\frac{S_y}{T} = \frac{S_{y_1}}{T} + \frac{S_{y_2}}{T} = \frac{k}{V_1}\sinh^{-1}\left(\frac{\dot{\varepsilon}}{\dot{\varepsilon}_{0_1}}\exp\left(\frac{\Delta E_1}{kT}\right)\right) + \frac{k}{V_2}\sinh^{-1}\left(\frac{\dot{\varepsilon}}{\dot{\varepsilon}_{0_2}}\exp\left(\frac{\Delta E_2}{kT}\right)\right). \tag{3.2}$$

In equation (3.2), the subscripts 1 and 2 are associated with each of the Eyring plastic flow processes. Studies on uniaxial tensile and compression tests of polymers under the same deformation rates [38, 41, 48] indicated a significant difference in the magnitude of yield stress which is considered as the effect hydrostatic pressure effect on yield stress. The hydrostatic pressure increases the activation energy of each Eyring processes. Therefore, the hydrostatic pressure modified form of equation (3.2) is [41, 63];

$$\frac{S_y}{T} = \frac{k}{V_1}\sinh^{-1}\left(\frac{\dot{\varepsilon}}{\dot{\varepsilon}_{0_1}}\exp\left(\frac{\Delta E_1}{kT} + \frac{p\Psi_1}{kT}\right)\right) + \frac{k}{V_2}\sinh^{-1}\left(\frac{\dot{\varepsilon}}{\dot{\varepsilon}_{0_2}}\exp\left(\frac{\Delta E_2}{kT} + \frac{p\Psi_2}{kT}\right)\right) \tag{3.3}$$

where p is the hydrostatic pressure and Ψ_1 and Ψ_2 are pressure activation volume for Processes 1 and 2, respectively. It is noteworthy that the hydrostatic pressure term, p, is the pressure within the

material and must be distinguished from the pressure inside the pipe during the burst tests. For uniaxial tensile and compression loading, p is given as $-\frac{\sigma}{3}$ and $\frac{\sigma}{3}$, respectively, where σ is the absolute value of axial stress. The hydrostatic pressure can be evaluated as $-\frac{\sigma_h}{2}$ when the pipe is under internal pressure loading where σ_h denote as the hoop stress of a thin-walled pipe. In equation (3.3), there are eight parameters that need to be determined experimentally.

3.3. Experiments

Several characterization tests were required to provide sufficient data to develop the model. The characterization tests were conducted in the form of uniaxial tensile and compression tests at different temperatures and strain rates. Then the yield stress associated with each test configuration were collected and utilized to evaluate the unknown parameters of equation (3) and develop hydrostatic pressure modified plastic flow rate model. Since pressure activation volumes, Ψ_1 and Ψ_2, are independent parameters, at least two sets of uniaxial compression tests in two different temperatures are required. The compression tests were conducted at room temperature and at $60℃$ to ensure an adequate number of experimental data points are available for each of the two Eyring flow processes shown in figure 24. After the characterization tests were completed, the model was fitted on the test data using a two-step regression process. In the first step, only Eyring process 1 was fitted to the test data shown with the red mask in figure 24. Then, by fixing the corresponding parameters of Eyring process 1, the whole model (including Eyring process 1 and 2) was fitted to the rest of the test data. The reason for using such a dual steps regression process was to ensure that the model captures the most accurate flow behavior of the material at higher temperatures and lower strain rate configuration. Such temperature and strain rate configurations are, indeed, related to the long-term creep behavior of the material. Table 2 presents the model parameters (evaluated by applying the dual steps regression process) and elastic properties (measured using the tensile tests data at different temperatures). The characterization test data, the model prediction, and the relative errors are provided in Table 3.

Table 2: The model parameters and elastic properties.

i	$V_i\ (nm^3)$	$\Delta E_i\ (\frac{kJ}{mol})$	$\dot{\varepsilon}_i\ (\frac{1}{s})$	$\Psi_i\ (nm^3)$
1	34.58	902.5	5.61E+111	3.644
2	2.66	108	1.716E+14	0.0048

Temperature $(°C)$	20	42	60	80
E (MPa)	500	300	150	120
ν	0.49			

To observe the creep rupture behavior and measure the short/long term performance of the HDPE pipes, several validation tests were conducted using an in-house built internal pressurization test setup. (The schematic diagram of the setup is shown in figure 14.) The pipes were cut into 254 mm sections, speckled with white paint, and placed between end caps. Then, water was pumped into the sample and reservoir to purge out the air from the system. Finally, all the valves were closed and compressed nitrogen (N_2) gas was charged into the reservoir. To maintain a constant pressure, a feedback pressure control system was designed and created. The control system measured the internal pressure in the sample using an pressure transducer analyzed the data, and then sent appropriate command signals to the actuator valves to adjust the system pressure. A digital image correlation (DIC) system was utilized to measure the strains in axial and hoop directions of the pipe samples. The imaging rate was adjusted based on the estimated time scale of each test. Each test was repeated at least two times to make ensure that the experimental results are repeatable.

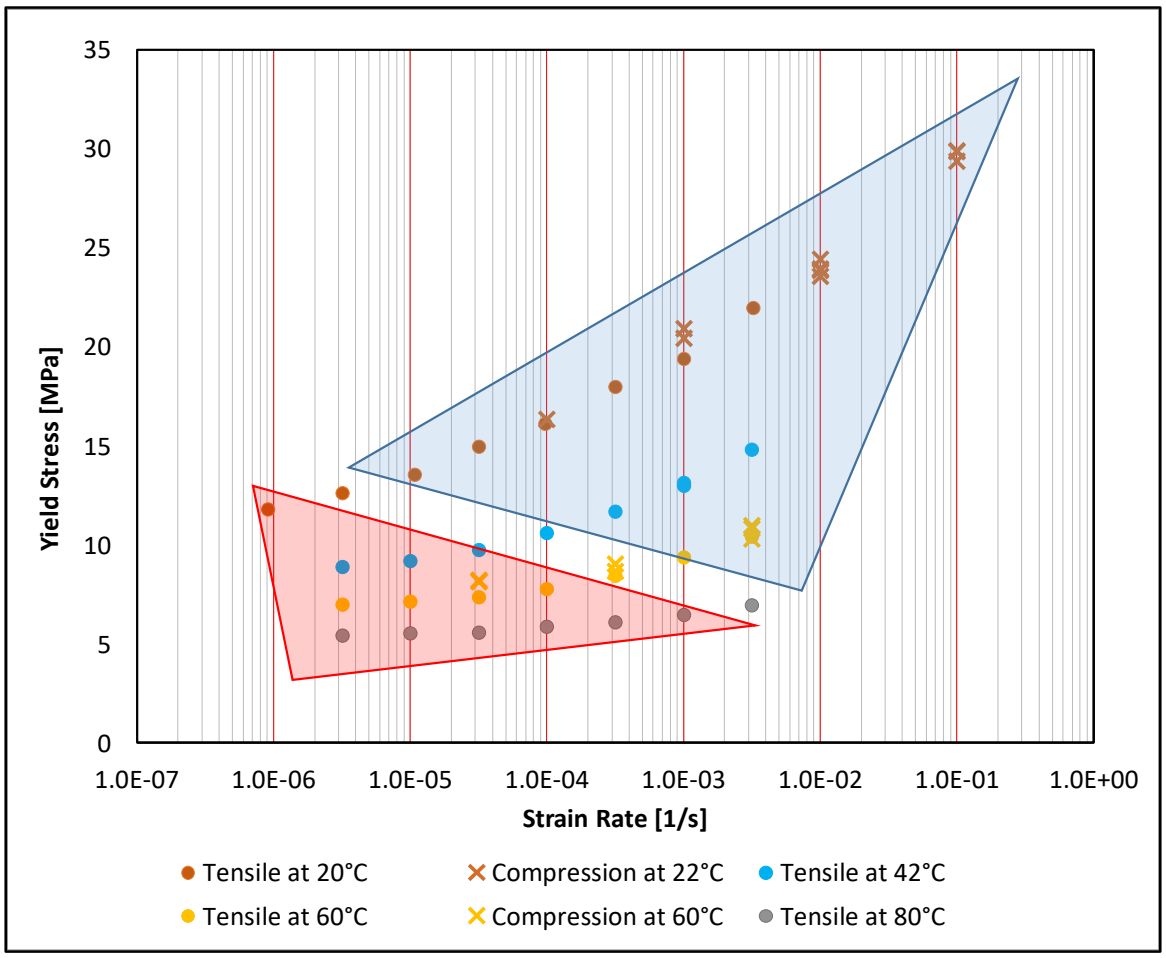

Figure 24: Yield stress from the characterization tests at different temperatures and strain rates. The area identified with the red mask is associated with Eyring process 1, however, the blue mask denotes the area where both Eyring processes are active.

Table 3: Characterization test data and model predictions.

Test type	Temperature [℃]	Strain Rate [s^{-1}]	Yield Stress [MPa]	Model prediction yield stress [MPa]	Relative Error [%]
Tensile	20	9.08E-07	11.794	11.397	3.42
		3.16E-06	12.628	11.805	6.74
		1.08E-05	13.541	12.775	5.82
		3.16E-05	14.964	14.220	5.10
		9.71E-05	16.121	15.983	0.86
		3.16E-04	17.992	17.856	0.76
		1.00E-03	19.384	19.703	1.63
		3.24E-03	21.968	21.547	1.93
	42	3.16E-06	8.890	9.182	3.24
		1.00E-05	9.187	9.363	1.90
		3.16E-05	9.749	9.633	1.19
		1.00E-04	10.608	10.193	3.99
		3.16E-04	11.693	11.416	2.40
		1.00E-03	12.982	13.231	1.90
		1.00E-03	13.127	13.225	0.74
		3.16E-03	14.811	15.183	2.48
	60	3.16E-06	6.973	7.295	4.52
		1.00E-05	7.138	7.448	4.25
		3.16E-05	7.353	7.611	3.45
		1.00E-04	7.783	7.803	0.27
		3.16E-04	8.427	8.106	3.88
		1.00E-03	9.389	8.748	7.06
		3.16E-03	10.397	10.128	2.63
	80	3.16E-06	5.420	5.196	4.21
		1.00E-05	5.519	5.356	3.00
		3.16E-05	5.585	5.518	1.20
		1.00E-04	5.882	5.676	3.56
		3.16E-04	6.081	5.853	3.82
		1.00E-03	6.477	6.067	6.54
		3.16E-03	6.940	6.422	7.75
Compression	22	1.00E-04	-16.332	-16.590	1.57
		1.00E-03	-20.426	-20.552	0.62
		1.00E-03	-20.940	-20.570	1.78
		1.00E-02	-23.570	-24.488	3.82
		1.00E-02	-23.852	-24.498	2.67
		1.00E-02	-23.927	-24.501	2.37
		1.00E-02	-24.418	-24.519	0.41
		1.00E-01	-29.863	-28.539	4.53
		1.00E-01	-29.889	-28.540	4.62
		1.00E-01	-29.366	-28.521	2.92
	60	3.16E-03	-10.295	-10.888	5.60
		3.16E-03	-10.813	-10.907	0.87
		3.16E-03	-10.974	-10.913	0.56
		3.16E-04	-8.655	-8.733	0.90
		3.16E-04	-9.042	-8.747	3.31
		3.16E-05	-8.210	-8.182	0.34
		3.16E-05	-8.141	-8.180	0.48

3.4. Numerical Modeling

Finite element analysis (FEA) was adopted to conduct the simulation of the nonlinear behavior of HDPE pipes under different loading conditions. This modeling was conducted using a commercial FEA software, Abaqus CAE version 6.14. However, due to the complicated nonlinear plastic behavior of the material, a user-material subroutine file was developed in Fortran. The pipe was modeled using axisymmetric shell elements with four degrees of freedom (DOF) including two displacement DOF in the radial and axial directions and two rotation DOF about the z-axis and in the r-z plane. As with the continuum axisymmetric bending formulation, the restriction is made that a plane of symmetry exists in the r–z plane at $\theta = 0$. Hence in-plane bending of the model is permitted, while deformations such as torsion about the axis of symmetry are precluded. The symmetries of the undeformed configuration and of the deformation are utilized through the assumption of particular displacement and rotation interpolations around the circumference of the shell. Specifically, Fourier series expansions are used in the θ or circumferential direction that preserve the plane of symmetry. The pipe was modeled with the actual dimensions of the SDR 11 pipes with 33 mm diameter and the wall thickness of 3 mm. The end caps also were modeled as a rigid axisymmetric part tied to each end of the pipe. Due to the symmetry, only half of the pipe and one end cap is modeled and appropriate symmetry boundary conditions were enforced. Figure 25 shows the axisymmetric model of pipe mounted on the end cap.

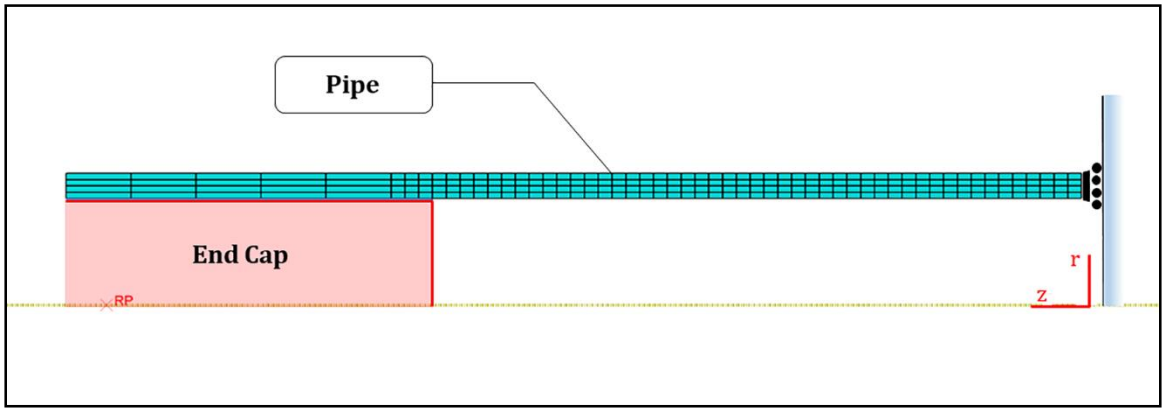

Figure 25: Axisymmetric model of the pipe.

In order to use the developed plastic flow model in the simulation, a user creep subroutine file was developed in Fortran. The subroutine was called at all of the integration points of elements for

which the material definition contains user-subroutine defined creep behavior, during procedures that allow viscoplastic response to occur. The subroutine is intended to provide the creep laws that are to be included in the time/temperature dependent viscoplastic model. For our material, the creep law (viscoplastic behavior) of the following form can be defined:

$$\dot{\bar{\varepsilon}} = g^{cr}(Q, P, T) \tag{3.4}$$

where g^{cr} is a nonlinear creep law based on equation 3.3 that relates the equivalent creep (plastic) strain rate to the applied temperature, T, equivalent Mises stress, Q, and hydrostatic pressure, P. However, because of the nonlinear nature of hyperbolic sine inverse funtions at equation 3.3, determination of a mathematical expression for the creep law, g^{cr}, that explicitly relates the creep strain rate to the other terms is very challenging.

A numerical analysis was adopted to overcome the above-mentioned challenge and evaluate the incremental creep strain rate numerically based on the field variables. In this numerical analysis, Newton-Raphson method was used in a "while loop" to evaluate the strain rate with a high level of accuracy. To use the Newton-Raphson method, the subroutine needs to start the analysis using an initial guess for the strain rate value. The initial guess is calculated as

$$\dot{\bar{\varepsilon}}_0 = \frac{Q}{kT\left\{\frac{1}{V_1\dot{\varepsilon}_{0_1}}\exp\left(\frac{\Delta E_1}{kT}+\frac{P\Psi_1}{kT}\right)+\frac{1}{V_2\dot{\varepsilon}_{0_2}}\exp\left(\frac{\Delta E_2}{kT}+\frac{P\Psi_2}{kT}\right)\right\}} \tag{3.5}$$

which is based on rearranging the equation (3.3). The inverse hyperbolic sine functions were approximated by a linear function: $\sinh^{-1} x \cong x$. The subroutine then starts a "while loop" where the value of function $f(\dot{\bar{\varepsilon}}_0)$ was calculated as

$$f\left(\dot{\bar{\varepsilon}}_0\right) = S_{y_0} - Q$$

where S_{y_n} is the equivalent Mises stress calculated using equation (3.3) based on the model constants, the strain rate initial guess, the given temperature, and the given hydrostatic pressure. Then, the $f'(\dot{\bar{\varepsilon}})$ was defined at $\dot{\bar{\varepsilon}} = \dot{\bar{\varepsilon}}_0$ as;

$$f'(\dot{\bar{\varepsilon}}) = \frac{\partial f(\dot{\bar{\varepsilon}})}{\partial \dot{\bar{\varepsilon}}} = kT \left\{ \frac{\exp\left(\frac{\Delta E_1}{kT} + \frac{P\Psi_1}{kT}\right)}{V_1 \sqrt{\left(\dot{\bar{\varepsilon}} \exp\left(\frac{\Delta E_1}{kT} + \frac{P\Psi_1}{kT}\right)\right)^2 + 1}} + \frac{\exp\left(\frac{\Delta E_2}{kT} + \frac{P\Psi_2}{kT}\right)}{V_2 \sqrt{\left(\dot{\bar{\varepsilon}} \exp\left(\frac{\Delta E_2}{kT} + \frac{P\Psi_2}{kT}\right)\right)^2 + 1}} \right\} \quad (3.6)$$

After calculating $f(\dot{\bar{\varepsilon}}_0)$ and $f'(\dot{\bar{\varepsilon}}_0)$, the subroutine evaluated the new estimate for the incremental creep strain rate as

$$\dot{\bar{\varepsilon}}_1 = \dot{\bar{\varepsilon}}_0 - \frac{f(\dot{\bar{\varepsilon}}_0)}{f'(\dot{\bar{\varepsilon}}_0)} \quad (3.7)$$

The process was repeated in the loop as

$$\dot{\bar{\varepsilon}}_{n+1} = \dot{\bar{\varepsilon}}_n - \frac{f(\dot{\bar{\varepsilon}}_n)}{f'(\dot{\bar{\varepsilon}}_n)} \quad (3.8)$$

until a sufficient accuracy was achieved and the adjustment was 4 orders of magnitude smaller than the most recent estimated strain rate, or

$$\log(\dot{\bar{\varepsilon}}_n) - \log\left(Abs\left(\frac{f(\dot{\bar{\varepsilon}}_n)}{f'(\dot{\bar{\varepsilon}}_n)}\right)\right) > 4.0 \quad (3.9)$$

The user subroutine must define the increment of inelastic strain, $\Delta\bar{\varepsilon}$, as a function of Q, P, T and of the time increment, Δt. The increment of inelastic strain can be calculated as

$$\Delta\bar{\varepsilon} = \dot{\bar{\varepsilon}}_n \Delta t \quad (3.10)$$

At the start of a new increment, the subroutine was called once for each integration point to calculate the estimated creep strain based on the state at the start of the increment. Subsequently, it was called twice for each iteration: once to calculate the creep strain increment at the start of the increment and once to calculate it at the end of the increment. This was needed to test the validity of the time increment with respect to the user-specified maximum allowable difference in the creep strain increment which was set to 0.1 percent.

The tensile and internal pressurization (burst) tests were simulated in the finite element modeling software. For the tensile test simulations, a constant displacement rate was applied to the end cap as shown in Figure 26. The nodal displacements of pipe surface that was in contact with

the end cap were coupled with the reference point of the end cap to model the contact properties between the clamped pipe and the end cap. Symmetry boundary conditions in the z-direction were applied to the other end of the pipe. To simulate the tensile test experiments, reported in table 3, several analyses were conducted using different displacement rates and different temperatures ($20°C, 42°C, 60°C,$ and $80°C$). Since only half of the pipe was modeled, the corresponding displacement rates were half of the one applied during the experiments to ensure that the pipe experiences the same level of strain rate for both cases.

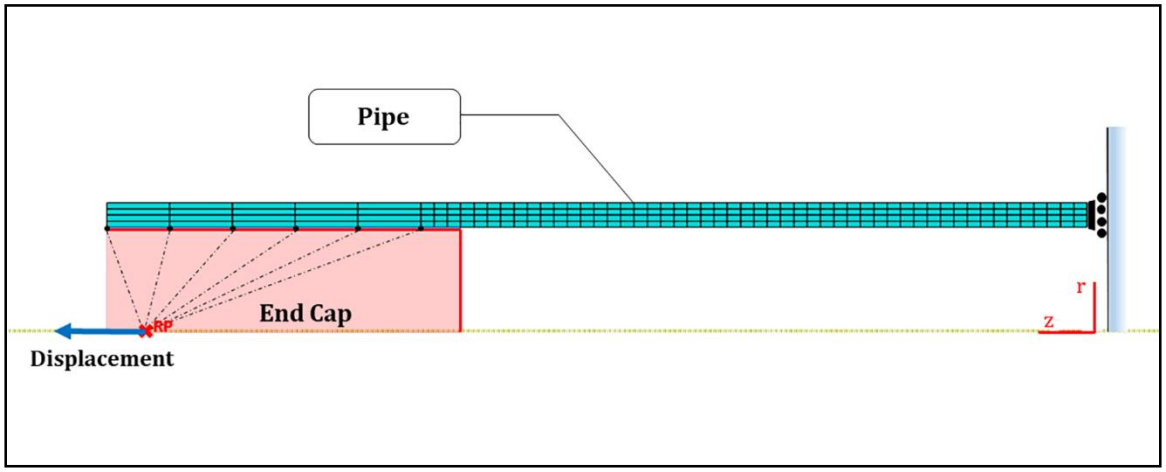

Figure 26: Modeled pipe during the tensile tests.

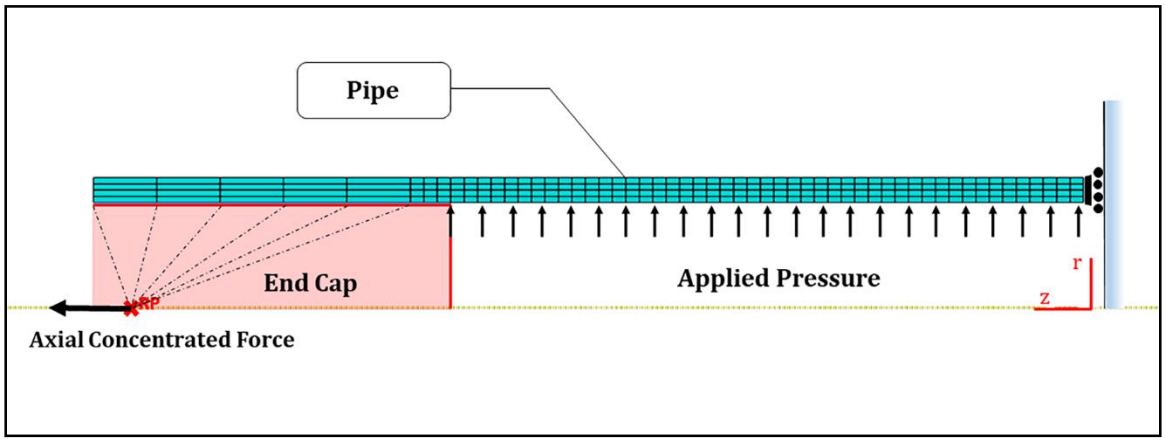

Figure 27: Modeled pipe with corresponding loading and boundary conditions under internal pressurization (burst) tests.

The internal pressurization (burst) tests were simulated using different levels of internal pressures. The pressure was applied on the inside surface of the pipe in the form of a normal surface

load. Also, an extra concentrated axial force was applied to the end cap. The force represents the axial load caused by internal pressure. Figure 27 shows the modeled pipe and applied load during internal pressurization (burst) tests. To evaluate the long-term hydrostatic strength curves, several simulations conducted using different pressures and temperatures. To investigate the effect of variation in the working temperature, an internal pressurization (burst) test was simulated where a constant pressure, 2.275 MPa (330 psi), with a daily fluctuating temperature was applied on the pipe. The average temperature was set to $25°C$ $(298\,K)$ with $\pm 5\,K$ daily variation. The simulation was conducted in Abaqus CAE software by using the user creep subroutine file.

3.5. Results and Discussion

To study the effect of variation in elastic properties on the long-term performance of the pipes, two sets of simulations were performed using the viscoplastic model and elastic properties. The only difference between these two sets of simulations was the magnitude of elastic modulus which was set to the minimum and maximum value observed during the room temperature tensile tests, 400 and 600 MPa. The simulations were conducted under different internal pressure levels and at 23℃. The model predictions are shown in Figure 28. Based on the results, the predictions where the elastic modulus of 400 MPa was used, result in a shorter lifetime comparing to those where the elastic modulus of 600 MPa was used. However, the differences between the two prediction lines were neglectable, especially for the lower stress levels. Thus, it appears that rate-dependent stiffness variations of the HDPE do not play a significant role in the long-term performance of the pipes, and simply a constant elastic modulus can be utilized. The values for the elastic modulus used at each temperature are given in Table 2.

The numerical model was used to estimate the tensile tests results under different strain rates and temperatures based on Table 3. The stress-strain results of the numerical simulation are presented in Figure 29 where numerical estimations (shown with solid lines) are compared with the experimental data (shown with dashed lines). As the results show, the numerical model can estimate the magnitude of yield stresses with good accuracy; however, the estimated yielding appeared at a lower strain compared to the experimental data. The model is less accurate for the highest temperature investigated (80℃), a result which is related to the existence of a secondary yielding at large strain (~0.6) [8], a behavior which was not considered in the model. In general,

one can conclude that the presented numerical model is highly sensitive to the variations of applied strain rates and temperatures, and the predictions are in a good agreement with the experimental data.

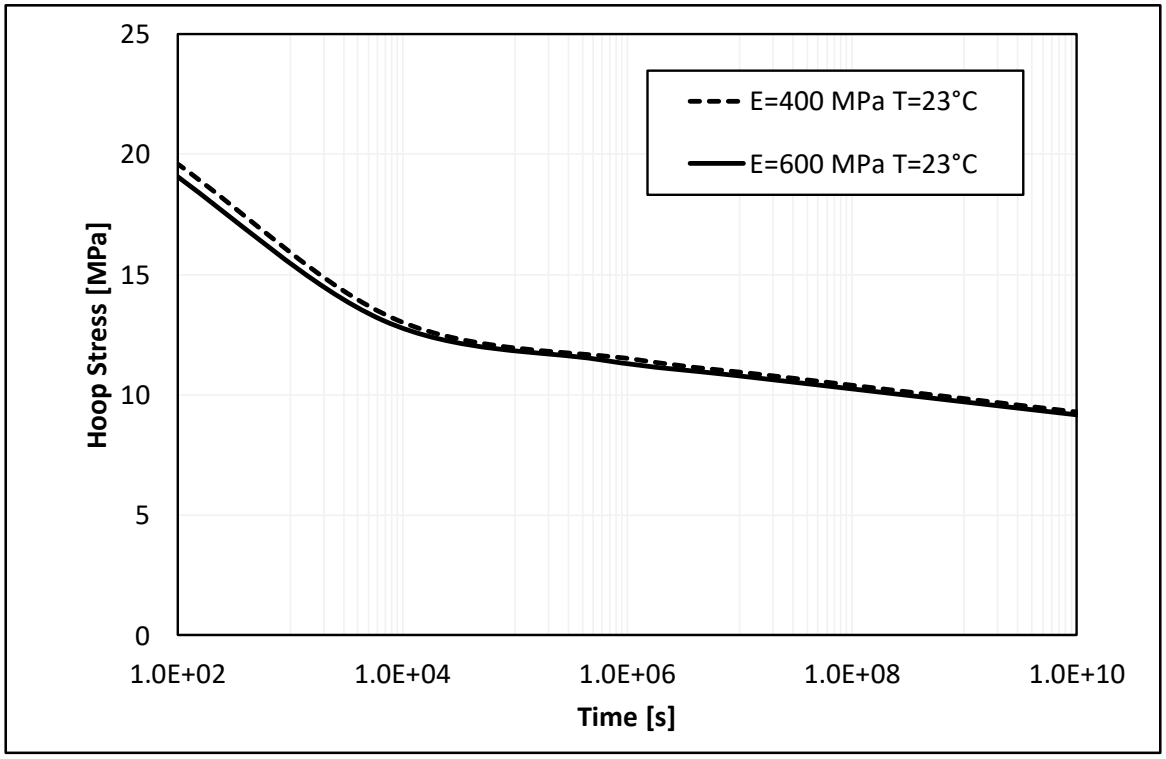

Figure 28: Effect of using different initial elastic properties on the estimated creep behavior of the material.

The numerical model, using the given parameters in Table 2, was employed to simulate the pipe burst tests at room temperature. Since the burst tests were conducted at a temperature range of 21 ± 2℃, the simulations were conducted under different internal pressures and at 19℃ and 23℃. Figure 31 shows the deformed pipe during ductile failure under the internal pressure loading. The top image was created using the numerical model and the bottom image was captured from the actual pipe during a burst test. Figure 31 indicates that the numerical simulation accurately mimics the geometry of the failed pipe during the test. The model predictions of time-to-failure are presented in figure 30 where the numerical simulation results are shown by solid lines and the experimental data are shown by the circles. Based on the observation from Figure 30, the model successfully predicts the trend of the actual time-to-failure data. However, the model is slightly conservative in predicting the failure time. Among all of the experimental data points, in 17 cases

(~53%) the failures occurred within the prediction lines and in 15 cases (~47%) the samples were failed after the predicted failure time. This discrepancy can be explained by the observation that the yielding occurs at lower strain levels in the model than in the experiments.

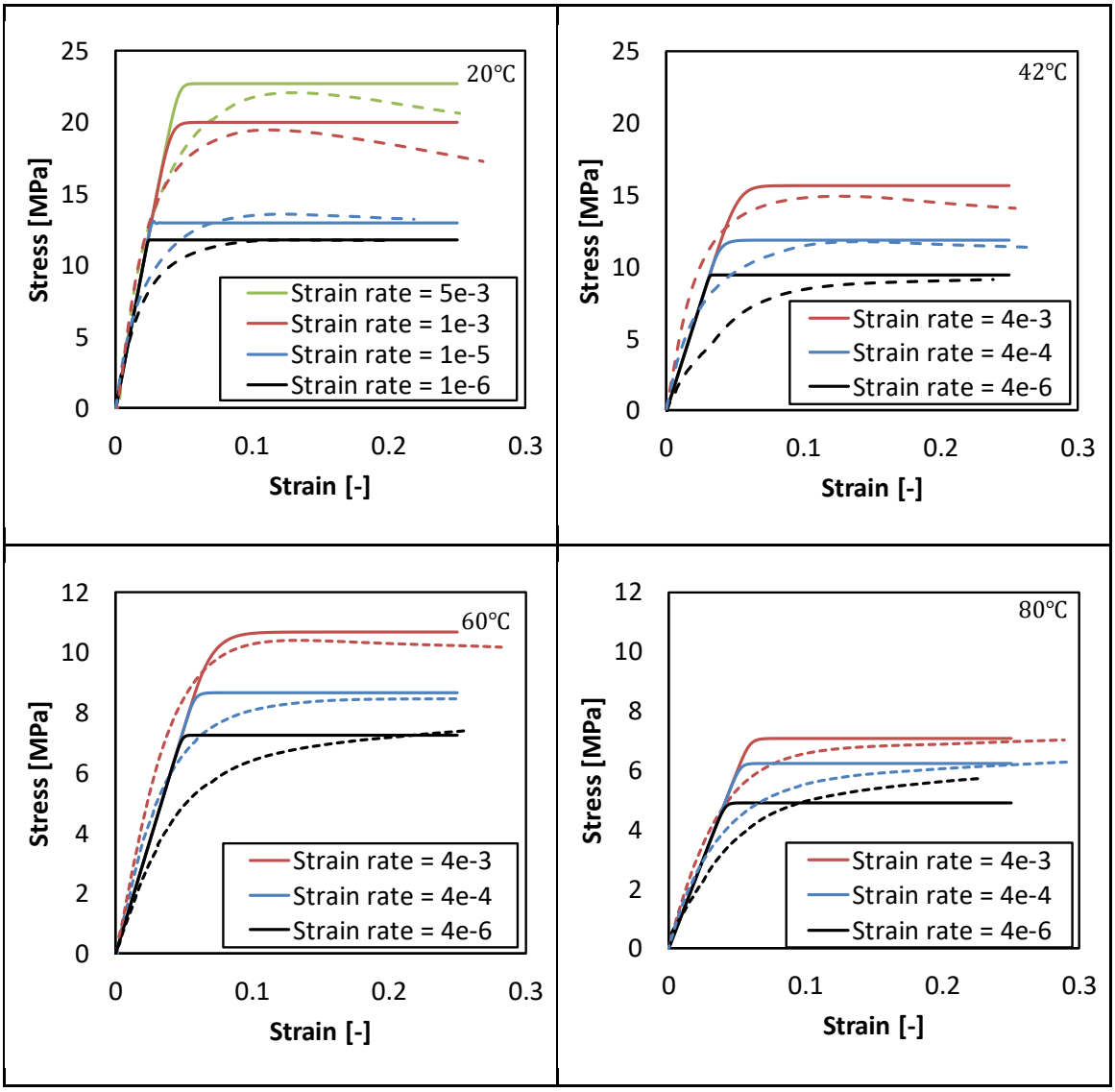

Figure 29: Numerical simulation results of uniaxial tensile tests at different temperatures and strain rates, the solid lines. The experimental measurements were shown with dashed lines.

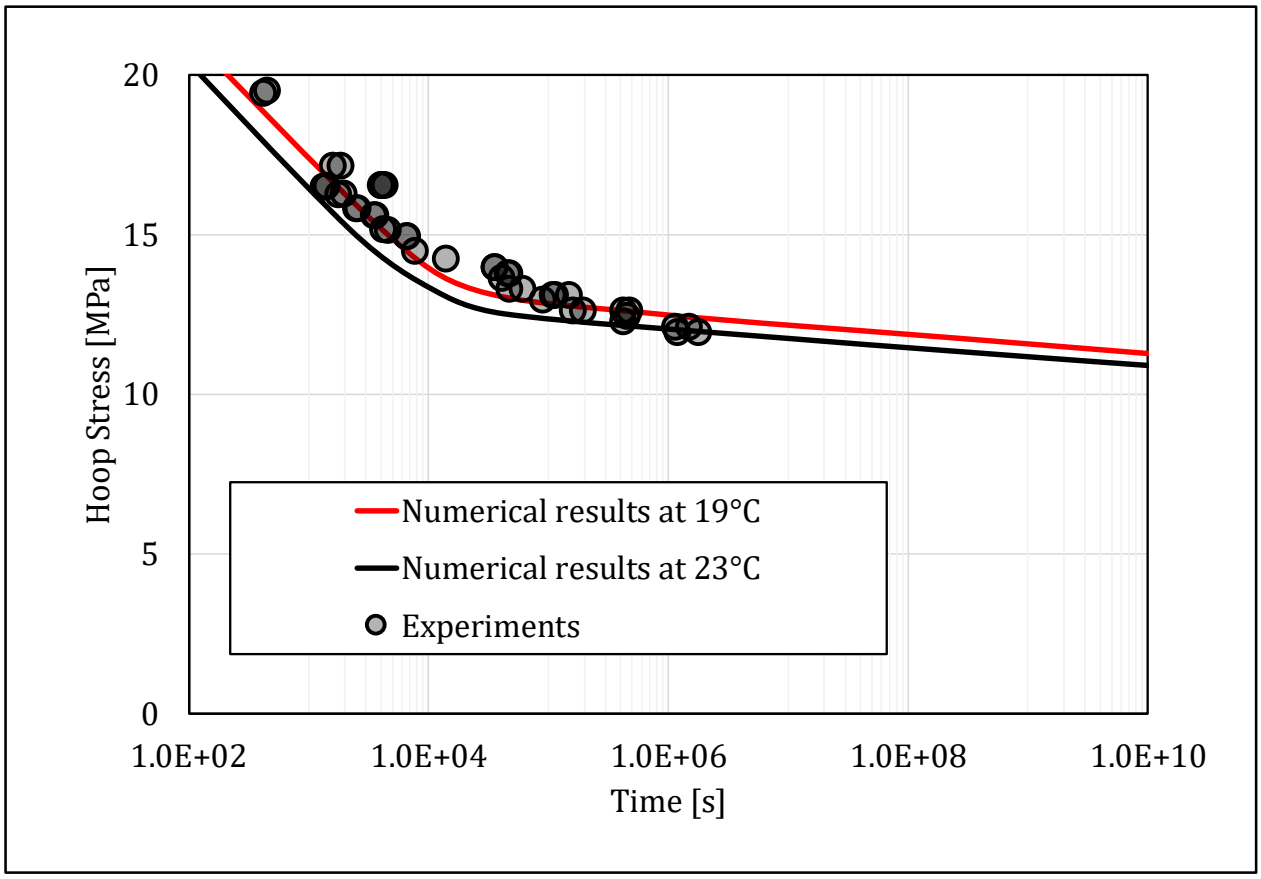

Figure 30: The numerical simulation results for the pipe ductile failure at 19°C and 23°C and the experimental observations at room temperature.

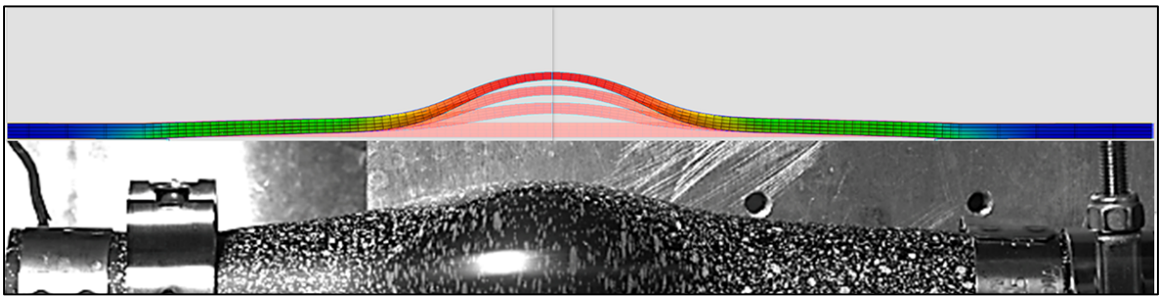

Figure 31: The deformation of the pipe during the internal pressurization (burst) test, the top image is the FE simulation of ductile pipe failure, the bottom image is a photo of the failed pipe during the test.

To study the effect of variation in the working temperature on the long-term performance of the pipe, a burst test was simulated in which a daily fluctuating temperature and a constant internal pressure were applied on the pipe. The applied pressure was set to 2.275 MPa (330 psi). Figure 32

shows the profile of applied temperature during the time (the red dashed curve). The numerical simulation was conducted using the FE model and the input loading and temperature condition. Figure 32 shows the results of the simulation where the predicted deformation is presented as a function of time. The results indicate that the material deformation was dominated by the changes in the temperature. Based on the results, an insignificant amount of deformation was observed in the pipe at the lower temperature. However, the creep deformation was accelerated by increasing the temperature. This observation can be explained based on the sensitive response of the material to the temperature. At the low temperature, 20℃, the rate of deformation is negligible with compare to the rate of deformation of the material when the temperature is only 10 degrees higher, 30℃. Thus, for a pipe working under a fluctuating temperature between T_{low} and T_{high}, the time-to-failure can be estimated as twice of the time-to-failure for the pipe under a constant T_{high} temperature.

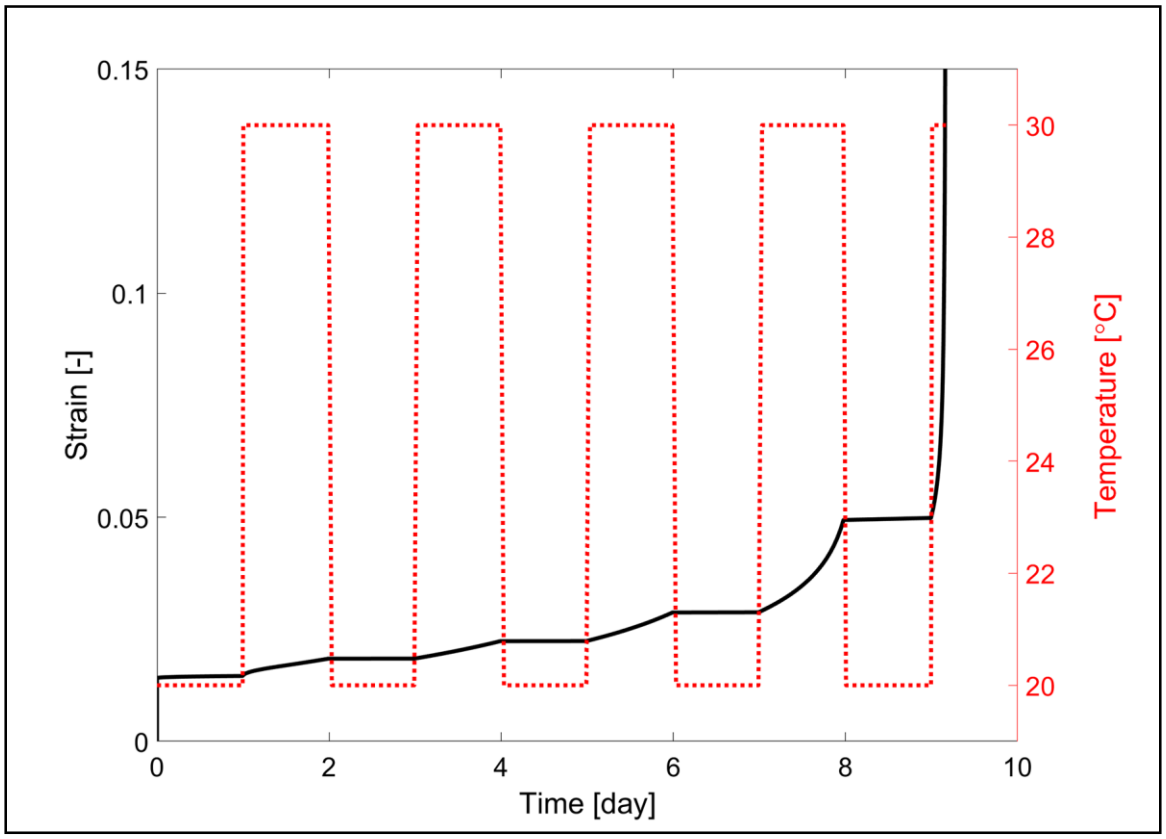

Figure 32: The daily fluctuating temperature profile and the corresponding simulated deformation of the pipe under constant internal pressure of 2.275 MPa.

3.6. Conclusions

In this chapter, the finite element method was adopted to conduct numerical modeling on the short-term and long-term behavior of the HDPE pipes. The modeling was based on the time-temperature dependent plastic model that was constructed in chapter 2. Numerical simulations were conducted using the developed Eyring plastic flow model and elastic properties of the material. The time-temperature dependent plastic response of the material was implemented into the simulation using a user-defined creep subroutine file. The subroutine was called for each integration point and at each time increment to calculate the estimated creep strain based on the state at the start of the increment. The characterization tensile tests were modeling using the presented numerical model and the numerical predictions were compared with the experimental measurements. The results revealed that the numerical model was able to estimate the magnitude of yield stresses with good accuracy, however, the estimated yielding appeared to occur at a lower strain compared to the experimental data. The model was less accurate for the highest temperature (80°C) which could be related to the existence of the secondary yielding at large strain (~0.6). The presented numerical model showed a high level of sensitivity to the variations of applied strain rates and temperatures.

The numerical model also was utilized to simulate the hydrostatic pressure (burst) tests under different internal pressure levels and at different temperatures. The long-term creep rupture predictions were evaluated using the numerical model with different values of initial elastic properties to investigate the effect of elastic properties variation on the simulations. The simulations using a higher elastic modulus resulted in an insignificant higher time-to-failure. Consequently, It was concluded that the initial viscoelastic behavior of the material did not play any significant role in the long-term performance of the pipes, and as a result, can be simplified by using the elastic properties. The numerical predictions at the room temperature ($19 - 23$ ℃) were evaluated and presented along with the experimental data. The model successfully predicted the trend of the actual time-to-failure data and the predictions were almost accurate, however, the numerical results were slightly conservative. The lower predicted value for yield strain might be the reason for observing this discrepancy.

The effect of variation in working temperature was studied as a case study. The results indicated that for a pipe working under a daily variable temperature between 20℃ and 30℃ and under constant internal pressure of 2.275 MPa (330 psi), the time-to-failure can be estimated as twice of the time-to-failure for the pipe working under the same constant internal pressure and at a constant temperature of 30℃.

Chapter 4: Residual Stress Effects on the Long-Term Performance of the Pipes

4.1. Introduction

High density polyethylene pipes are producing using the extrusion technique where hot melt of polyethylene material is pushed toward a ring-shaped die. The produced pipe is warm and soft just after it is pushed out of the die. A cold water spray is usually used to cool down the pipe. During this cooling process, cold water is sprayed on the outside of the pipe and reduces the temperature of the outside layers at a high rate while the inside of the pipe is still warm and soft. The pipe geometry may impact the cooling rate of the inside of the pipe, introducing a temperature gradient through the thickness of the pipe. This temperature gradient leads to an uneven residual hoop stress distribution across the wall thickness of the pipe. In this chapter, the distribution of residual hoop stress is evaluated for three geometrically different HDPE pipes. Then, the residual hoop stress distribution is included in the numerical simulation, introduced in the previous chapter, to study the effect of residual stress on the long-term performance of the pipes.

4.2. Profile of the Residual Hoop Stress

Residual stresses are introducing during the cooling process and are due to the uneven temperature gradient and cooling rate. Variation in cooling rate causes variation in the thermal expansion of the material across the thickness of the pipes which results in generating tensile and compression residual stresses. During the cooling process, the outside layers of the material freeze at a higher rate in comparison to the inside and middle layers. Therefore, the outside of the pipe solidifies while the inside of the pipe is still warm and soft. The fast cooling rate of the outside layers locks in the microstructural arrangement and limits the crystallization process. However, the slower cooling rate in the inside layers of the pipe allows the material to crystallize. The cold solid outside layers limit the thermal shrinkage of inside layers. Consequently, the continuity between layers causes the generation of compressive and tension residual hoop stress on the outside and inside layers of the pipe.

4.2.1. Residual Hoop Stress Evaluation Method

In this study, the ring slitting method introduced by Williams et al. [30] was adopted to evaluate the distribution of the residual hoop stress across the wall thickness of three geometrically different HDPE pipes. Figure 33 (a) shows the schematic illustration of a pipe ring cut from the pipe. The axisymmetric equilibrium equation holds for the residual stress components across the thickness of the pipe as

$$\frac{d\sigma_r}{dr} + \frac{\sigma_r - \sigma_\theta}{r} = 0 \tag{4.1}$$

where σ_r and σ_θ are the radial and the hoop residual stresses. The boundary conditions state that the radial component of the residual stress is zero on the inside and outside of the pipe, and equilibrium condition holds for the net force in the hoop direction, thus,

$$\int_{r_i}^{r_o} \sigma_\theta dr = 0 \tag{4.2}$$

where r_i and r_o are the original inside and outside radius of the pipe. Rearranging equation (4.1) and using equation (4.2), the radial component of residual stress for any radius r can be evaluated as

$$\sigma_r = \frac{1}{r}\int_{r_i}^{r} \sigma_\theta dr = -\frac{1}{r}\int_{r}^{r_o} \sigma_\theta dr \tag{4.3}$$

By removing layers of material from outside of the pipe as shown in Figure 33 (b), the radial component of residual stress on the new outside surface is reduced to zero by elastic unloading, and the residual hoop stress can be evaluated as

$$\sigma'_\theta(r) = \sigma_\theta(r) + \Delta\sigma_\theta(r) \tag{4.4}$$

where $\Delta\sigma_\theta$ is the changes in residual hoop stress and caused by elastic unloading. The changes in residual hoop stress can be expressed by Lamé solutions as

$$\Delta\sigma_\theta(r) = -\frac{1}{r_c}\int_{r_i}^{r_c} \sigma_\theta dr \times \left\{\frac{r_c^2}{r_i^2 - r_c^2}\left[1 + \frac{r_i^2}{r^2}\right]\right\} \tag{4.5}$$

where r_c is the new outside radius of the pipe after removing layers. Although the average residual hoop stress across the thickness is zero, a pure bending moment exists in the pipe which can be released by axial slitting of the pipe. This bending moment is calculated by

$$M = \int_{r_i}^{r_c} \sigma'_\theta(r) r dr \tag{4.6}$$

By substituting Equation (4.5) into (4.4) and then into Equation (4.6), we obtain

$$M = \int_{r_i}^{r_c} \sigma_\theta(r) r dr - \frac{r_c}{2}\left(1 + \frac{2\ln\left(\frac{r_c}{r_i}\right)}{\left(\frac{r_c}{r_i}\right)^2 - 1}\right)\int_{r_i}^{r_c} \sigma_\theta(r) dr \tag{4.7}$$

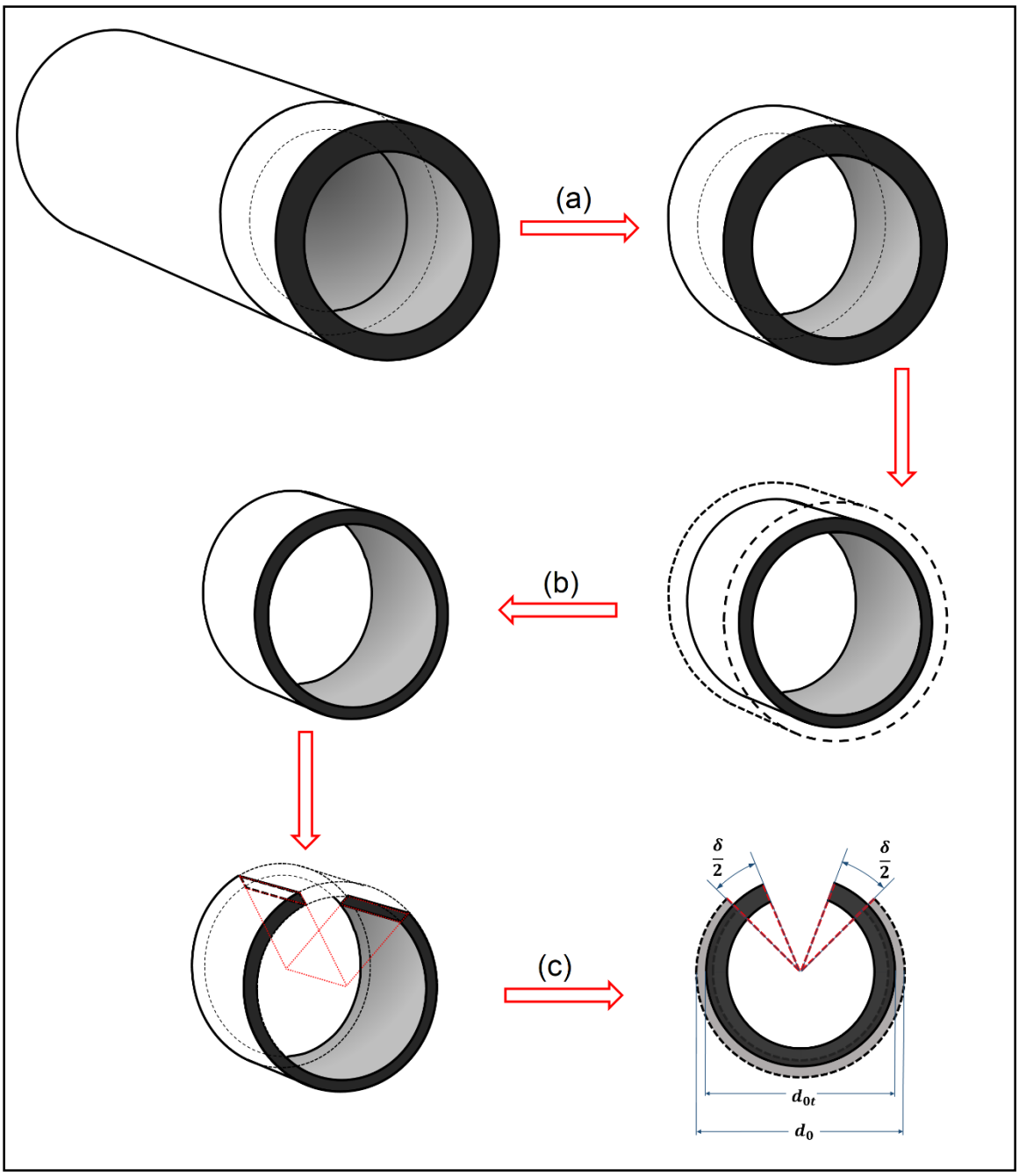

Figure 33: Schematic illustration of the sample preparation for the residual stress analysis. (a) A ring was cut from the pipe, (b) Material was bored out from the outside of the pipe, (c) The sample was axially cut and the bending moments were released.

However, slitting the pipe and reducing the bending moment to zero causes displacement, δ, as shown in Figure 33 (c), which can be related to the bending moment by

$$\delta = \frac{8\pi M}{E r_i}\Gamma \tag{4.8}$$

where E is the elastic modulus of the material and Γ is determined by;

$$\Gamma = \left\{\left(\frac{r_c}{r_i}\right) + 1\right\} \Big/ \left\{\left(\left(\frac{r_c}{r_i}\right)^2 - 1\right) - \frac{\left(\frac{r_c}{r_i}\right)^2 \left(ln\left(\frac{r_c}{r_i}\right)^2\right)^2}{\left(\frac{r_c}{r_i}\right)^2 - 1}\right\} \tag{4.9}$$

For thin walled pipes, by substituting equation (4.8) into (4.7) and differentiating twice, the residual hoop stress can be written in terms of radial deformation function as

$$\sigma_\theta(r) = \frac{E}{12\pi r_o^2}\left(4t\delta + t^2\frac{d\delta}{dr} + 2\int \delta\, dr\right) + \sigma_0 \tag{4.10}$$

where t is the remaining thickness, and σ_0 is a constant which is evaluated by using the condition of balance of hoop stress though the thickness of the pipe, as

$$\int_0^{r_o - r_i} \sigma_\theta dr = 0. \tag{4.11}$$

4.2.2. Residual Hoop Stress Measurement

The residual stress measurements were conducted on three geometrically different HDPE pipes, standard dimension ratio of 9, 11 and 13 with a nominal outside diameter of 33 mm. The pipes were made from the same resin and under the same processing conditions; however, different pipe thickness may have introduced different residual hoop stresses. The hypothesis is that pipes with a thicker wall will have a lower average cooling rate during the cooling process which causes a higher level of crystallinity and higher magnitude of residual hoop stress across the wall.

Seven rings with a length of 6 mm were cut from each pipe. Then different amounts of material were carefully removed from the outside of the rings using a lathe. Water cooling was employed to prevent the specimen from overheating during this machining process. Table 4 summarizes the dimensions of each pipe specimens. In the next step, the specimens were slit axially. Since the

material tends to close (positive δ), small pieces were cut out to allow the material deform without any restriction (see Figure 33 (c)). Figure 34 shows the seven specimens cut and slit for the SDR 9 HDPE pipe. Although the same length of the material was cut off from each specimen during axial slitting, different amounts of displacement, δ, were observed, as it is noticeable in figure 34. The first specimen with original wall thickness closed significantly (positive δ) while the last specimen with the lowest wall thickness slightly opened (negative δ). In addition, significant variation in the magnitude of measured displacements were observed over the time after the axial slitting of the rings. The displacement, δ, was determined as;

$$\delta = \pi(d_o - d_{ot}) \tag{4.12}$$

where, d_o and d_{ot} are outside diameter of the specimens before and after axial slitting (see figure 33 (c)). Table 5 presents the measured displacements over the time for all specimens. The specimens' displacements were measured for 10 weeks (1680 hours) and, as is shown in Figure 35, no further significant changes were observed after 4 weeks (672 hours).

Figure 34: Prepared specimens for residual hoop stress measurements (the SDR 9 HDPE pipe).

Table 4: Dimensions of cut rings after machining from the outer diameter. D_0 and H are the original outside diameter and wall thickness, and d_0 and h are the specimen's outside diameter and wall thickness after machining. (All dimensions are in millimeters.)

I	SDR9 $D_o = 33.28$ $H = 4.01$		SDR11 $D_o = 33.31$ $H = 3.30$		SDR13 $D_o = 33.31$ $H = 2.89$	
	d_o	h	d_o	h	d_o	h
1	33.28	4.01	33.31	3.30	33.31	2.89
2	32.40	3.56	32.53	2.91	32.82	2.65
3	31.38	3.05	31.82	2.56	32.13	2.30
4	30.31	2.52	31.03	2.16	31.55	2.01
5	29.31	2.02	30.29	1.79	30.78	1.63
6	28.23	1.48	29.50	1.40	30.00	1.24
7	27.09	0.91	28.60	0.95	29.09	0.78

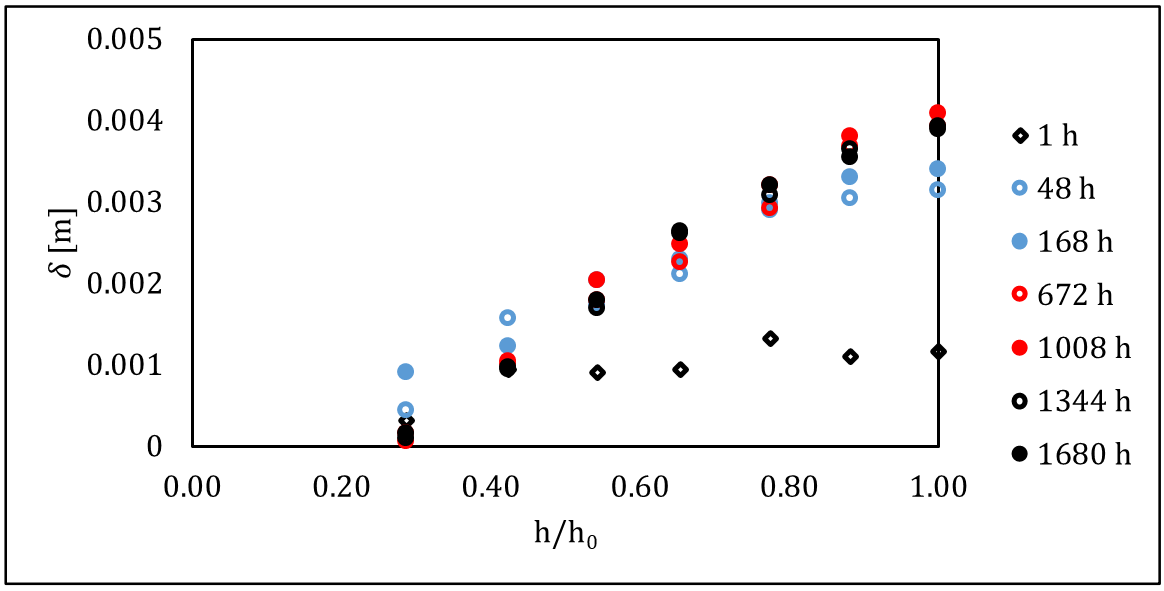

Figure 35: Measured displacements over time for specimens from the SDR 11 HDPE pipe. The horizontal axis denotes the normalized distance of the machined surface from the inner surface of the pipe.

Table 5: Measured displacements, δ, in millimeters as a function of time after axial slitting

	Elapsed time after axial slitting (h)						
	1	48	168	672	1008	1344	1680
SDR9-1	1.288	2.922	3.079	3.236	3.644	3.519	3.613
SDR9-2	1.571	3.173	3.330	3.487	3.550	3.707	3.707
SDR9-3	0.974	2.168	2.231	2.293	2.419	2.419	2.545
SDR9-4	0.660	1.477	1.634	1.791	1.602	1.728	1.885
SDR9-5	0.408	0.974	1.068	1.225	1.319	1.288	1.131
SDR9-6	0.377	0.220	0.314	0.031	0.251	0.283	0.346
SDR9-7	0.094	-0.157	-0.503	-1.257	-0.628	-0.471	-0.565
SDR11-1	1.162	3.142	3.393	3.927	4.084	3.896	3.927
SDR11-2	1.100	3.047	3.299	3.676	3.801	3.644	3.550
SDR11-3	1.319	2.890	2.985	2.922	3.204	3.079	3.204
SDR11-4	0.942	2.105	2.293	2.262	2.482	2.639	2.608
SDR11-5	0.911	2.042	1.728	1.791	2.042	1.696	1.791
SDR11-6	0.942	1.571	1.225	1.037	1.005	0.942	0.974
SDR11-7	0.314	0.440	0.911	0.157	0.063	0.094	0.157
SDR13-1	1.445	3.299	3.896	4.43	4.367	4.524	4.618
SDR13-2	1.602	3.707	3.99	4.147	4.744	4.587	4.461
SDR13-3	0.942	2.89	2.985	3.236	3.487	3.393	3.424
SDR13-4	0.942	2.608	2.639	3.047	3.204	3.11	3.267
SDR13-5	1.225	2.765	2.796	2.89	2.513	2.765	2.922
SDR13-6	0.377	2.262	1.257	1.948	1.477	1.571	1.791
SDR13-7	0.408	1.665	0.251	-0.157	-0.377	-0.314	-0.314

To evaluate the residual hoop stress using equation (4.10), the function of displacement was needed to be determined. A quadratic equation

$$\delta = b_0 + b_1\left(\frac{h}{h_0}\right) + b_2\left(\frac{h}{h_0}\right)^2 \tag{4.13}$$

was fit to the measured displacements shown in Figure 35, where b_0, b_1 and b_2 are the fitting constants. By substituting the displacement function, Equation (4.13), into Equation (4.10), the residual hoop stress can be evaluated as

$$\sigma_\theta(r) = \frac{E h_0}{12\pi r_\delta^2}\left(6b_0\left(\frac{h}{h_0}\right) + 6b_1\left(\frac{h}{h_0}\right)^2 + \frac{20}{3}b_2\left(\frac{h}{h_0}\right)^3\right) + \sigma_0 \tag{4.14}$$

Then using the equilibrium condition, equation (4.11), σ_0 can be expressed

$$\sigma_0 = -3b_0 - 2b_1 - \frac{5}{3}b_2 \tag{4.15}$$

The evaluated values of the unknown constants are shown in Table 6 which correspond to the displacements of the three pipes after 4 weeks. Using Equation (4.14), the residual hoop stress curves were constructed and shown in Figure 36. The results show that the residual hoop stress is positive (tension) in the inner layers while it is negative (compression) in the outer layers. The magnitude of these tension and compression residual stresses is higher for SDR 9 pipes than it is for SDR 11 and SDR 13 pipes. This observation can be related to the difference in temperature gradients that the pipes experienced during the cooling process. Pipes with a thicker wall experience higher gradients of temperature on average. The results also indicate that residual stresses in the SDR 11 and SDR 13 pipes were nearly identical.

Table 6: Evaluated fitting constants of Equation (4.13) for different pipes geometries.

	b_0	b_1	b_2
SDR 9	-0.0022	0.0076	-0.0015
SDR 11	-0.0025	0.0099	-0.0035
SDR 13	-0.0036	0.0148	-0.0067

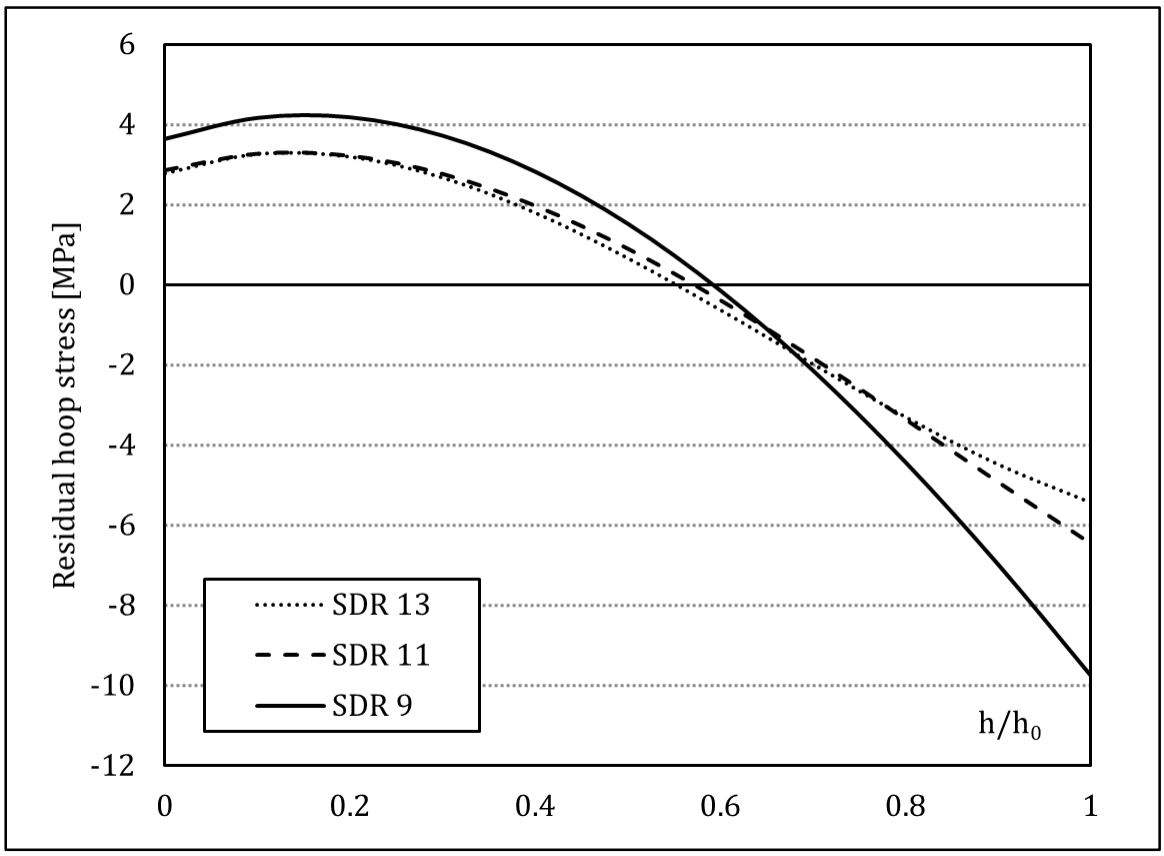

Figure 36: Residual hoop stress distribution across the wall thickness of the three pipes.

4.3. Residual Hoop Stress and Long-Term Performance

In this section, the numerical model presented in Chapter 3 and the residual hoop stresses measured in the previous section were utilized to study the effect of residual hoop stress on the long-term performance of HDPE pipes. In this regard, several numerical simulations were conducted on two SDR11 pipe models at different temperatures and under different levels of internal pressures. In the first pipe model, the profile of residual hoop stress across the wall thickness was set to zero, while in the second pipe model, measured residual hoop stress profile was applied directly on the pipe wall. The pipes modeled as a deformable axisymmetric shell with the same dimensions as the pipe segments used in the internal pressurization tests. Because of the symmetry in the axial direction of the pipe, only half of the pipe is needed to be modeled and appropriate constraints are applied. The developed user subroutine (Appendix A) was used to describe the plastic deformation of the material during the hydrostatic pressure simulations.

For the second pipe model, 10 uniform portions were created through the wall thickness of the pipe. The measured residual hoop stresses in the SDR11 pipe were applied directly to each of these portions as a pre-defined state of stress in the hoop direction. Figure 37 shows the contours of applied residual hoop stress.

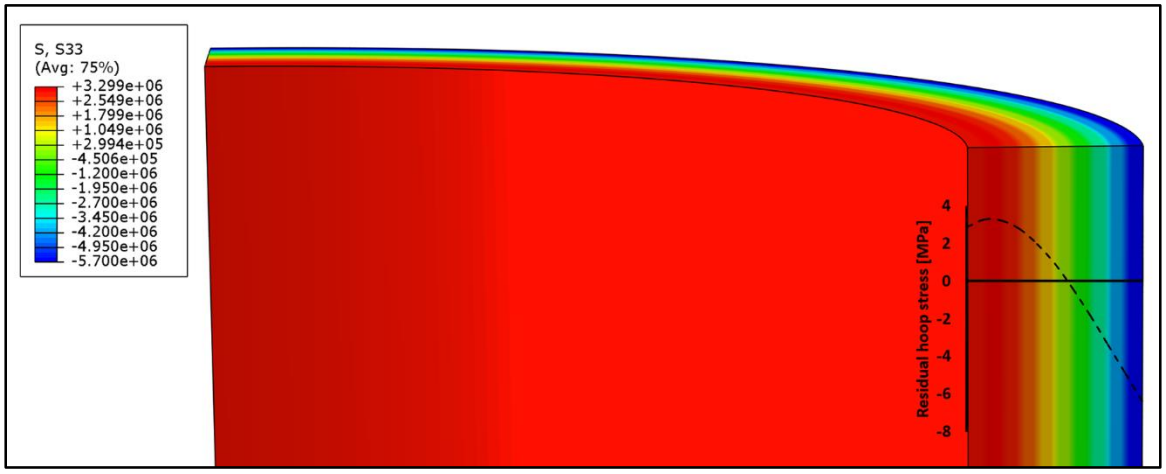

Figure 37: Contours of applied residual hoop stress.

The hydrostatic pressure tests were conducted at three temperatures (20°C, 60°C and 80°C) and under different internal pressures for both pipe models. The results of the simulations and experimental data are presented in Figure 38. The estimated time-to-failure in each test configurations and for both pipe models are reported in Table 7. As the results show, for all testing configurations the residual hoop stress accelerated the creep rupture failure. Up to 6.6 times faster failure was observed at room temperature. However, the amount of acceleration decreases with increasing temperature. The results in Figure 38 indicate that a slightly better prediction can be achieved by considering the residual hoop stress into the modeling. The differences between the predictions, however, are negligible compared to the variation in experimental data. Therefore, although taking account the residual hoop stress into the simulations increases the accuracy of predicted time-to-failure, the modification does not practically change the prediction. On the other hand, the residual stress evaluation requires almost one month to be complete which is three times more than the mechanical characterization tests. Thus, one can conclude that the long-term performance of the pipes made from this HDPE can be evaluated without considering the residual stresses.

Table 7: Results of numerical simulations

Temperature (°C)	Pressure (MPa)	Hoop Stress (MPa)	Predicted time-to-failure		
			Pipe model I*	Pipe model II**	Rate of failure acceleration***
20	4.137	22.753	3.00E+01	2.70E+01	1.111
	2.758	15.168	3.55E+03	3.25E+03	1.091
	2.413	13.272	2.21E+04	1.59E+04	1.392
	2.275	12.514	8.09E+05	1.49E+05	5.432
	2.137	11.756	2.60E+08	3.93E+07	6.611
	1.999	10.997	8.49E+10	1.44E+10	5.911
	1.931	10.618	1.57E+12	2.73E+11	5.740
60	1.655	9.101	9.18E+02	4.86E+02	1.889
	1.379	7.584	1.36E+07	4.54E+06	2.985
	1.241	6.826	2.15E+09	7.95E+08	2.709
	1.103	6.067	3.36E+11	1.38E+11	2.428
80	1.241	6.826	3.19E+02	1.65E+02	1.933
	1.103	6.067	3.05E+04	1.36E+04	2.243
	0.827	4.551	4.09E+08	2.23E+08	1.832
	0.689	3.792	4.78E+10	2.93E+10	1.628

* Without considering the residual hoop stress.

** With considering the residual hoop stress.

*** The ratio of predicted time-to-failure using pipe model I and II.

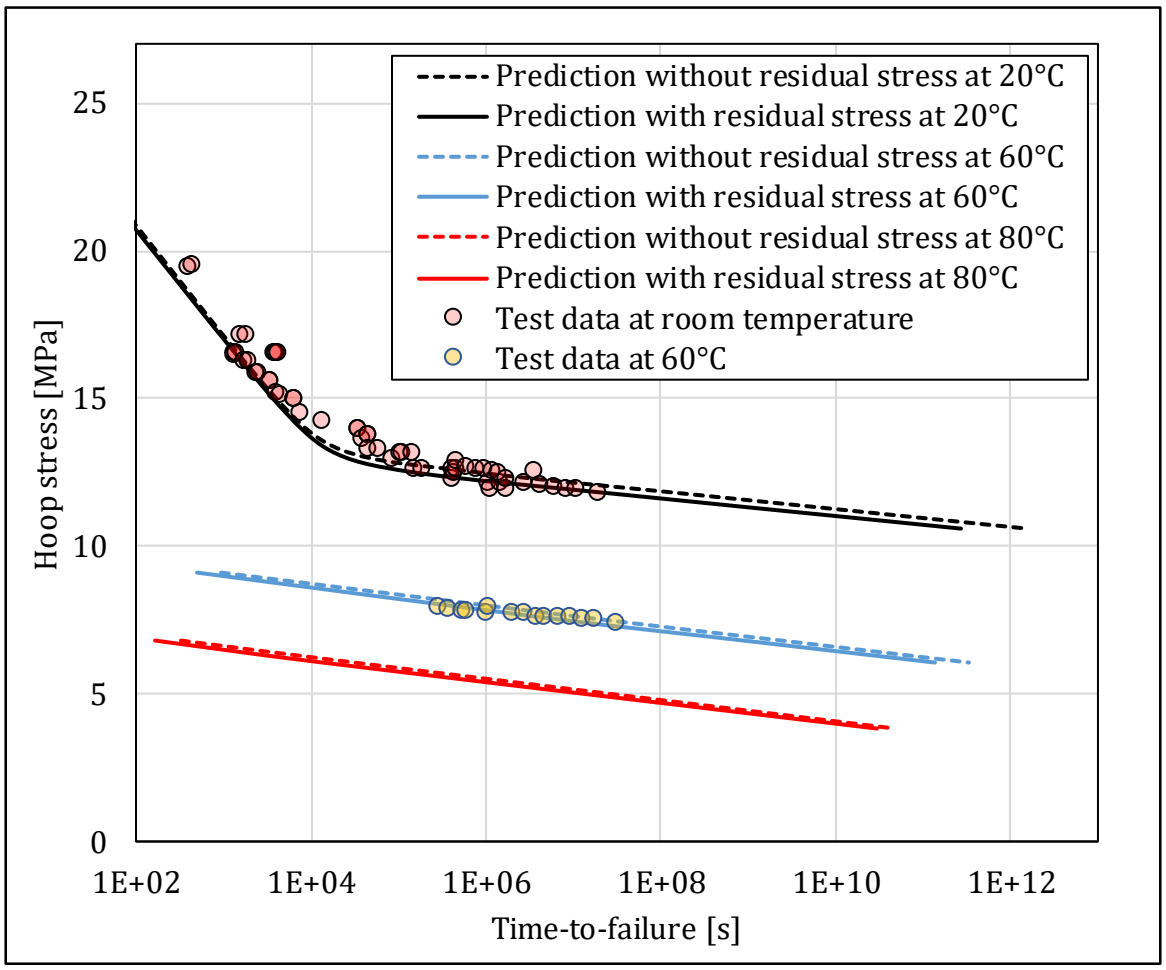

Figure 38: Failure predictions with and without considering the residual hoop stress, the solid and dashed lines, respectively. The circles are the experimental data from hydrostatic pressure (burst) tests.

4.4. Conclusions

In this chapter, the ring sliting method was adopted to evaluate the residual hoop stress profile for three geometrically different HDPE pipes. Several small rings were cut from each pipe and the material was carefully bored out from the outside of the ring by the machining technique. Consequently, the samples were slit axially and allowed to freely deform and release the bending moments which were the results of non-uniform residual hoop stresses. The deformations of the samples were measured over time and then the profile of residual hoop stress was evaluated by relating the released bending moment and the measured sample deformations.

Based on the results of evaluated residual hoop stress, the magnitude of residual stresses was found to be higher for the pipe with a thicker wall (SDR 9 pipe). The explanation for this observation is the difference in temperature gradients that the pipes experienced during the cooling process: pipes with a thicker wall were experienced a higher temperature gradient. A higher gradient of temperature yields to a higher magnitude in the tension and compression residual stresses. The same magnitudes of residual stresses were observed for the SDR 11 and SDR 13 pipes, indicating that the magnitude of residual stress is less sensitive to the variation of wall thickness for thinner pipes. However, as the wall thickness increases, the magnitude of residual stresses become more sensitive to the pipe geometry.

Numerical simulations were conducted to study the effect of residual hoop stress on the long-term performance of the pipes. Hydrostatic pressure (burst) tests were simulated with and without the residual stresses at different temperatures and under different internal pressures. The numerical predictions suggested that the residual hoop stress accelerated the creep rupture failure up to 660% at the room temperature. The amounts of acceleration, however, were lower for higher temperatures. Although a slightly better prediction was achieved by considering the residual hoop stress into the modeling, the alteration was negligible in comparison to the variation in experimental data. Therefore, although including the residual hoop stress into the simulations altered the predicted time-to-failure, the model modification does not significantly change the prediction for this HDPE pipe. Thus, due to the significant time cost of the residual stress evaluation, it was concluded that the long-term performance of the pipes can be evaluated without considering the residual stresses.

Chapter 5: Summary, Conclusions and Future Work

5.1. Summary and Conclusions

This study focuses on the long-term performance of HDPE pipes. An accelerated testing method was presented in Chapter 2 where mechanical characterization tests were conducted on as-manufactured pipe segments. Several tensile and compression tests were conducted at different rates of deformation and temperatures on the pipe segments. Using as-manufactured pipe segments eliminates any additional needs for adjusting the material state and enhances the ability to study the effect of different processing conditions on material behavior. The yield kinetics were described using two pressure-modified Eyring processes working in parallel. Hydrostatic pressure effect on the plastic flow behavior of the material was evaluated separately for each of the Eyring processes. Based on the evaluated values for the pressure modification factors, the hydrostatic pressure did not uniformly affect the plastic flow behavior of the material, and thus, independent pressure modification factors were required to characterize the effect of hydrostatic pressure on each Eyring process.

The constructed Eyring model was utilized to predict the long-term performance of the pipes. During evaluating the predictions, several critical strain values were adopted to investigate the sensitivity of the model to the magnitude of the critical strain. The results showed that the magnitude of critical strain did not play a significant role in the long-term predictions, which means

the predictions were mainly dominated by the estimated value for the plastic rate of deformation. Thus, the yield strain measured during the tensile tests was used instead of critical strain. This important observation yielded to eliminate the need for conducting characterization creep tests. Consequently, the new experimental protocol significantly reduced the required testing time to 10 days using the experimental data from only tensile and compression tests conducted using a single load frame.

To validate the model predictions internal pressurization (burst) tests were conducted. A custom-designed test setting was designed and assembled using a data acquisition system, pressure transducers, and actuators. The experimental setting was used to conduct the validation tests on the SDR 11 pipe segments under several carefully controlled constant pressures and at the room temperature. During each test, the field of deformation of each sample was measured using a high-resolution digital image correlation (DIC) system. Based on the results, the developed model was able to provide an accurate lifetime prediction, as demonstrated with the comparison of the results of experimental measurements.

Finite element method was adopted to conduct numerical modeling based on the constructed constitutive model. Numerical simulations were conducted using the developed Eyring plastic flow model and elastic properties of the material. The time-temperature dependent plastic response of the material was implemented into the simulation using a user-defined creep subroutine file. The subroutine was called for each integration point at each time increment to calculate the estimated creep strain based on the state at the start of the increment. The characterization tensile tests were modeling using the presented numerical model and the numerical predictions were compared with the experimental measurements. The results revealed that the numerical model was able to estimate the magnitude of yield stresses with good accuracy, however, the estimated yielding appeared to occur at a lower strain compared to the experimental data. The model was less accurate for the highest temperature (80°C) which could be related to the existence of the secondary yielding at large strain (~0.6). The presented numerical model showed a high level of sensitivity to the variations of applied strain rates and temperatures.

The numerical model also was utilized to simulate the hydrostatic pressure (burst) tests under different internal pressure levels and at different temperatures. The long-term creep rupture predictions were evaluated using the numerical model with different values of initial elastic properties to investigate the effect of elastic properties variation on the simulations. The

simulations using a higher elastic modulus resulted in an insignificant higher time-to-failure. Consequently, It was concluded that the initial viscoelastic behavior of the material did not play any significant role in the long-term performance of the pipes, and as a result, can be simplified by using the elastic properties. The numerical predictions at the room temperature ($19 - 23$ ℃) were evaluated and presented along with the experimental data. The model successfully predicted the trend of the actual time-to-failure data and the predictions were almost accurate, however, the numerical results were slightly conservative. The lower predicted value for yield strain might be the reason for observing this discrepancy.

The effect of variation in working temperature was investigated as a case study. The results indicated that for a pipe working under a daily variable temperature between 20℃ and 30℃ and under constant internal pressure of 2.275 MPa (330 psi), the time-to-failure can be estimated as twice of the time-to-failure for the pipe working under the same constant internal pressure and at a constant temperature of 30℃.

The residual hoop stress profile was evaluated for three geometrically different HDPE pipes in Chapter 4. In this regard, the ring slitting method was utilized where several pipe segments were cut from each pipe. Then the material was bored out from the outside of the ring. Consequently, the samples were slit axially and allowed to freely deform and release the bending moments resulted from residual hoop stresses. The deformations of the samples were measured over time and then the profile of residual hoop stress was evaluated by relating the released bending moment and the measured sample deformations.

The results of evaluated residual hoop stress indicated that the magnitude of residual stresses was higher for the pipe with a thicker wall (SDR 9 pipe). The observation can be related to the difference in temperature gradients that the pipes experienced over the cooling process. Pipes with a thicker wall experience a higher temperature gradient on average. This high gradient of temperature yields to a higher magnitude in the tension and compression residual stresses. The results also showed that SDR 11 and SDR 13 possess almost the same magnitudes of residual stresses indicated that the magnitude of residual stress is less sensitive to the variation of wall thickness for thinner pipes. However, as the wall thickness increases, the magnitude of residual stresses become more sensitive to the pipe geometry.

Finally, numerical simulations were conducted to study the effect of residual hoop stress on the long-term performance of the pipes. The hydrostatic pressure (burst) tests were simulated with and

without the residual stresses at different temperatures and under different internal pressures. The numerical predictions suggested that the residual hoop stress accelerated the creep rupture failure up to 660% at the room temperature. The amounts of acceleration, however, were lower for higher temperatures. Although a slightly better prediction was achieved by considering the residual hoop stress into the modeling, the alteration was found to be negligible in comparison to the variation in experimental data. Therefore, although including the residual hoop stress into the simulations altered the predicted time-to-failure, the model modification does not significantly change the prediction. Thus, due to the relatively high time cost of the residual stress evaluation, it was concluded that the long-term performance of the pipes can be evaluated without considering the residual stresses for this HDPE pipe.

5.2. Future Work

The following ideas are the suggestions for future work which are based on the studies presented in this dissertation.

- The ductile-brittle transition of the long-term behavior of the pipes can be investigated. The presented research focused on the ductile failure of the pipes. Although the new generation of bimodal HDPE pipes showed higher crack propagation resistance, the brittle failure due to the rapid crack propagation still needs to be investigated to ensure that the new material advancements pushed the ductile-brittle transition to such a higher time scale that the brittle failure does not appear during the service lifetime of the pipes anymore.

- A comprehensive study is required to investigate the effects of crystallinity on the ductile and brittle failure of the pipes. The higher degree of crystallinity is known to increase the creep resistance of the semicrystalline polymers as well as material stiffness. However, it reduces the crack propagation resistance of the material which can result in pre-brittle failure in the semicrystalline polymer pipes. Thus, the effects of the crystallinity need to be investigated and modeled where an optimum degree of crystallinity can be evaluated.

- Numerical techniques should be used to create a comprehensive structure-to-property model based on a robust combination of the following knowledge; the mechanical characterization (presented in the current work), the effects of material crystallinity on the mechanical properties, the thermodynamics of the extrusion and cooling process, and the kinetics of crystallization process.

References

[1] U. Schulte, A Vision Becomes True-50 Years of Pipes Made From High Density Polyethylene, Proceedings of Plastics Pipes XIII2006.
[2] M.J. Kanters, K. Remerie, L.E. Govaert, A new protocol for accelerated screening of long-term plasticity-controlled failure of polyethylene pipe grades, Polymer Engineering & Science, 56 (2016) 607-724.
[3] R. Seguela, Critical review of the molecular topology of semicrystalline polymers: The origin and assessment of intercrystalline tie molecules and chain entanglements, Journal of Polymer Science Part B: Polymer Physics, 43 (2005) 1729-1748.
[4] A. Galeski, Strength and toughness of crystalline polymer systems, Progress in Polymer Science, 28 (2003) 1643-1699.
[5] E. Oleinik, S. Rudnev, O. Salamatina, Evolution in concepts concerning the mechanism of plasticity in solid polymers after the 1950s, Polymer Science Series A, 49 (2007) 1302-1327.
[6] S. Humbert, O. Lame, J. Chenal, C. Rochas, G. Vigier, New insight on initiation of cavitation in semicrystalline polymers: in-situ SAXS measurements, Macromolecules, 43 (2010) 7212-7221.
[7] F. Detrez, S. Cantournet, R. Seguela, Plasticity/damage coupling in semi-crystalline polymers prior to yielding: Micromechanisms and damage law identification, Polymer, 52 (2011) 1998-2008.
[8] R. Seguela, F. Rietsch, Molecular topology in ethylene copolymers studied by means of mechanical testing, Journal of Materials Science, 23 (1988) 415-421.
[9] L. Lin, A. Argon, Structure and plastic deformation of polyethylene, Journal of Materials Science, 29 (1994) 294-323.
[10] F. Addiego, A. Dahoun, C. G'Sell, J.M. Hiver, O. Godard, Effect of microstructure on crazing onset in polyethylene under tension, Polymer Engineering & Science, 49 (2009) 1198-1205.
[11] D. Pope, A. Keller, Deformation of oriented polyethylene, Journal of Polymer Science: Polymer Physics Edition, 13 (1975) 533-566.
[12] A. Pawlak, A. Galeski, Plastic deformation of crystalline polymers: the role of cavitation and crystal plasticity, Macromolecules, 38 (2005) 9688-9697.
[13] A. Rozanski, A. Galeski, M. Debowska, Initiation of cavitation of polypropylene during tensile drawing, Macromolecules, 44 (2010) 20-28.
[14] A. Pawlak, Cavitation during tensile deformation of high-density polyethylene, Polymer, 48 (2007) 1397-1409.
[15] A. Bellare, R. Cohen, A. Argon, Development of texture in poly (ethylene terephthalate) by plane-strain compression, Polymer, 34 (1993) 1393-1403.
[16] C. G'sell, V. Favier, J. Hiver, A. Dahoun, M. Philippe, G. Canova, Microstructure transformation and stress-strain behavior of isotactic polypropylene under large plastic deformation, Polymer Engineering & Science, 37 (1997) 1702-1711.
[17] Z. Bartczak, A. Galeski, Yield and plastic resistance of α-crystals of isotactic polypropylene, Polymer, 40 (1999) 3677-3684.
[18] R.H. Boyd, Relaxation processes in crystalline polymers: molecular interpretation—a review, Polymer, 26 (1985) 1123-1133.
[19] J.-L. Syi, M.L. Mansfield, Soliton model of the crystalline α relaxation, Polymer, 29 (1988) 987-997.

[20] R. Seguela, V. Gaucher-Miri, S. Elkoun, Plastic deformation of polyethylene and ethylene copolymers: Part I Homogeneous crystal slip and molecular mobility, Journal of materials science, 33 (1998) 1273-1279.
[21] M. Mansfield, R.H. Boyd, Molecular motions, the α relaxation, and chain transport in polyethylene crystals, Journal of Polymer Science: Polymer Physics Edition, 16 (1978) 1227-1252.
[22] R. Popli, M. Glotin, L. Mandelkern, R. Benson, Dynamic mechanical studies of α and β relaxations of polyethylenes, Journal of polymer science: polymer physics edition, 22 (1984) 407-448.
[23] T. Trankner, M. Hedenqvist, U.W. Gedde, Structure and crack growth in gas pipes of medium-density and high-density polyethylene, Polym Eng Sci, 36 (1996) 2069-2076.
[24] S. Boros, Long-Term Hydrostatic Strength and Design of Thermoplastic Piping Compounds, Journal of ASTM International, 8 (2011) 57-72.
[25] J. Moon, H. Bae, J. Song, S. Choi, Algorithmic methods of reference-line construction for estimating long-term strength of plastic pipe system, Polymer Testing, 56 (2016) 58-64.
[26] C. Popelar, V. Kenner, J. Wooster, An accelerated method for establishing the long term performance of polyethylene gas pipe materials, Polymer Engineering & Science, 31 (1991) 1693-1700.
[27] M.J. Kanters, K. Remerie, L.E. Govaert, A new protocol for accelerated screening of long-term plasticity-controlled failure of polyethylene pipe grades, Polymer Engineering & Science, (2016) 1548-2634.
[28] A. Kühl, P.A. Muñoz-Rojas, R. Barbieri, I.J. Benvenutti, A procedure for modeling the nonlinear viscoelastoplastic creep of HDPE at small strains, Polymer Engineering & Science, 57 (2017) 144-152.
[29] C. Cheng, G.O. Widera, Development of Maximum Secondary Creep Strain Method for Lifetime of HDPE Pipes, Journal of Pressure Vessel Technology, 131 (2009) 021208.
[30] J.G. Williams, J.M. Hodgkinson, A. Gray, The determination of residual stresses in plastic pipe and their role in fracture, Polymer Engineering & Science, 21 (1981) 822-828.
[31] E. Clutton, J. Williams, On the measurement of residual stress in plastic pipes, Polymer Engineering & Science, 35 (1995) 1381-1386.
[32] J. Poduška, J. Kučera, P. Hutař, M. Ševčík, J. Křivánek, J. Sadílek, L. Náhlík, Residual stress distribution in extruded polypropylene pipes, Polymer Testing, 40 (2014) 88-98.
[33] R.K. Krishnaswamy, Influence of wall thickness on the creep rupture performance of polyethylene pipe, Polymer Engineering & Science, 47 (2007) 516-521.
[34] J. Crissman, G. McKenna, Relating creep and creep rupture in PMMA using a reduced variable approach, Journal of Polymer Science Part B: Polymer Physics, 25 (1987) 1667-1677.
[35] E.J. Kramer, E.W. Hart, Theory of slow, steady state crack growth in polymer glasses, Polymer, 25 (1984) 1667-1678.
[36] H.A. Visser, T.C. Bor, M. Wolters, T.A. Engels, L.E. Govaert, Lifetime Assessment of Load-Bearing Polymer Glasses: An Analytical Framework for Ductile Failure, Macromolecular Materials and Engineering, 295 (2010) 637-651.
[37] T.B. Van Erp, C.T. Reynolds, T. Peijs, J.A. Van Dommelen, L.E. Govaert, Prediction of yield and long-term failure of oriented polypropylene: Kinetics and anisotropy, Journal of Polymer Science Part B: Polymer Physics, 47 (2009) 2026-2035.

[38] C. Bauwens-Crowet, J.-M. Ots, J.-C. Bauwens, The strain-rate and temperature dependence of yield of polycarbonate in tension, tensile creep and impact tests, Journal of Materials Science, 9 (1974) 1197-1201.
[39] H. Eyring, Viscosity, plasticity, and diffusion as examples of absolute reaction rates, The Journal of chemical physics, 4 (1936) 283-291.
[40] I.M. Ward, Review: The yield behaviour of polymers, Journal of materials Science, 6 (1971) 1397-1417.
[41] R. Truss, P. Clarke, R. Duckett, I. Ward, The dependence of yield behavior on temperature, pressure, and strain rate for linear polyethylenes of different molecular weight and morphology, Journal of Polymer Science: Polymer Physics Edition, 22 (1984) 191-209.
[42] C. Bauwens-Crowet, The compression yield behaviour of polymethyl methacrylate over a wide range of temperatures and strain-rates, Journal of Materials Science, 8 (1973) 968-979.
[43] C. Bauwens-Crowet, J.-C. Bauwens, G. Homes, The temperature dependence of yield of polycarbonate in uniaxial compression and tensile tests, Journal of Materials Science, 7 (1972) 176-183.
[44] J. Bauwens, Yield condition and propagation of Lüders' lines in tension–torsion experiments on poly (vinyl chloride), Journal of Polymer Science Part B: Polymer Physics, 8 (1970) 893-901.
[45] J. Roetling, Yield stress behaviour of polymethylmethacrylate, Polymer, 6 (1965) 311-317.
[46] J. Roetling, Yield stress behaviour of isotactic polypropylene, Polymer, 7 (1966) 303-306.
[47] J. Roetling, Yield stress behaviour of poly (ethyl methacrylate) in the glass transition region, Polymer, 6 (1965) 615-619.
[48] R. Truss, R. Duckett, I. Ward, Effect of hydrostatic pressure on the yield and fracture of polyethylene in torsion, Journal of Materials Science, 16 (1981) 1689-1699.
[49] C. Bauwens-Crowet, J.-C. Bauwens, G. Homès, The temperature dependence of yield of polycarbonate in uniaxial compression and tensile tests, Journal of Materials Science, 7 (1972) 176-183.
[50] B. Aidi, S.W. Case, Experimental and Numerical Analysis of Notched Composites Under Tension Loading, Applied Composite Materials, 22 (2015) 837-855.
[51] ASTM D638-14 Standard Test Method for Tensile Properties of Plastics, 2014.
[52] R. Seguela, S. Elkoun, V. Gaucher-Miri, Plastic deformation of polyethylene and ethylene copolymers: Part II Heterogeneous crystal slip and strain-induced phase change, Journal of materials science, 33 (1998) 1801-1807.
[53] D. Rees, Basic engineering plasticity, School of Eng. and Design Brunel Univ., UK, (2006) 290-292.
[54] G.F. Modlen, Engineering Plasticity. By W. Johnson and P. B. Mellor. (Ellis Horwood Limited, Van Nostrand Reinhold (UK) Ltd, 1983. First published 1973.) [Pp. 646.] International Journal of Production Research, 22 (1984) 723-723.
[55] R.M. Caddell, R.S. Raghava, A.G. Atkins, A yield criterion for anisotropic and pressure dependent solids such as oriented polymers, Journal of Materials Science, 8 (1973) 1641-1646.
[56] M. Abramowitz, I.A. Stegun, R.H. Romer, Handbook of mathematical functions with formulas, graphs, and mathematical tables, AAPT, 1988.
[57] R.M. Guedes, A viscoelastic model for a biomedical ultra-high molecular weight polyethylene using the time-temperature superposition principle, Polymer Testing, 30 (2011) 294-302.

[58] O.U. Colak, N. Dusunceli, Modeling viscoelastic and viscoplastic behavior of high density polyethylene (HDPE), Journal of Engineering Materials and Technology, Transactions of the ASME, 128 (2006) 572-578.
[59] J.M.L. Reis, L.J. Pacheco, H.S. da Costa Mattos, Tensile behavior of post-consumer recycled high-density polyethylene at different strain rates, Polymer Testing, 32 (2013) 338-342.
[60] O. Bilgin, Modeling Viscoelastic Behavior of Polyethylene Pipe Stresses, Journal of Materials in Civil Engineering, 26 (2014) 676-683.
[61] R. Haward, G. Thackray, The use of a mathematical model to describe isothermal stress-strain curves in glassy thermoplastics, Proc. R. Soc. Lond. A, 302 (1968) 453-472.
[62] J. Richeton, S. Ahzi, L. Daridon, Y. Rémond, A formulation of the cooperative model for the yield stress of amorphous polymers for a wide range of strain rates and temperatures, Polymer, 46 (2005) 6035-6043.
[63] M. Taherzadehboroujen, R. Kalhor, G. Fahs, R. Moore, S. Case, Accelerated Testing Method to Estimate the Long-Term Hydrostatic Strength of Semi-Crystalline Plastic Pipes, Polymer Engineering & Science, 60 (2019).
[64] B. Wunderlich, M. Dole, Specific heat of synthetic high polymers. VIII. Low pressure polyethylene, Journal of Polymer Science, 24 (1957) 201-213.
[65] H. Sun, R.S. Cooke, W.D. Bates, K.J. Wynne, Supercritical CO2 processing and annealing of polytetrafluoroethylene (PTFE) and modified PTFE for enhancement of crystallinity and creep resistance, Polymer, 46 (2005) 8872-8882.
[66] N. Dusunceli, O.U. Colak, Modelling effects of degree of crystallinity on mechanical behavior of semicrystalline polymers, International Journal of Plasticity, 24 (2008) 1224-1242.
[67] M. Cakmak, Y. Wang, The effect of biaxial orientation and crystallinity on the long-term creep behavior of poly (ethylene terephthalate) films below glass transition temperature, Journal of Applied Polymer Science, 41 (1990) 1867-1890.
[68] S.J. Hocker, W.T. Kim, H.C. Schniepp, D.E. Kranbuehl, Polymer crystallinity and the ductile to brittle transition, Polymer, 158 (2018) 72-76.
[69] L. Mandelkern, F. Smith, M. Failla, M. Kennedy, A. Peacock, The brittle-ductile transition in linear polyethylene, Journal of Polymer Science Part B: Polymer Physics, 31 (1993) 491-493.
[70] R.K. Krishnaswamy, Analysis of ductile and brittle failures from creep rupture testing of high-density polyethylene (HDPE) pipes, Polymer, 46 (2005) 11664-11672.

Appendix A

```
      SUBROUTINE CREEP(DECRA,DESWA,STATEV,SERD,EC,ESW,P,QTILD,
     1 TEMP,DTEMP,PREDEF,DPRED,TIME,DTIME,CMNAME,LEXIMP,LEND,
     2 COORDS,NSTATV,NOEL,NPT,LAYER,KSPT,KSTEP,KINC)
C
      INCLUDE 'ABA_PARAM.INC'
C
      CHARACTER*80 CMNAME
C
      DIMENSION DECRA(5),DESWA(5),STATEV(*),PREDEF(*),DPRED(*),
     1 TIME(2),COORDS(*),EC(2),ESW(2)
C
C
      REAL*8    :: v1, v2, e2, e1, loge1, h1, h2, g1, g2, K, y0, KK
      REAL*8    :: s, T, p, f, ff, y, x1, x2, sinh1, sinh2, n1, n2, y1
      REAL*8    :: y2, ee1, ee2, yy1, yy2, dly

      v1 = 3.457459E-3
      loge1 = 257.311
      h1 = 14.986418E0
      g1 = 36.44028E-9
      v2 = 2.658417E-4
      e2 = 1.715934E14
      h2 = 1.7930322E0
      g2 = 0.481166E-10
      K = 1.38064852E0
      KK = 1.38064852E-4

C
      e1 =e xp(loge1)
      s = QTILD
      T = TEMP
      n1 = h1/KK/T+P*g1/KK/T
      n2 = h2/KK/T+P*g2/KK/T
      ee1 = exp(n1)
      ee2 = exp(n2)
      yy1 = ee1/(v1*1e-23)
      yy2 = ee2/(v2*1e-23)
```

```
      y1 = yy1/e1
      y2 = yy2/e2
      y0 = s/(y1+y2)
      y = y0

      DO WHILE ( dly < 4. )
        y0 = y
        x1 = EXP((h1+P*g1)/(KK*T))/e1
        x2 = EXP((h2+P*g2)/(KK*T))/e2
        sinh1 = log(y0*x1+sqrt((y0*x1)**2.+1.))
        sinh2 = log(y0*x2+sqrt((y0*x2)**2.+1.))
        f = K*T*(sinh1/v1+sinh2/v2)-s
        ff =K*T*(x1/SQRT((y0*x1)**2.+1.)/v1+x2/SQRT((y0*x2)**2.+1.)/v2)
        y = y0-f/ff
        dly = log10(y0)-log10(abs(f/ff))
      END DO
      DECRA(1) = y*DTIME
C
      RETURN
      END
```

Appendix B: Degree of Crystallinity and Long-Term Performance

Differential scanning calorimetry (DSC) tests were conducted for the three pipes to measure the crystallinity and investigate the effects of pipe geometry on the microstructure of the pipe material. As well as residual stress, the differences in pipe wall thickness can introduce different cooling rates across the wall which might influence the total crystallinity of the material. In this regard, a small sample from each pipe was cut and placed in the small aluminum pans designed for the DSC tests. The DSC tests were conducted in a TA Instrument Q2000 DSC machine using a heating rate of $10\ ℃/min$ from $10℃$ to $160℃$. Figure A.1 shows the heating flow per unit of mass consumed for each sample at different temperatures. As is shown, the peak integration, ΔH_p, for the specimens from SDR 11 and SDR 13 pipes is very close (175.5 J/g and 177.2 J/g for SDR 13 and SDR 11, respectively). However, the DSC results for the SDR 9 pipe specimen show a higher area under the peak (181.8 J/g). The integrated area under the peak was compared with the heat of fusion of complete crystalline polyethylene [64], $\Delta H_0 = 276.98$ J/g, to calculate the percentage of crystallinity for each pipe. Therefore, the crystallinities of the pipes were evaluated as;

$$\chi_c = \frac{\Delta H_p}{\Delta H_0}$$

The evaluated crystallinity for each pipe is provided in Table A.1. The DSC results indicate that for the same pipe material, the percentage of crystallinity can depend on the pipe wall thickness. Higher crystallinity is measured in the pipe with a thicker wall. The slightly different crystallinity in the pipes might be directly related to the different cooling rates that the material has experienced during the cooling process. On average, the cooling rate of the material is higher in a pipe with a thinner wall, which causes very limited crystallization time. On the other hand, for pipes with a thicker wall, the cooling rate is lower and the material has more time to crystallize. This relation between crystallization, cooling rate, and the pipe's wall thickness suggests that for the same pipe material and under the same processing conditions, the material cooling rate might be less sensitive to the variation in pipe thickness for thinner pipes which is compatible with the residual stress results observed for the three pipes.

Table A.1. Evaluated crystallinities for the pipes.

	SDR 9	SDR 11	SDR 13
χ_c	65.64 %	63.97 %	63.36 %

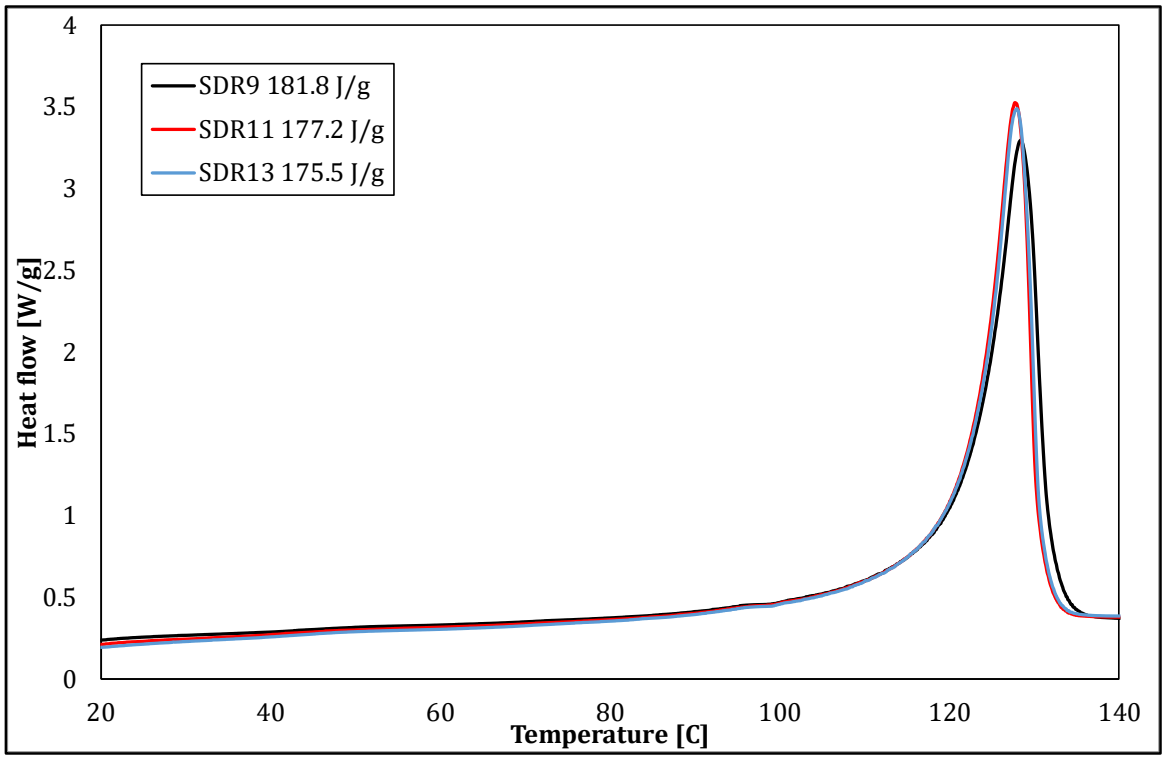

Figure A.1. DSC results for the three pipes.

High density polyethylene is a semicrystalline polymer and the degree of crystallinity of this material can be related to different parameters including the molecular architectural characteristics of the material (the molecular weight averages and distribution, the density of chain branching, and etc) and processing conditions such as the cooling rate. During the solidification of thermoplastic semicrystalline polymer, the degree of crystallinity decreases with increasing cooling rate. This behavior can be explained as follows: when the material is warm enough, around melting its point, the polymer chain molecules have high kinetic energy which enables them to deform, dislocate, twist, and move easily. As the temperature decreases, the mobility decreases, and the molecules chains want to create the most efficient microstructural pattern to minimize the potential energy. When the cooling rate is high, the temperature drops more quickly and molecule

chains have less time to arrange and stuck in an organized pattern to construct the crystals. Thus, one can conclude that a higher cooling rate results in a lower degree of crystallinity.

The effect of the degree of crystallinity on the mechanical properties of the semicrystalline polymers was investigated in different studies [65-68]. Sun et al [65] conducted a study to investigate the creep resistance improvements that can be achieved using annealing processing on polytetrafluoroethylene (PTFE). PTFE is a semicrystalline polymer with a unique combination of mechanical and electrical properties and is widely employed in different mechanical and electrical applications. Sun et al annealed PTFE samples by placing them into a pressure vessel purged by nitrogen gas and using a programmable chamber to apply different temperature during different timing scales. They were able to achieve different degrees of crystallinity, from 9 to 53%, by performing the annealing process at a verity of configurations. Then the tensile creep resistance of samples was measured and a significant improvement in the creep resistance of the materials with a higher degree of crystallinity was observed. The results indicated that by increasing the degree of crystallinity from 43.6% to 50.1% (6.5% higher), the response of the material to the room temperature creep loading was more than 5 times slower [65]. Although increasing the degree of crystallinity can significantly improve the creep resistance of the material, Cakmak et al [67] showed that increasing the degree of crystallinity also decreases the long term creep strain. In other words, increasing the degree of crystallinity transforms the material behavior from ductile to brittle. It increases the material stiffness and reduces the ductility of the material. Cakmak et al [67] designed and conducted tensile creep test on poly(ethylene terephthalate) (PET) films with different degrees of crystallinity. The results indicated that by increasing the degree of crystallinity from 23% to 30.2% the long term creep strain reduced from 0.22 to 0.12. Thus, the degree of crystallinity plays a significant role in determining the mechanical properties of the semicrystalline polymers and it introduces the ductile-brittle behavior transition into the long term response of the semicrystalline polymer pipes.

The effects of crystallinity on the ductile-brittle transition of a semicrystalline polymer were studied recently [68], where the authors conducted several tensile tests on different samples of polyamide-11 that were prepared using different conditions. Based on the observations they highlighted that the degree of crystallinity determines the transition between ductile and brittle behavior of semicrystalline polymers. Similar observations also were reported by Mandelkern et al [69] for the ductile-brittle transition of high density polyethylene. Instead of preparing and

testing samples with different degree of crystallinities, they conducted experiments to observe the transition during the course of isothermal crystallization of the material. The crystallizations were conducted in two different temperatures and for each one, the sample was initially in the primary region of crystallization and under ductile deformation. During the crystallization process, the degree of crystallinity tended to increase over time. The transition from ductile to brittle behavior was clearly observed in both temperatures only after a small change occurred in the crystallinity [69]. One of the main reasons of this observation can be addressed to an insufficient number of sequences of chain units in the amorphous phase connecting the crystallites which may lead to a limited capability of transmitting forces between the lamellae. In addition, increasing the degree of crystallinity reduces the ability to sustain large deformations in disordered connecting chain units.

Krishnaswamy [70] studied the ductile-brittle behavior transition of HDPE pipes. Different HDPE resins with a wide range of molecular architectures were used to produce the pipe samples using an extrusion process. In addition, the annealing process was employed to increase the degree of crystallinity of some samples. Based on the long term creep rupture results, a small increase (less than 2%) in the degree of crystallinity of the material increased the failure time in the ductile failure mode. The observation can be related to creep resistance improvement of the material due to increasing the degree of crystallinity, however, a more comprehensive study is required to investigate the effects of crystallinity on the ductile and brittle failure of the pipes and determine its optimum value that postpones the occurrence of the ductile-brittle transition to the higher time scales and, at the same time, achieves the highest creep resistance of the material.

Conclusion

Several DSC measurements were conducted to determine the effects of pipe geometry to the degree of crystallinity of the material. According to the results, the variation in wall thickness played a significant role in the degree of crystallinity of the material. Higher crystallinity was measured in the pipe with a thicker wall. The differences in the crystallinity of the pipe material might have a direct relationship with the different cooling rates that the material had experienced during the cooling process. The cooling rate of the material is higher in pipes with a thinner wall, which results in a limited time for the crystallization process. On the other hand, the average cooling rate for pipes with a thicker wall is lower which means that the material has more time to

crystallize. This relationship between the degree of crystallization, cooling rate, and the wall thickness of the pipes suggests that the cooling rate might be less sensitive to the pipe geometry for thinner pipes.